Mémoire d'habilitation à diriger des recherches

Inverse problems for the environment: tools, methods and applications

Maëlle Nodet

28 novembre 2013

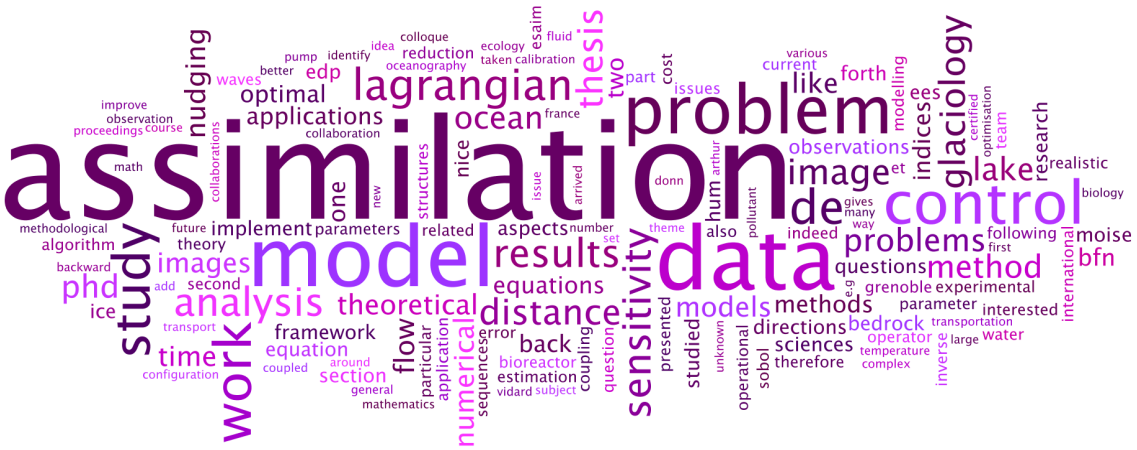

Jury :

Mark Asch (rapporteur)	Université de Picardie (Amiens)
Jacques Blum	Université de Nice Sophia Antipolis
Georges-Henri Cottet	Université Joseph Fourier et IUF (Grenoble)
Gérald Desroziers	Météo-France (Toulouse)
Bijan Mohammadi	Université de Montpellier 2
Nancy Nichols (rapporteur)	Université de Reading (Royaume-Uni)
Catherine Ritz	CNRS, LGGE (Grenoble)
Enrique Zuazua (rapporteur)	BCAM Bilbao (Espagne)

Contents

Introduction

This manuscript summarizes the work I have done since I came to Grenoble in the MOISE team (INRIA – LJK), in September 2006.

The general theme of my work is data assimilation, and more generally inverse problems and related issues (such as control and sensitivity analysis). I also attach great importance to applications, with a particularly strong taste for the environment. In fact, I think that, in the field of inverse problems, theory and applications do not make sense one without the other.

My work is therefore a constant back and forth between methodological / theoretical aspects and practical / numerical applications. I broadened my research spectrum after my thesis to both farther methods and further applications, according to Grenoble or Nice collaboration opportunities and personal research interests. One might ask why my international collaborations are underdeveloped compared to current academic standards. But we should not forget that my deepest motivation is the environment, and as such I am reluctant to travel around the world every year by plane, and I prefer collaborations that can be led by train or bicycle...

I chose to organize this manuscript into two sections: the applications on the one hand, the methodological aspects on the other. Of course there are overlaps between the two. Essentially, in the first part we start from specific problems (glaciology, oceanography, images) and classical data assimilation methods for complex models are extended, while in the second part we investigate more upstream questions, that we study on very simple models.

Each section includes a summary of the results and its own bibliography. Future directions are presented at the end of document. I give an overview of the contents of these two parts below.

Throughout the document, references numbered between brackets are my own works, gray for documents in connection with my PhD thesis, color for recent works.

Contents outlook

In the first part, I present the application aspects of my work. This section includes mostly numerical and algorithmic developments for concrete problems.

Glaciology. A few years after my arrival in Grenoble, I had the chance to meet the team of glaciologists EDGe[1] at LGGE (Laboratory of Glaciology and Geophysics of the Environment), especially Catherine Ritz, Olivier Gagliardini, Fabien Gillet-Chaulet and Gaël Durand. A fruitful collaboration was set up around several current glaciological questions. For example, one question (very fashionable at the moment because of the growing concern about climate change) is the contribution of the Antarctica and Greenland to sea level change. This is a typical problem of data assimilation: how to initialize models (to make forecasts) using available observations? There are other problems with various time (20 or 20,000 years) and space (a glacier or Antarctica) scales. These issues led to the co-supervision of Bertrand Bonan thesis (with Catherine Ritz) and the supervision of several undergraduate and graduate trainees. These various studies are summarized in paragraph §1.2.

Lagrangian data assimilation. This theme is the continuation of my thesis, where I studied the assimilation of positions of floats drifting in the ocean. During my PhD I studied the feasibility of the assimilation problem with a realistic ocean model, but in an idealized configuration. To include the method into operational systems, we wanted to generalize it to a more realistic model, the NEMO code. When I arrived in Grenoble, Arthur Vidard (INRIA MOISE) and I have therefore co-supervised Claire Chauvin during her postdoc. Her job was to set up the Lagrangian assimilation in a more general framework: within the ocean code NEMO in a configuration closer to operational oceanography. This work is summarized in section §1.3.

Image sequences assimilation. This theme was already studied in the MOISE team when I arrived, around the group of François-Xavier Le Dimet and Arthur Vidard (with PhD student Innocent Souopgui and post-doc fellow Olivier Titaud). Given the close link between Lagrangian data and image sequences, I was naturally interested. Indeed, an image sequence closely resembles a collection of Lagrangian tracers moving in the flow. Some operational images assimilation methods are actually based on Lagrangian tracking of some structures. Unlike these methods, we aim to perform direct assimilation of images without resorting to the use of pseudo-observations. In particular, we explored different observation operators, some based on multi-scale decomposition (wavelets, curvelets), other on gradients. With Arthur Vidard we supervised the PhD thesis of Vincent Chabot on this subject, and a new thesis should begin shortly. This work is summarized in paragraph §1.4.

[1] EDGe: Dynamics of flow and physics of the deformation of the Ice

In the second part, I present the theoretical and methodological aspects of my work. The idea this time is to focus on more theoretical issues, and study them on simpler models (Burgers, transport, Venturi, waves, ...).

Sensitivity analysis and model reduction. When Clémentine Prieur arrived in the MOISE team in 2008, we wanted to set up a collaboration on topics mixing both deterministic and stochastic aspects. E.g. I was interested in the following question: given a model with many unknown input parameters (ice or ocean for example), and a number of available observations, how to choose the parameters to be identified? Indeed, the conservative approach would be to assimilate every unknown parameter, but at the cost of a large computational effort. It is sometimes advantageous to restrict the control to a few well-chosen parameters, to which the model is the most sensitive. This is typically a sensitivity analysis problem: to find the input parameter that has the most influence on the model outputs uncertainty. Global sensitivity analysis, especially Sobol indices, is a way to answer this question. The only problem is that numerical methods of indices computation generally involve Monte-Carlo methods and therefore require a very large number of model runs. This is of course unthinkable in practice, therefore our second line of research: model reduction. The idea is to replace the model by a meta-model, approximate but faster. The questions that guided us in this work were the following: how to effectively reduce a model? How to quantify the error on Sobol indices when the model is replaced by the metamodel? These issues have motivated the PhD thesis of Alexander Janon, co-supervised with Clémentine Prieur, and the results are presented in paragraphs §2.1 (model reduction) and §2.2 (sensitivity analysis with reduced models).

Back and Forth Nudging (BFN). When I was a PhD student in Nice, Jacques Blum and Didier Auroux jointly developed a new algorithm for data assimilation: the Back and Forth Nudging. Forward nudging is to add a feedback to the observations in the model equations. This method is quite old but very simple to implement, and gives good results when the number of observations is sufficient. The backward nudging does the same thing, but on the backward model equation. The BFN consists in iterating the forward and backward nudging steps. Like many people at the time, I was both impressed with the positive results and appalled by the idea of changing the direction of time in the models (which most of the time contain diffusion terms). So with Didier Auroux and Jacques Blum, we studied the BFN in more details and proposed improvements. These results are presented in Section §2.3.

Numerical HUM method. Shortly after my departure from Nice, Gilles Lebeau (Nice) asked me to collaborate on a control problem for the wave equation. For this well-known problem, the HUM method gives a necessary and sufficient condition for the controllability of the equation and gives the expression of the control operator. Gilles Lebeau had shown theoretical results on the properties of this operator, and he wanted to observe them numerically. We have done experimental work, implementing a robust Galerkin method to solve the control problem, and using it to highlight the theoretical results, and issue new conjectures about the problem. This work is presented in Section §2.4. It is of course farther from data assimilation, but it is still related in the sense that it allowed me to better understand some difficulties encountered in assimilation (non-controllability, numerical instabilities due to waves, etc.).

Personal publications

Works in relation with my PhD thesis are in gray, later works in color.

- PhD thesis:

[0] MN, Modélisation mathématique et assimilation de données lagrangiennes pour l'océanographie, Université de Nice Sophia-Antipolis (2005)

- Articles:

[1] MN, Variational assimilation of Lagrangian data in oceanography, *Inverse Problems* (2006) 22 245–263

[2] MN, Regularity results for the Primitive Equations of the ocean. Asymptotic Analysis, IOS Press (2006), 50 3/4, pp. 293–324

[3] MN, Optimal control of the Primitive Equations of the Ocean with Lagrangian observations. Control Optimisation and Calculus of Variations, EDP Sciences (2010) 16 2, pp. 400–419

[4] G. Lebeau, MN, Experimental Study of the HUM Control Operator for Linear Waves. Experimental Mathematics, A K Peters (2010) 19 (1), pp. 93–120.

[5] D. Auroux, MN. The Back and Forth Nudging algorithm for data assimilation problems: theoretical results on transport equations. ESAIM: Control, Optimisation and Calculus of Variations, EDP Sciences (2012) 18 2, pp. 318–342.

[6] M. Jay-Allemand, F. Gillet-Chaulet, O. Gagliardini, MN. Investigating changes in basal conditions of Variegated Glacier prior to and during its 1982-1983 surge. Cryosphere, Copernicus Publications on behalf of EGU (2011) 5 3, pp. 659-672.

[7] D. Auroux, J. Blum, MN. Diffusive Back and Forth Nudging algorithm for data assimilation. Comptes Rendus Mathématique, Elsevier (2011) 349 (15-16), pp. 849-854.

[8] F. Gillet-Chaulet, O. Gagliardini, H. Seddik, MN, G. Durand, C. Ritz, T. Zwinger, R. Greve, D. G. Vaughan. Greenland Ice Sheet contribution to sea-level rise from a new-generation ice-sheet model. The Cryosphere, EGU (2012) 6 6, pp. 1561-1576.

[9] A. Janon, MN, C. Prieur. Uncertainties assessment in global sensitivity indices estimation from metamodels. International Journal for Uncertainty Quantification, Begell House Publishers (2012).

[10] A. Janon, MN, C. Prieur. Certified reduced-basis solutions of viscous Burgers equation parametrized by initial and boundary values. ESAIM: Mathematical Modelling and Numerical Analysis, EDP Sciences (2013) 47 2, pp. 317-348.

[11] A. Janon, T. Klein, A. Lagnoux-Renaudie, MN, C. Prieur. Asymptotic normality and efficiency of two Sobol index estimators. ESAIM: Probability and Statistics, EDP Sciences (2013)

- Conference proceedings:

[12] MN, J. Blum, Assimilation de données lagrangiennes pour l'océanographie. *Colloque National sur l'Assimilation de Données, Toulouse* (2006)

[13] MN, Assimilation of Lagrangian Data into an ocean model. Wiley, Special Issue: Sixth International Congress on Industrial Applied Mathematics (ICIAM07) and GAMM Annual Meeting, Zürich (2007) pp. 1026503-1026504, Proceedings in Applied Mathematics and Mechanics.

[14] MN, G. Lebeau. Experimental study of the HUM control operator for waves. PICOF'10 V International Conference on Inverse Problems, Control and Shape Optimization (2010) Cartagena, Spain.

[15] A. Janon, MN, C. Prieur. Certified metamodels for sensitivity indices estimation. SMAI 2011, Guidel, France. EDP Sciences, Congrès National de Mathématiques Appliquées et Industrielles, 35, pp. 234-238 (2012) ESAIM Proceedings.

[16] MN. Introduction to Data Assimilation. EFIDIR Spring School (2011) Les Houches, Chamonix, France.

[17] MN, B. Bonan, O. Ozenda, C. Ritz. Data assimilation in glaciology. Advanced Data Assimilation for Geosciences (2012) Les Houches, France.

[18] A. Janon, T. Klein, A. Lagnoux, MN, C. Prieur. Normalité asymptotique et efficacité dans l'estimation des indices de Sobol. 44èmes journées de statistique (2012) Bruxelles, Belgium.

[19] N. Papadakis, V. Chabot, A. Makris, MN, A. Vidard. Assimilation d'images et de structures. Colloque GRETSI, Brest (2013).

[20] V. Chabot, MN, A. Vidard, N. Papadakis, Assimilation directe de séquences d'images de traceur passif : application aux équations de Saint-Venant. Colloque GRETSI, Brest (2013).

- Submitted papers:

[21] A. Janon, MN, C. Prieur. Goal-oriented error estimation for reduced basis method, with application to certified sensitivity analysis. (2012)

[22] B. Bonan, MN, C. Ritz, V. Peyaud. An ETKF approach for initial state and parameter estimation in ice sheet modelling. (2013)

- In preparation:

  [23] V. Chabot, MN, N. Papadakis, A. Vidard. Assimilation of image structures in the presence of observation error. (2013)

- Research reports:

  [24] C. Chauvin, MN, A. Vidard, Pierre-Antoine Bouttier. Assimilation of Lagrangian Data in an operational framework. (2010) pp. 27. RR-7840

  [25] C. Chauvin, MN, A. Vidard. Assimilation of Lagrangian Data in NEMOVAR. (2010) pp. 15

- Outreach paper:

  [26] MN. De la glace à la mer. Matapli, SMAI (2013) 100

1

Data assimilation for the environment

Contents

1.1 Data assimilation methods

In this paragraph, we present the main data assimilation methods we will use later on. The references can be found in the bibliography, page 72.

1.1.1 Introduction

What is data assimilation?

Data assimilation is the science of "fruitful compromises": it offers methods to combine optimally ("optimally" should be defined precisely) every source of available information about a system: mathematical equations (describing the physical or biological system), observations (measures, data), error statistics (observation errors, model errors...). These information sources are often heterogeneous: in nature, spatial and temporal distributions.

Data assimilation (DA) was initially introduced for initial state estimation in weather forecasting. Today it has many application domains (weather forecasting still, but also oceanography, sismography and oil search, nuclear fusion, medicine, glaciology, building, agronomy, ...). Similarly, initial state estimation is not the only aim of DA, we also look for other parameters (boundary conditions, forcings, numerical parameters, physical law parameters, domain and shape, ...).

In any cases, the idea is to solve an inverse problem about a (physical or other) system whose input parameters are partially unknown, and whose outputs are (partially, indirectly) observed. The inverse problems we faced in DA generally share the following characteristics: complex systems, indirect, sparse (in space and/or time) and error-prone observations, ill-posed problem (underdetermined or overdetermined).

BLUE

There are two major classes of data assimilation. One is based on the optimal statistical estimation theory and is the foundation of the Kalman filtering methods. The other is based on optimal control theory, and leads to variational methods. Under certain restrictive assumptions these two methods are equivalent, as we will see briefly.

We consider the following inverse problem: estimate $\boldsymbol{x}^t \in \mathbb{R}^n$ knowing observations $\boldsymbol{y}^o \in \mathbb{R}^m$ such that

$$\boldsymbol{y}^o = \boldsymbol{H}\boldsymbol{x}^t + \boldsymbol{\epsilon}^o$$

where $\boldsymbol{H}$ is the observation operator (linear) and $\boldsymbol{\epsilon}^o$ is the observation error vector, supposedly unbiased (ie expectancy $\mathbb{E}(\boldsymbol{\epsilon}^o) = 0$), with known covariance matrix $\boldsymbol{R} = \mathbb{E}(\boldsymbol{\epsilon}^o \boldsymbol{\epsilon}^{oT})$. It is also assumed that we have a background $\boldsymbol{x}^b$:

$$\boldsymbol{x}^b = \boldsymbol{x}^t + \boldsymbol{\epsilon}^b$$

where the background error is supposed to be without bias, with known covariance matrix $\boldsymbol{P}^b = \mathbb{E}(\boldsymbol{\epsilon}^b \boldsymbol{\epsilon}^{bT})$ and uncorrelated to the observation error. We then seek the BLUE (Best Linear Unbiased Estimator), ie $\boldsymbol{x}^a$ such that the estimator is:

- linear: $\boldsymbol{x}^a = \boldsymbol{L}\boldsymbol{y}^o$;
- unbiased: $E(\boldsymbol{x}^a - \boldsymbol{x}) = 0$, ie $\boldsymbol{L}\boldsymbol{H} = \boldsymbol{I}$;
- of minimal variance $\mathrm{Tr}(\boldsymbol{P}^a)$.

where $\boldsymbol{P}^a$ is the matrix of analysis errors $\boldsymbol{\epsilon}^a = \boldsymbol{x}^a - \boldsymbol{x}^t$. The solution to this problem is given by the formula

$$\boldsymbol{x}^a = \boldsymbol{x}^b + \boldsymbol{K}(\boldsymbol{y}^o - \boldsymbol{H}\boldsymbol{x}^b)$$

where $\boldsymbol{K}$ is the Kalman gain matrix:

$$\boldsymbol{K} = (\boldsymbol{P}^{b^{-1}} + \boldsymbol{H}^T\boldsymbol{R}^{-1}\boldsymbol{H})^{-1}\boldsymbol{H}^T\boldsymbol{R}^{-1} = \boldsymbol{P}^b\boldsymbol{H}^T(\boldsymbol{R} + \boldsymbol{H}\boldsymbol{P}^b\boldsymbol{H}^T)^{-1}$$

In this case, the analysis error covariance matrix is

$$\boldsymbol{P}^a = (\boldsymbol{I} - \boldsymbol{K}\boldsymbol{H})\boldsymbol{P}^b$$

The same estimate is obtained if one seeks the minimizer $\hat{x}$ of the following cost function:

$$\begin{aligned} J(\boldsymbol{x}) &= \tfrac{1}{2}(\boldsymbol{x} - \boldsymbol{x}^b)^T\boldsymbol{P}^{b^{-1}}(\boldsymbol{x} - \boldsymbol{x}^b) + \tfrac{1}{2}(\boldsymbol{H}\boldsymbol{x} - \boldsymbol{y}^o)^T\boldsymbol{R}^{-1}(\boldsymbol{H}\boldsymbol{x} - \boldsymbol{y}^o) \\ &= \tfrac{1}{2}\|\boldsymbol{x} - \boldsymbol{x}^b\|^2_{\boldsymbol{P}^{b^{-1}}} + \tfrac{1}{2}\|\boldsymbol{H}\boldsymbol{x} - \boldsymbol{y}^o\|^2_{\boldsymbol{R}^{-1}} \\ &= J^b(\boldsymbol{x}) + J^o(\boldsymbol{x}) \end{aligned}$$

The aim of filtering methods is to directly calculate the Kalman gain matrix, while variational methods aim to solve this last minimization problem thanks to optimization tools. We give more details on this in the following paragraphs.

1.1.2 Variational methods

The variational methods solve the inverse problem by directly minimizing the cost function, usually by a gradient descent method. The gradient calculation is done by the adjoint method, which comes from the theory of PDE optimal control (Lions, 1968). We briefly recall below what it is.

Adjoint method

The adjoint method (Lions, 1968) was introduced for the problem of controlling the initial condition in meteorology by Le Dimet (1982); Le Dimet and Talagrand (1986). We formally recall what it is below. The unknown function is the state of the system (temperature, pressure, wind, humidity) at the initial time, denoted U. The state vector $X(t)$ then satisfies a system of partial differential equations (called the model):

$$\begin{cases} \dfrac{dX}{dt} = M(X), & \text{dans } \Omega \times [0,T] \\ X(t=0) = U \end{cases}$$

where we detailed only the time derivative. Spatial differential operators in Ω and boundary conditions are contained in M. It is also assumed that observations of the state $X(t)$ are available

$$Y^o = HX + \boldsymbol{\epsilon}^o$$

where Y^o is in a space Ω^o that we endow (to simplify the writing) with the norm and the scalar product L^2. We therefore seek to minimize the following cost function, which measures the misfit to the observations:

$$J(U) = \frac{1}{2}\int_0^T \|HX - Y^o\|^2\, dt$$

The minimization of J by a descent method requires its gradient. We begin by expressing the derivative of J in U in the direction u:

$$\hat{J}[U](u) = \lim_{\alpha\to 0} \frac{J(U+\alpha u) - J(U)}{\alpha} = \int_0^T (\hat{X}, H^T(HX - Y))\, dt$$

where $\hat{X}$ is the directional derivative of X in U in the direction u

$$\hat{X} = \hat{X}[U](u) = \lim_{\alpha\to 0} \frac{X(U+\alpha u) - X(U)}{\alpha}$$

We know that $\hat{X}$ satisfies the so-called *tangent linear model* equation:

$$\begin{cases} \dfrac{d\hat{X}}{dt} = \left[\dfrac{\partial M}{\partial X}\right]\hat{X} \\ \hat{X}(t=0) = u \end{cases}$$

Then the (backward) equation of the *adjoint model* is introduced:

$$\begin{cases} \dfrac{dP}{dt} + \left[\dfrac{\partial M}{\partial X}\right]^T P = H^T(HX - Y) \\ P(t=T) = 0 \end{cases}$$

that allows easily to express the gradient of J:

$$\hat{J}[U](u) = \int_0^T \left(\hat{X}, \frac{dP}{dt} + \left[\frac{\partial M}{\partial X}\right]^T P\right) = -(u, P(0)) = (\nabla J_U, u) \quad \Rightarrow \quad \nabla J_U = -P(0)$$

This method is quite generic can also be applied in other cases: discrete time/space model, with other controls than initial condition, taking into account the error covariance, etc.

Major variational algorithms

In variational assimilation, the background error covariance matrix is typically denoted $\boldsymbol{B}$ rather than $\boldsymbol{P}^b$, so we will use this notation in this paragraph.

4D-Var. The reference algorithm is called 4D-Var. It is classically formulated for the control of the initial condition $\boldsymbol{x}$, knowing distributed in time observations $\boldsymbol{y}_i^o$, as in the optimal control problem described above. The 4D-Var cost function is as follows:

$$J(\boldsymbol{x}) = \frac{1}{2}\|\boldsymbol{x} - \boldsymbol{x}^b\|^2_{\boldsymbol{B}^{-1}} + \frac{1}{2}\sum_{i=1}^N \|\boldsymbol{H}_i\boldsymbol{x}_i - \boldsymbol{y}_i^o\|^2_{\boldsymbol{R}_i^{-1}}$$

The first term is the background term, it plays a double role. First it contains the a priori information that is available on the system, namely a *background* $\boldsymbol{x}^b$ of the desired estimator and statistical error covariance information via the $\boldsymbol{B}$ matrix. Then it mathematically plays a regularising role, because in general the problem of minimizing the deviation from the observations alone is ill-posed (non-uniqueness, no continuity with the data).
The second term, which contains the misfit to the data, is called the observation term. The sum is over the indices i, which represent various observation times, which are associated with an observation vector $\boldsymbol{y}_i^o$, as well as some knowledge of the observation error statistics through matrices $\boldsymbol{R}_i$. The linear operator $\boldsymbol{H}_i$ is the map between the state variable $\boldsymbol{x}_i$ of the model at time i and the observation vector $\boldsymbol{y}_i^o$. Here we look for the initial condition of a model, knowing observations distributed over a given time window. The state of the system at times of observation, $\boldsymbol{x}_i$ is related to the initial condition $\boldsymbol{x}$ by the (linear) evolution model:

$$\boldsymbol{x}_i = \boldsymbol{M}_{0\to i}\boldsymbol{x} = \boldsymbol{M}_{i-1\to i}\boldsymbol{M}_{i-2\to 1}...\boldsymbol{M}_{1\to 2}\boldsymbol{M}_{0\to 1}\boldsymbol{x} = \boldsymbol{M}_i\boldsymbol{M}_{i-1}...\boldsymbol{M}_2\boldsymbol{M}_1\boldsymbol{x}$$

where to simplify we use the notation $\boldsymbol{M}_k = \boldsymbol{M}_{k-1\to k}$ for one model time step, maping $\boldsymbol{x}_{k-1}$ onto $\boldsymbol{x}_k$. We can thus rewrite the cost function in expanding the dependence in $\boldsymbol{x}$ (recall that $\boldsymbol{x}$ is the initial state, ie $\boldsymbol{x} = \boldsymbol{x}_0$):

$$J(\boldsymbol{x}) = \frac{1}{2}\|\boldsymbol{x} - \boldsymbol{x}^b\|^2_{\boldsymbol{B}^{-1}} + \frac{1}{2}\sum_{i=1}^{N}\|\boldsymbol{H}_i\boldsymbol{M}_i\boldsymbol{M}_{i-1}...\boldsymbol{M}_2\boldsymbol{M}_1\boldsymbol{x} - \boldsymbol{y}_i^o\|^2_{\boldsymbol{R}_i^{-1}}$$

We can then express the gradient of J:

$$\nabla J(\boldsymbol{x}) = \boldsymbol{B}^{-1}(\boldsymbol{x} - \boldsymbol{x}^b) - \sum_{i=1}^{N}\boldsymbol{M}_1^T\dots\boldsymbol{M}_{i-1}^T\boldsymbol{M}_i^T\boldsymbol{H}_i^T\boldsymbol{R}_i^{-1}(\boldsymbol{y}_i^o - \boldsymbol{H}_i\boldsymbol{M}_i\boldsymbol{M}_{i-1}\dots\boldsymbol{M}_1\boldsymbol{x})$$

which is traditionally rewritten using the innovation vectors $\boldsymbol{d}_i$:

$$\boldsymbol{d}_i = \boldsymbol{y}_i^o - \boldsymbol{H}_i\boldsymbol{M}_i\boldsymbol{M}_{i-1}\dots\boldsymbol{M}_1\boldsymbol{x}$$

as follows:

$$\nabla J(\boldsymbol{x}) = \boldsymbol{B}^{-1}(\boldsymbol{x} - \boldsymbol{x}^b) - \boldsymbol{M}_1^T\left[\boldsymbol{H}_1^T\boldsymbol{R}_1^{-1}\boldsymbol{d}_1 + \boldsymbol{M}_2^T\left[\boldsymbol{H}_2^T\boldsymbol{R}_2^{-1}\boldsymbol{d}_2 + \ldots + \boldsymbol{M}_n^T\boldsymbol{H}_n^T\boldsymbol{R}_n^{-1}\boldsymbol{d}_n\right]\right]$$

This factorization shows that we can compute the gradient of J with one direct integration model (to compute the vectors $\boldsymbol{d}_i$) and the adjoint model integration.
This is the basis of the 4D-Var algorithm that does so, from a starting point for $\boldsymbol{x}$: calculate J and ∇J, do one descent method step to minimize J, update $\boldsymbol{x}$ and so on.

3D-Var and 3D-FGAT. Similarly, when the model does not depend on time, the 3D-Var algorithm proceeds in the same way to minimize the cost function:

$$J(\boldsymbol{x}) = \frac{1}{2}\|\boldsymbol{x} - \boldsymbol{x}^b\|^2_{\boldsymbol{B}^{-1}} + \frac{1}{2}\|\boldsymbol{H}\boldsymbol{x} - \boldsymbol{y}^o\|^2_{\boldsymbol{R}^{-1}},\ \text{with}\ \nabla J(\boldsymbol{x}) = \boldsymbol{B}^{-1}(\boldsymbol{x} - \boldsymbol{x}^b) - \boldsymbol{H}^T\boldsymbol{R}^{-1}\boldsymbol{d}$$

with $\boldsymbol{d} = \boldsymbol{y}^o - \boldsymbol{H}\boldsymbol{x}$. This algorithm is also used with evolution models, assuming that all observations are made at the initial time. The cost function can be written as

$$J(\boldsymbol{x}) = \frac{1}{2}\|\boldsymbol{x} - \boldsymbol{x}^b\|^2_{\boldsymbol{B}^{-1}} + \frac{1}{2}\sum_{i=1}^{N}\|\boldsymbol{H}\boldsymbol{x} - \boldsymbol{y}_i^o\|^2_{\boldsymbol{R}^{-1}}$$

As it is unsatisfactory to compare an observation at time i with the model state at the initial time, there is a variant called the 3D-FGAT (first guess at appropriate time), which is written as:

1. Compute the innovation vector thanks to the direct model:
$$\boldsymbol{d}_i = \boldsymbol{y}_i^o - \boldsymbol{H}_i \boldsymbol{M}_i \boldsymbol{M}_{i-1} \dots \boldsymbol{M}_1 \boldsymbol{x}$$
2. Compute J:
$$J = \frac{1}{2} \|\boldsymbol{x} - \boldsymbol{x}^b\|^2_{\boldsymbol{B}^{-1}} + \frac{1}{2} \sum_{i=1}^{N} \|\boldsymbol{d}_i\|^2_{\boldsymbol{R}_i^{-1}}$$
(note that this is the 4D-Var cost function)
3. Compute an approximation of ∇J thanks to the adjoint observation operator H^T:
$$\nabla J(x) = \boldsymbol{B}^{-1}(\boldsymbol{x} - \boldsymbol{x}^b) - \sum_{i=1}^{N} \boldsymbol{H}_i^T \boldsymbol{R}_i^{-1} \boldsymbol{d}_i$$

3D-FGAT is a variant of the 4D-Var, in which the adjoint operators $\boldsymbol{M}_i^T$ is replaced by the identity. This greatly simplifies the implementation since then only the adjoint of the observation operator is required.

1.1.3 Practical variational assimilation

The practical implementation of variational methods require many ingredients, which are all currently subjects of active research. We will review the major ones quickly.

Effective adjoint implementation

Obtaining the adjoint model, to get the gradient, can be done in two ways. The first method, which I call *continuous adjoint*, is to write the continuous adjoint equations (as was done above) and then discretise them. The second approach, which I call *discrete adjoint*, is to first write the discrete direct model and then calculate the adjoint of the discrete code.

These two methods are not equivalent, especially when the numerical schemes used are not symmetrical. Thus, continuous adjoint will not be exactly the adjoint operator of the direct model, while the discrete adjoint will be fine. The "good" approach is therefore that of the discrete adjoint which computes the gradient of the discrete cost function.

However, the calculation and implementation of the discrete adjoint can be complex and tedious, and it may happen that for convenience we choose the continuous adjoint, at the price of an approximate gradient.

However, there are tools that automate the writing of the adjoint code, called automatic differentiation tools, such as the software Tapenade (2002); Hascoet and Pascual (2013). These tools are powerful, always improving, and can now derive large computer codes in FORTRAN. It should be mentioned, however, that these tools can not be used completely in black box mode and require a lot of prep work on the direct code. We refer to Giering and Kaminski (1998); Griewank and Walther (2008) for details on automatic differentiation.

Nonlinearities

Classical algorithms are written for linear models and observation operators, but in practice they are rarely linear. To distinguish from the quadratic case we use the notations $\mathcal{J}$ for cost and $\mathcal{H}_i$ and $\mathcal{M}_i$ for the nonlinear observation and model operators. In that case the BLUE assumptions are not satisfied, so we lose the optimality of the algorithms and the variational / filtering equivalence. We can still continue to use the previous algorithms, the cost function writes:

$$\mathcal{J}(\boldsymbol{x}) = \frac{1}{2}\|\boldsymbol{x} - \boldsymbol{x}^b\|^2_{\boldsymbol{B}^{-1}} + \frac{1}{2}\sum_{i=1}^{N} \|\mathcal{H}_i\mathcal{M}_i\mathcal{M}_{i-1}...\mathcal{M}_2\mathcal{M}_1\boldsymbol{x} - \boldsymbol{y}_i^o\|^2_{\boldsymbol{R}_i^{-1}}$$

In practice we use two types of algorithms to minimize $\mathcal{J}$:

1. we either directly minimizes the non-quadratic functional with Quasi-Newton methods, using the gradient

   $$\nabla\mathcal{J}(\boldsymbol{x}) = \boldsymbol{B}^{-1}(\boldsymbol{x} - \boldsymbol{x}^b) - \sum_{i=1}^{N} \boldsymbol{M}_1^T \dots \boldsymbol{M}_{i-1}^T \boldsymbol{M}_i^T \boldsymbol{H}_i^T \boldsymbol{R}_i^{-1}(\boldsymbol{y}_i^o - \mathcal{H}_i\mathcal{M}_i\mathcal{M}_{i-1}\dots\mathcal{M}_1\boldsymbol{x})$$

   where the adjoint operators are the transposed linearized operators (commonly called tangent operators in the DA literature);

2. or we use so-called incremental algorithms which consists in assuming $\boldsymbol{x}$ near a reference $\boldsymbol{x}^r$, $\boldsymbol{x} = \boldsymbol{x}^r + \boldsymbol{\delta x}$, and in linearizing to get an quadratic cost function approaching $\mathcal{J}$:

   $$\mathcal{J}_{\text{quad}}(\boldsymbol{x}) = \frac{1}{2}\|\boldsymbol{\delta x}\|^2_{\boldsymbol{B}^{-1}} + \frac{1}{2}\sum_{i=1}^{N} \|\boldsymbol{d}_i - \boldsymbol{H}_i\boldsymbol{M}_i\boldsymbol{M}_{i-1}...\boldsymbol{M}_1\boldsymbol{\delta x}\|^2_{\boldsymbol{R}_i^{-1}}$$

   where $\boldsymbol{d}_i = \boldsymbol{y}_i^o - \boldsymbol{H}_i\boldsymbol{M}_i\boldsymbol{M}_{i-1}\dots\boldsymbol{M}_1\boldsymbol{x}^r$ and $\boldsymbol{H}$ and $\boldsymbol{M}$ are the linearized operators of $\mathcal{H}$ and $\mathcal{M}$ around the reference trajectory $\boldsymbol{x}^r$. It then proceeds iteratively: minimization of $\mathcal{J}_{\text{quad}}$, the minimizer becomes the new reference $\boldsymbol{x}^r$, linearization of $\mathcal{H}$ and $\mathcal{M}$ around $\boldsymbol{x}^r$, new quadratic function, etc.

Numerical optimisation

Once the discrete model and its gradient (with the adjoint) are available, we proceed to the iterative minimization of the cost function through numerical minimization algorithms. The book by Nocedal and Wright (1999) present current methods, it is our reference for this section, but there are many research papers on the subject. The methods that are used in data assimilation (weather forecasting, oceanography and glaciology) are variants of Newton's method, essentially the methods of Quasi-Newton and Gauss-Newton. The Quasi-Newton method consists in replacing the Hessian operator by an approximation (BFGS method, Broyden-Fletcher-Goldfarb-Shanno). For large scale problems it can be a reduced rank approximation (L-BFGS method, ie limited memory BFGS). The Gauss-Newton method is the incremental algorithm presented just above. The idea is to linearize the nonlinear operators $\mathcal{H}_i$ and $\mathcal{M}_i$, then minimize the quadratic function obtained and update the reference trajectory and again linearize, and iterate the process until convergence. Under certain conditions (that are rarely applicable in practice) the algorithm converges to a minimum of the function $\mathcal{J}$.

Covariance matrices

Background errors covariance matrices $\boldsymbol{B}$ and observation $\boldsymbol{R}$ are needed to implement the algorithms. Since the dimensions of these matrices are very large, they are never stored or defined in matrix form, we generally implement the matrix-vector product associated operator. Their role is very important of course, as can be seen from the formula BLUE:

$$\boldsymbol{x}^a = \boldsymbol{x}^b + \boldsymbol{B}\boldsymbol{H}^T(\boldsymbol{R} + \boldsymbol{H}\boldsymbol{B}\boldsymbol{H}^T)^{-1}(\boldsymbol{y}^o - \boldsymbol{H}\boldsymbol{x}^b)$$

The analysis increment $\boldsymbol{x}^a - \boldsymbol{x}^b$ is in the image of $\boldsymbol{B}$ matrix! The modeling of these matrices is difficult and is the subject of active research. Those are more advanced for the matrix $\boldsymbol{B}$ than for the matrix $\boldsymbol{R}$ (often chosen diagonal). We briefly mention below various ways to do so.

Recall that if $\boldsymbol{\epsilon}^b$ represents the background error (with $\overline{\boldsymbol{\epsilon}^b} = 0$), then $\boldsymbol{B} = \mathbb{E}(\boldsymbol{\epsilon}^b \boldsymbol{\epsilon}^{b^T})$. If we denote by $B_{i,j} = \mathbb{E}(\boldsymbol{\epsilon}^b_i \boldsymbol{\epsilon}^b_j)$ its coefficients, we can write classically

$$\boldsymbol{B} = \boldsymbol{\Sigma}\boldsymbol{C}\boldsymbol{\Sigma}$$

where $\boldsymbol{\Sigma}$ is the diagonal matrix of standard deviations $\sqrt{B_{i,i}}$, and $\boldsymbol{C}$ is the correlation matrix

$$C_{i,j} = \frac{B_{i,j}}{\sqrt{B_{i,i}}\sqrt{B_{j,j}}}$$

The matrix of standard deviations $\boldsymbol{\Sigma}$ can be estimated by statistics on the model states, it has only n coefficients ($\boldsymbol{B}$ has n^2), where n is the dimension of the state vector. One first naive approach is to say that the correlation functions are Gaussian functions depending on the distance between two points:

$$C_{i,j} = c_1 \exp\left(-\frac{d_{i,j}}{c_2}\right)$$

where c_1 and c_2 are normalization coefficients and $d_{i,j}$ is the disctance between the point identified by the index i in the grid and the point identified by the index j, so that the influence of point i on point j decreases with the distance between these points. The method of the diffusion operator (Weaver and Courtier, 2001) improve this idea, by deforming the Gaussian to follow the boundaries of the field, or the flow. This is achieved through a diffusion operator (whose solutions are exactly deformed Gaussian functions).

The problem with the above method is that it produces spatial correlations between two different grid for the same physical variable (temperature, speed, etc.), but no correlation between two different physical variables.
Other methods of producing multivariate $\boldsymbol{B}$ matrices (that is to say, with non-zero correlations between different physical variables) are: reduced basis method, Monte-Carlo (called ensemble methods in DA).
The reduced basis method is to provide a sufficiently rich time series of model states ξ_k, and form the matrix $\boldsymbol{X}$ which contains the columns ξ_k minus their average. A singular value decomposition (or principal component analysis) of the matrix $\boldsymbol{X}\boldsymbol{X}^T$ is then performed:

$$\boldsymbol{X}\boldsymbol{X}^T = \boldsymbol{N}\boldsymbol{\Lambda}\boldsymbol{N}^T$$

where $\boldsymbol{N}$ is the eigenvector matrix and $\boldsymbol{\Lambda}$ the diagonal matrix of the decreasing eigenvalues. The idea is to approximate B using only the first r components (called Empirical Orthogonal Functions in geosciences) of these matrices:

$$\boldsymbol{B} = \boldsymbol{N}_r \boldsymbol{\Lambda}_r \boldsymbol{N}_r^T$$

where $\boldsymbol{N}_r$ is a matrix whose r columns are the r first EOFs and $\boldsymbol{\Lambda}_r$ is a diagonal r by r matrix containing the r largest eigenvalues. In general, $r < 100$, so this formulation of $\boldsymbol{B}$ can be stored in memory and manipulated easily.

Another way to produce a multivariate $\boldsymbol{B}$ matrix is to use an ensemble method (Monte-Carlo). If one has an ensemble of system states $\boldsymbol{x}^1, \ldots, \boldsymbol{x}^p$, we can estimate $\boldsymbol{B}$ by Monte-Carlo

$$\boldsymbol{B} = \frac{1}{p-1} \sum_{j=1}^{p} \left(\boldsymbol{x}^j - \overline{\boldsymbol{x}}\right) \left(\boldsymbol{x}^j - \overline{\boldsymbol{x}}\right)^T$$

where $\overline{\boldsymbol{x}}$ is the average of $\boldsymbol{x}^j$. As before, we then have less expensive computations. The problem is then to calculate wisely the vectors $\boldsymbol{x}^j$ of the ensemble. We refer to the methods of ensemble filtering to see how to choose the ensemble members. Generally, p is of the order of 80 to 100, so that $\boldsymbol{B}$ is elementary to calculate. As with the reduced method, the obtained $\boldsymbol{B}$ matrix is naturally multivariate.

1.1.4 Sequential methods: Kalman filtering

The Kalman filter, as 4D-Var, extends the BLUE analysis to time-dependent problems. The notations are the same as above, except that the Kalman filter naturally takes into account the model error:

$$\boldsymbol{x}_{k+1} = \boldsymbol{M}_{k+1}\boldsymbol{x}_k + \eta_k$$

where η_k is an unbiased noise, uncorrelated in time, with covariance matrix $\boldsymbol{Q}_k$. Note that the 4D-Var also allows the inclusion of the error model, as in Vidard et al. (2000, 2004); Freitag et al. (2012), but the implementation is less natural than the Kalman filter. As for the 4D-Var and BLUE, we also have observations at each time t_k:

$$\boldsymbol{y}_k^o = \boldsymbol{H}_k\boldsymbol{x}_k + \boldsymbol{\epsilon}_k^o$$

We also assume that the observation and model errors are uncorrelated, or $\mathbb{E}(\boldsymbol{\epsilon}_k^o \eta_l^T) = 0$ for all times t_k, t_l. As 4D-Var, the Kalman filter assumes that the operators $\boldsymbol{M}$ and $\boldsymbol{H}$ are linear.

Algorithm

The Kalman filter is composed of a succession of two phases: analysis and prediction. The analysis step at time t_k is a simple application of the BLUE: at this time, there is a background (which is the previous forecast), which we denote $\boldsymbol{x}_k^f$ (exponent f for *forecast*), with covariance matrix $\boldsymbol{P}_k^f$ assumed known. The BLUE analysis is thus rewritten

$$\boldsymbol{x}_k^a = \boldsymbol{x}_k^f + \boldsymbol{K}_k(\boldsymbol{y}_k^o - \boldsymbol{H}_k\boldsymbol{x}_k^f), \quad \boldsymbol{K}_k = \boldsymbol{P}_k^f\boldsymbol{H}_k^T(\boldsymbol{R}_k + \boldsymbol{H}_k\boldsymbol{P}_k^f\boldsymbol{H}_k^T)^{-1}$$

and the analysis error covariance matrix $\boldsymbol{P}_k^a$ is also given by the BLUE:

$$\boldsymbol{P}_k^a = (\boldsymbol{I} - \boldsymbol{K}_k\boldsymbol{H}_k)\boldsymbol{P}_k^f$$

The second step of the Kalman filter is to propagate the analysis to the next observation time, thanks to the model. It is called the prediction/forecast step:

$$\boldsymbol{x}_{k+1}^f = \boldsymbol{M}_{k+1}\boldsymbol{x}_k^a, \quad \boldsymbol{P}_{k+1}^f = \boldsymbol{M}_{k+1}\boldsymbol{P}_{k+1}^a\boldsymbol{M}_{k+1}^T + \boldsymbol{Q}_k$$

Variational equivalence

Under the assumptions of the Kalman filter about errors and linearity of the operators, the 4D-Var and the Kalman filter are equivalent. More precisely, in the absence of model error, on the same time window $[t_0, t_N]$, with the same observations and the same background (ie $\boldsymbol{x}^b = \boldsymbol{x}_0^f$), the analysis of the KF (Kalman Filter) at final time $\boldsymbol{x}_N^a$ coincides with the minimum of the 4D-Var cost function (propagated to time t_N by the model).

Nonlinearites

As for the 4D-Var, in the presence of non-linearities, the algorithm can be extended, at the cost of loss of optimality. We also loose the variational equivalence. The extended Kalman filter is an adaptation of the filter with the non-linear operators $\mathcal{M}_k$ and $\mathcal{H}_k$ and their linearized versions $\boldsymbol{M}_k$ and $\boldsymbol{H}_k$ around $\boldsymbol{x}_k^a$ et $\boldsymbol{x}_k^f$. The analysis is written

$$\boldsymbol{x}_k^a = \boldsymbol{x}_k^f + \boldsymbol{K}_k(\boldsymbol{y}_k^o - \mathcal{H}_k\boldsymbol{x}_k^f), \quad \boldsymbol{K}_k = \boldsymbol{P}_k^f\boldsymbol{H}_k^T(\boldsymbol{R}_k + \boldsymbol{H}_k\boldsymbol{P}_k^f\boldsymbol{H}_k^T)^{-1}, \quad \boldsymbol{P}_k^a = (\boldsymbol{I} - \boldsymbol{K}_k\boldsymbol{H}_k)\boldsymbol{P}_k^f$$

and the forecast step becomes

$$\boldsymbol{x}_{k+1}^f = \mathcal{M}_{k+1}\boldsymbol{x}_k^a, \quad \boldsymbol{P}_{k+1}^f = \boldsymbol{M}_{k+1}\boldsymbol{P}_{k+1}^a\boldsymbol{M}_{k+1}^T + \boldsymbol{Q}_k$$

1.1.5 Ensemble filtering methods

The Kalman filter, even in its extended version, is rarely used as is in geosciences, because the dimensions of the involved matrices are too large. Let us recall that if the dimension of the state space is n (and the observation space dimension is m) then the matrices $\boldsymbol{P}$ and $\boldsymbol{K}$ are of size $n \times n$. In realistic applications (Numerical Weather Prediction – NWP, oceanography), n can be of the order of a million, so these matrices are not storable in practice. An empirical method has been proposed to overcome this problem by Evensen (1994); Burgers et al. (1998): the Ensemble Kalman Filter (EnKF). The theoretical justification is still at its beginning, we can refer to the work of Bocquet (2011) for a solid mathematical interpretation. However, this filter provides quite good results in practice and it is fairly easy to implement, so it is widely used, and there are many variations.

Ensemble Kalman filter algorithm

The idea is to replace the state vector and its covariance matrix by an *ensemble* of vectors $\boldsymbol{x}_k^{(i)}$, $i = 1, \ldots, N_e$, whose first moments provide an estimate of the state vector and the covariance matrix:

$$\overline{\boldsymbol{x}_k} = \frac{1}{N_e}\sum_{i=1}^{N_e}\mathbf{x}_k^{(i)}, \quad \mathbf{P}_k = \frac{1}{N_e - 1}\sum_{i=1}^{N_e}(\boldsymbol{x}_k^{(i)} - \overline{\boldsymbol{x}_k})(\boldsymbol{x}_k^{(i)} - \overline{\boldsymbol{x}_k})^T$$

The forecast step is to propagate each member of the ensemble:

$$\boldsymbol{x}_k^{f^{(i)}} = \mathcal{M}_k\left(\boldsymbol{x}_{k-1}^{a^{(i)}}\right)$$

Then

$$\overline{\boldsymbol{x}_k^f} = \frac{1}{N_e}\sum_{i=1}^{N_e} \boldsymbol{x}_k^{f(i)}, \quad \boldsymbol{P}_k^f = \frac{1}{N_e - 1}\sum_{i=1}^{N_e} (\boldsymbol{x}_k^{f(i)} - \overline{\boldsymbol{x}_k^f})(\boldsymbol{x}_k^{f(i)} - \overline{\boldsymbol{x}_k^f})^T$$

For the analysis, we first create an ensemble of observations for each element of the ensemble:

$$\boldsymbol{y}_k^{o(i)} = \boldsymbol{y}_k^o + \boldsymbol{\epsilon}_k^{o(i)},\ i = 1, .., N_e$$

where the noise $\boldsymbol{\epsilon}_k^{o(i)}$ satisfies

$$\sum_{i=1}^{N_e} \boldsymbol{\epsilon}_k^{o(i)} = 0, \quad \boldsymbol{R}_k = \frac{1}{N_e - 1}\sum_{i=1}^{N_e} (\boldsymbol{\epsilon}_k^{o(i)})(\boldsymbol{\epsilon}_k^{o(i)})^T$$

Then the analysis step is similar to the standard filter for each element of the ensemble:

$$\boldsymbol{x}_k^{a(i)} = \boldsymbol{x}_k^{f(i)} + \boldsymbol{K}_k(\boldsymbol{y}_k^{o(i)} - \boldsymbol{H}_k \boldsymbol{x}_k^{f(i)}), \quad \boldsymbol{K}_k = \boldsymbol{P}_k^f \boldsymbol{H}_k^T (\boldsymbol{R}_k + \boldsymbol{H}_k \boldsymbol{P}_k^f \boldsymbol{H}_k^T)^{-1}$$

The analysed vector and its error covariance matrix are given by the first two moments of the analyses:

$$\overline{\boldsymbol{x}_k^a} = \frac{1}{N_e}\sum_{i=1}^{N_e} \boldsymbol{x}_k^{a(i)}, \quad \boldsymbol{P}_k^a = \frac{1}{N_e - 1}\sum_{i=1}^{N_e} (\boldsymbol{x}_k^{a(i)} - \overline{\boldsymbol{x}_k^a})(\boldsymbol{x}_k^{a(i)} - \overline{\boldsymbol{x}_k^a})^T$$

Inflation and localisation

The ensemble Kalman filter is known to be sensitive to sampling errors due to the small size of the ensemble. Indeed, in practice $N_e < 100$ while $n = 10^4$ to 10^6. This leads to two identified drawbacks, for which two types of remedies have been proposed.

1. The underestimation of variances. To remedy this, we proceed in general to an artificial inflation of the ensemble (Pham et al., 1996; Anderson and Anderson, 1999). That artificially increases the variance of the ensemble:

$$\boldsymbol{x}_k^{f(i)} = \overline{\boldsymbol{x}_k^f} + \rho\left(\boldsymbol{x}_k^{f(i)} - \overline{\boldsymbol{x}_k^f}\right),\ \text{avec } \rho > 1$$

   Other ways to implement inflation exist, in particular using observations.

   This problem is due to the formulation of the filter itself. Indeed Bocquet (2011) showed that another formulation (EnKF-N, taking into account the finite size) eliminates the need for inflation (in fact, this formulation of finite size naturally introduces the optimal inflation required).

2. The appearance of long-range spurious correlations. This problem is solved by a tool called localisation (Hamill et al., 2001; Houtekamer and Mitchell, 2001; Ott et al., 2004). Again there are many formulations, the general idea is to remove the correlations between far away grid points (e.g. covariance matrices can be convolved with localising functions).

Ensemble Transform Kalman filter (ETKF)

The ETKF was introduced by Bishop et al. (2001), it is a particular rewriting of the analysis step of the general Kalman filter using a change of variable (hence the term *transform*), similar to that developed by Pham (1996); Pham et al. (1998); Pham (2001) for SEIK filter. We describe here the version of the filter given by Hunt et al. (2007). We introduce the anomaly matrix $\boldsymbol{X}^f$ whose columns are $[\boldsymbol{x}^{f(1)} - \overline{\boldsymbol{x}^f}, \dots, \boldsymbol{x}^{f(N_e)} - \overline{\boldsymbol{x}^f}]$. Then we look for the $\boldsymbol{P}^a$ matrix as a transformation by the formula:

$$\boldsymbol{P}^a = \boldsymbol{X}^f \widetilde{\boldsymbol{P}}^a \boldsymbol{X}^{f^T}$$

where $\widetilde{\boldsymbol{P}}^a$ is a square matrix of size N_e. We also define the observations of forecasts:

$$\boldsymbol{y}^{f(1)} = \mathcal{H}\left(\boldsymbol{x}^{f(1)}\right), \dots, \boldsymbol{y}^{f(N_e)} = \mathcal{H}\left(\boldsymbol{x}^{f(N_e)}\right)$$

and we define $\overline{\boldsymbol{y}^f}$ as the average of this ensemble and $\boldsymbol{Y}^f$ the matrix of associated anomalies.

The analysis step is then to minimize the following cost function:

$$\mathcal{J}(\boldsymbol{w}) = \frac{N_e - 1}{2}\|\boldsymbol{w}\|^2 + \frac{1}{2}\|\boldsymbol{y}^o - \overline{\boldsymbol{y}^f} - \boldsymbol{Y}^f\boldsymbol{w}\|^2_{\boldsymbol{R}^{-1}}, \quad \boldsymbol{w} \in \mathbb{R}^{N_e}$$

We have an explicit formula for the minimizer:

$$\boldsymbol{w}^a = \widetilde{\boldsymbol{P}}^a \boldsymbol{Y}^{f^T} \boldsymbol{R}^{-1}(\boldsymbol{y}^o - \overline{\boldsymbol{y}^f}), \quad \widetilde{\boldsymbol{P}}^a = \left(\boldsymbol{Y}^{f^T}\boldsymbol{R}^{-1}\boldsymbol{Y}^f + (N_e - 1)\boldsymbol{I}\right)^{-1}$$

And then we get the analysis vectors thanks to their average and the anomaly matrix:

$$\overline{\boldsymbol{x}^a} = \overline{\boldsymbol{x}^f} + \boldsymbol{X}^f\boldsymbol{w}^a, \quad \boldsymbol{X}^a = \boldsymbol{X}^f\left((N_e - 1)\widetilde{\boldsymbol{P}}^a\right)^{\frac{1}{2}}$$

This formulation also admits a version with inflation and localization, we refer to Hunt et al. (2007) and to Bonan (2013) for details.

1.2 Some inverse problems in glaciology

In this paragraph, we present the inverse problems we investigated in collaboration with glaciologists from LGGE. First we explain the main points of ice-sheet dynamics modelling, the major models and some inverse questions. Then we summarise the publications [6] [8] [17] [22] *and the ongoing works.*

1.2.1 Ice-sheet dynamics modelling

Some parts of this paragraph are translated from the (french) outreach paper [26] *I wrote for Matapli 100, on the occasion of "2013 Mathematics for Planet Earth" (MPE 2013). For more details on ice-sheet modelling we refere to the PhD thesis manuscript Bonan (2013).*

Processes involved in ice dynamics

Figure 1.1 presents the various processes occurring in ice dynamics, which we describe below.

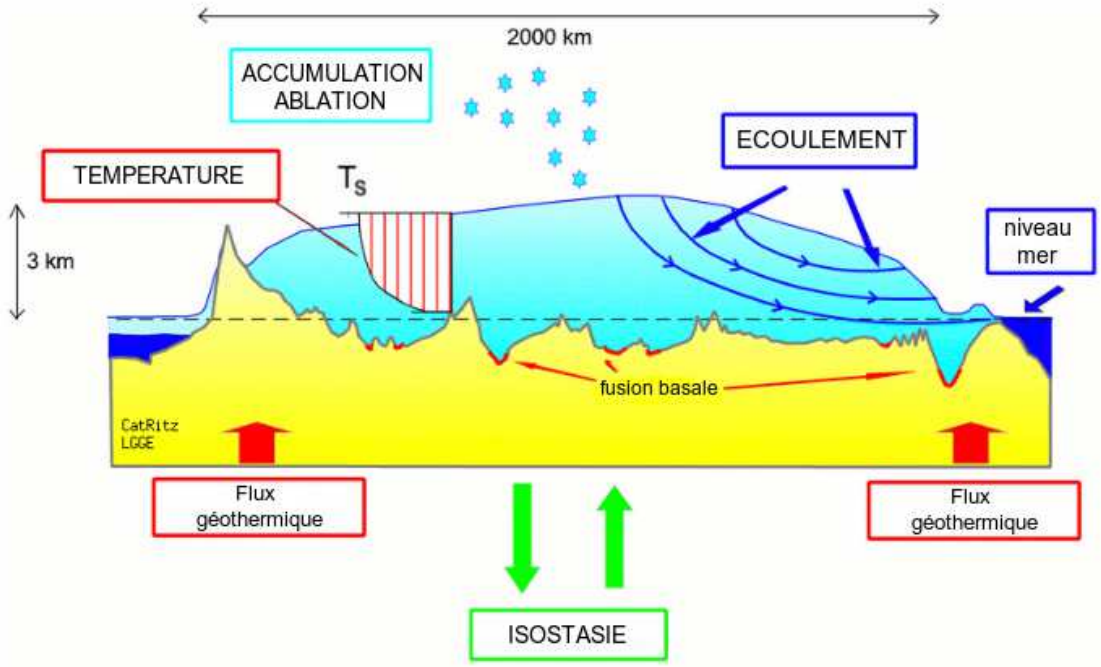

Figure 1.1: Different processes of ice dynamics, represented on a profile of polar ice-sheet. *Source : C. Ritz.*

Flow. Ice is a incompressible non-newtonian fluid, flowing under its own weight. Movies made from daily-captured pictures of a moutain glacier look like frozen river ice

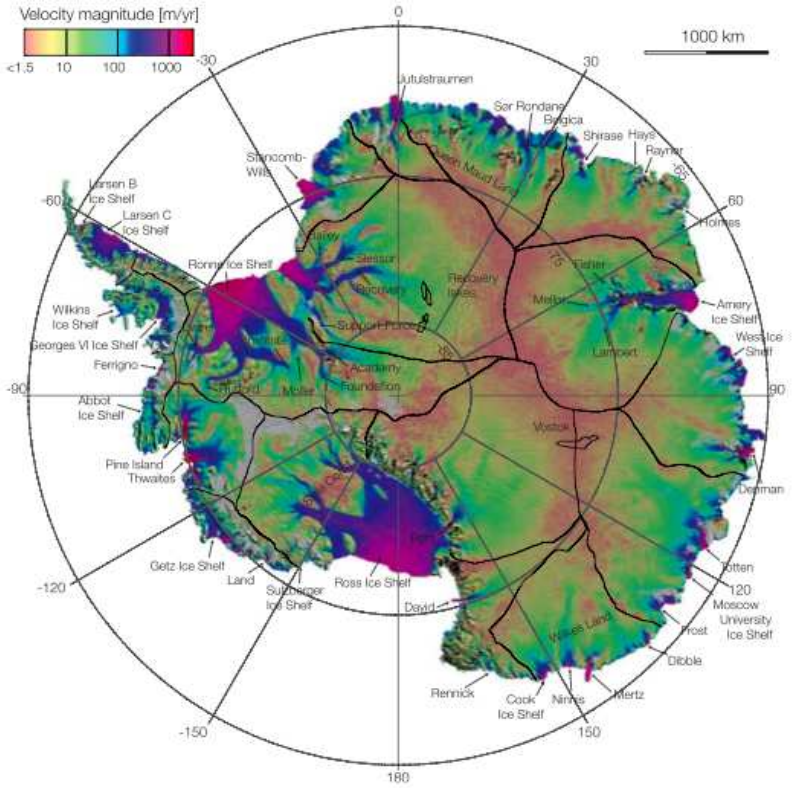

Figure 1.2: Surface ice velocities, from Rignot et al. (2011).

flow[1]. But contrary to water flow, the flow time scales are such that acceleration effects are negligible. "Non-newtonian" means that the ice viscosity non-linearly depends on dynamics. It is given by a viscoplastic constitutive law called the Glen law by glaciologists. It models the material complexity and its deformation tendency. Ice is a really complex material, all the more so as its physical properties vary inside an ice-sheet. Indeed, ice temperature and pressure are unhomogeneous, therefore ice properties change. Moreover, pressure and melting/refrost result in crystalline structure changes, and consequently physical and mechanical properties changes.

Mass balance. The mass balance is the difference between ice accumulation (snow precipiations, surface/crevice/basal refrost) and ice ablation (surface or ground melt, icebergs calving, wind transport). Mass balance estimation is a highly complex problem, depending on many external factors: weather conditions and surface temperature (impacting precipitations, surface melt and wind transport), geothermal flux (impacting basal melt).

Basal boundary conditions. At the bottom of the ice-sheet, either the ice is cold and it sticks to the ground, or it slides. Basal sliding can occur for different reasons. First, when ice is at melt point, a water film forms between the ice and the bedrock, allowing sliding. Second, the ice can be set on a waterlogged sediment, or on rock debris. Third, we can also find subglacial hydrological networks (cavities, rivers, lakes under the ice), on

[1] `https://www.youtube.com/watch?v=HZaknW8m6tI`

which the ice slides. And so on... In the Antarctica and Greenland, the fastest sliding zones can be found on the costlines, in fjord- or canyon-like valleys. Figure 1.2 presents a surface velocity map. We can see numerous and gigantic ice-streams, flowing faster than 10 km/year (14 km/y for the Jakobshavn ice-stream, which has recently produced spectacular icebergs calving episodes[2]). Ice-sheets sometimes extend on the sea, forming gigantic floating platforms, called *ice-shelves*.

Retroaction bestiary. Retroaction, or feedback, occurs when a cause produces an effect which in return acts on the cause. The *small ice-sheet instability* is an example of such feedback: if ice-sheet surface elevation is too small, then its surface temperature increases, leading to a higher melting rate and an increasing surface elevation decrease. The phenomenom can then develop leading to the ice-sheet disappearance.

We can also mention isostasy (or post-glacial rebound). The earth crust deforms and warps downward under the ice weight. This deformation is not negligible: a 3000m high ice-sheet causes a 1000m downward deformation of the bedrock (with a 10,000 years relaxation time). This of course induces a retroaction on the ice-sheet, because it impacts the surface elevation, thus the surface temperature and surface mass balance.

Other retroactions involve the ocean: sealevel impacts ice-sheet, because of lateral boundary conditions (Archimedes principle), and ice-sheets also impact sea-level. Ocean temperature around and below ice-shelves also plays a complex role, and similarly the ice-sheet impacts the neighbouring ocean circulation.

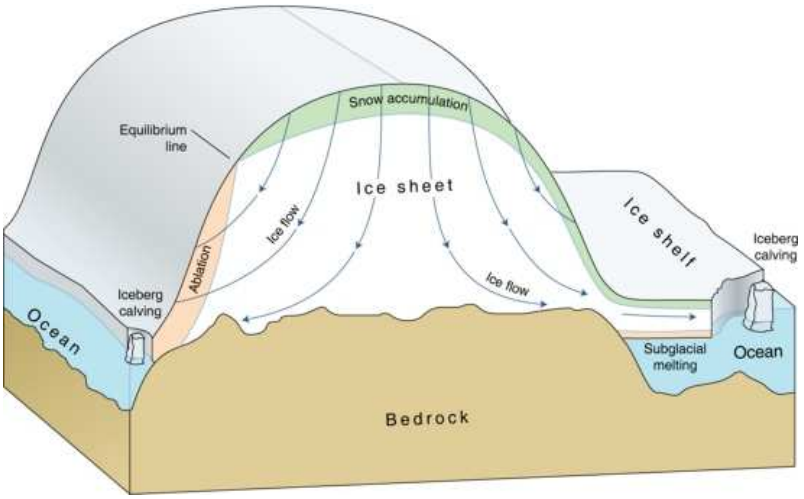

Figure 1.3: Ice sheet geometry of an ice-sheet with ice-shelf. Source `http://www.solcomhouse.com/icecap.htm`

Notations

Spatial coordinates are x, y on the horizontal, z for vertical; axis Oz is upward oriented. The following table presents the geometrical variables:

[2] `http://www.youtube.com/watch?v=hC3VTgIPoGU`

Notation	Description	Unit
$S(x,y,t)$	surface elevation	(m)
$H(x,y,t)$	ice-sheet thickness	(m)
$B(x,y,t)$	ice-sheet base elevation	(m)
$B_{soc}(x,y,t)$	bedrock elevation	(m)

elevations are measured with respect to sea level. Conventionally, where there is no ice we set $B = S = \max(B_{\text{soc}}, 0)$. The ice thickness H is defined by $H = S - B$. Figure 1.3 presents a profile of an ice-sheet.

The following table presents the velocity variables:

Notation	Description	Unit
$\boldsymbol{u}(x,y,z,t)$	ice flow velocity : $\mathbf{u} = (u_x, u_y, u_z)$	$(m.y^{-1})$
$\boldsymbol{U}(x,y,t)$	vertically-averaged horizontal velocity: $\mathbf{U} = (U_x, U_y)$	$(m.y^{-1})$
$\boldsymbol{u}_b(x,y,t)$	basal sliding velocity: $\mathbf{u}_b = (u_{b,x}, u_{b,y})$	$(m.y^{-1})$
$\boldsymbol{u}_s(x,y,t)$	surface velocity: $\mathbf{u}_s = (u_{s,x}, u_{s,y})$	$(m.y^{-1})$

Vertically averaged velocity is defined by

$$\boldsymbol{U}(x,y,t) = \frac{1}{H(x,y,t)} \int_{B(s,y,t)}^{S(x,y,t)} \boldsymbol{u}(x,y,z,t)\, dz$$

and the basal and surface velocities by

$$\boldsymbol{u}_b(x,y,t) = \boldsymbol{u}(x,y,B(x,y,t),t), \quad \boldsymbol{u}_s(x,y,t) = \boldsymbol{u}(x,y,S(x,y,t),t)$$

The following table presents dynamics and viscous law variables:

Notation	Description	Unit
$\eta(x,y,z,t)$	ice viscosity	$(Pa.y^{-1})$
$\overline{\eta}(x,y,t)$	effective (vertically averaged) ice viscosity	$(Pa.y^{-1})$
$\boldsymbol{\sigma}(x,y,z,t)$	strain tensor	(Pa)
$\boldsymbol{\tau}(x,y,z,t)$	deviatoric stresse (rate-of-shear) tensor	(Pa)
$\dot{\boldsymbol{\varepsilon}}(x,y,z,t)$	deformation tensor	(an^{-1})
$\sigma_0 = p(x,y,z,t)$	1/3 of the strain tensor trace	(Pa)
$\tau(x,y,z,t)$	strain rate second invariant	(Pa)

Tensors are matrices, e.g., $\boldsymbol{\sigma} = (\sigma_{ij})$ avec $i,j = x,y,z$. The rate of shear tensor is given by $\boldsymbol{\tau} = \boldsymbol{\sigma} + p\boldsymbol{I}$, where the pressure is

$$p = \frac{\sigma_{xx} + \sigma_{yy} + \sigma_{zz}}{3} = \sigma_0$$

The deformation rate tensor is

$$\dot{\boldsymbol{\varepsilon}}_{i,j} = \frac{1}{2}\left(\frac{\partial u_i}{\partial j} + \frac{\partial u_j}{\partial i}\right), \text{ with } i,j = x,y,z$$

The strain rate second invariant is:

$$\tau = \sqrt{\frac{1}{2}\left(\tau_{xx}^2 + \tau_{yy}^2 + \tau_{zz}^2\right) + \tau_{xy}^2 + \tau_{yz}^2 + \tau_{xz}^2}$$

Finally, the following table presents the various forcings, boundary conditions, and physical parameters:

Notation	Description	Unit
$\boldsymbol{\tau}_b(x,y,t)$	basal drag: $\boldsymbol{\tau}_b = (\tau_{b,x}, \tau_{b,y})$	(Pa)
$\beta(x,y,t)$	basal sliding coefficient	–
$\dot{f}(x,y,t)$	basal melt	$(m.y^{-1})$
$\dot{b}(x,y,t)$	surface mass balance: accumulation - ablation	$(m.y^{-1})$
$T_s(x,y,t)$	surface temperature	°C
$F_{clim}(t)$	climate counterpart of the surface temperature	°C
n	deformation law exponent	-
$\mathcal{B}_{AT,n}$	flow law parameter	$(Pa^{-n}.y^{-1})$
$\boldsymbol{g}$	gravity vector (vecteur : $\boldsymbol{g} = -g\boldsymbol{e}_z$)	9.81 $m.s^{-2}$
ρ_i	ice density	910 $kg.m^{-3}$
ρ_w	water density	1028 $kg.m^{-3}$

Small scale ice modelling: Full-Stokes

The Full-Stokes model aims to represent small scales, both in time (up to 100–200 years) and in space (small mesh size, around or below one kilometer). Because of the small time span, isostasy is ignored: bedrock topography is assumed stationary, as is the ice base. This model is generally used to study watersheds (one glacier or ice-stream, as in [6]), but we also used it for the whole Greenland ice-sheet in [8].

Full Stokes model equations describe a viscous non-newtonian incompressible flow, and are written as follows. First we have the incompressibility equation for mass balance:

$$\text{div } \boldsymbol{u} = 0 \tag{1.1}$$

Then we have the quasi-static equilibrium equation, that is to say Newton law without acceleration terms:

$$\text{div } \boldsymbol{\sigma} + \rho_i \boldsymbol{g} = 0 \tag{1.2}$$

And finally we have the viscous constitutive law from Duval (1979); Lliboutry (1993); Cuffey and Paterson (2010):

$$\boldsymbol{\tau} = 2\eta\dot{\boldsymbol{\varepsilon}}, \quad \frac{1}{\eta} = \mathcal{B}_{AT,n}\tau^{n-1}, \text{ with } n = 1 \text{ and/or } 3 \tag{1.3}$$

in other words:

$$2\dot{\boldsymbol{\varepsilon}} = \left(\mathcal{B}_{AT,1} + \mathcal{B}_{AT,3}\tau^2\right)\boldsymbol{\tau} \tag{1.4}$$

We then have boundary conditions. The free surface evolution writes as:

$$\partial_t S + u_{s,x}\partial_x S + u_{s,y}\partial_y S + u_{s,z} = \dot{b} \tag{1.5}$$

ainsi que

$$\boldsymbol{\sigma}.\boldsymbol{n} = 0 \tag{1.6}$$

where $\boldsymbol{n}$ is the unitary vector orthogonal to the surface. At the base of the ice-sheet, we have a sliding condition:

$$\boldsymbol{t}.(\boldsymbol{\sigma}.n) + \beta\boldsymbol{u}.\boldsymbol{t} = 0, \quad \boldsymbol{u}.\boldsymbol{n} = 0 \tag{1.7}$$

where $\boldsymbol{n}$ and $\boldsymbol{t}$ are the tangent and normal unitary vectors. Finally, we have lateral boundary conditions, depending on whether the ice front is or is not below sea level (at $z = 0$):

$$\boldsymbol{n}^T.\boldsymbol{\sigma}.\boldsymbol{n} = \min(\rho_w g z, 0), \quad \boldsymbol{t}^T.\boldsymbol{\sigma}.\boldsymbol{n} = 0 \tag{1.8}$$

Large scale ice-sheet modelling: Shallow-Ice, Shallow-Shelf

In glaciology we sometimes wish to consider large scales, either in time (up to hundreds of thousands years for paleoclimatology questions) or in space (e.g., for the Antarctica, spanning thousands of kilometers). In this case the Full Stokes model is unpractical because of numerical cost. Therefore we perform classical shallow approximations (as in Navier-Stokes $\rightarrow$ Shallow water), which implies a vertical integration of the equations. Mathematically, justifying the asymptotics is difficult, and studies are few and far between (Schoof and Hindmarsh, 2010; Bassis, 2010).

Combining the incompressibility equation (1.1) with (1.5) and its basal counterpart we get:

$$\partial_t B + u_{b,x}\partial_x B + u_{b,y}\partial_y B + u_{b,z} = \dot{f} \tag{1.9}$$

we obtain the following mass balance equation, called the Shallow-Ice Approximation (SIA) (Hutter, 1983) :

$$\frac{\partial H}{\partial t} = \dot{b} - \dot{f} - \text{div}\ (H\boldsymbol{U}) \tag{1.10}$$

where $\text{div}\ = \partial_x + \partial_y$ is the 2D divergence operator.

Regarding the bedrock evolution there are various kinds of models. The most simple compute the bedrock downward movement as one third of the ice thickness (with a 10,000 relaxation term). More complex models involve coupling with the earth crust dynamics (see (Ritz, 1992)).

The vertically averaged velocity can be split up in two parts:

$$\boldsymbol{U} = \boldsymbol{U}_{\text{def}} + \boldsymbol{U}_{\text{slid}} \tag{1.11}$$

where $\boldsymbol{U}_{\text{def}}$ is the deformation contribution (from Glen's law) and $\boldsymbol{U}_{\text{slid}}$ the sliding counterpart.

We get the deformation velocity after a vertical integration of the constitutive equation (1.4). If the coefficients $\mathcal{B}_{AT,n}$ do not depend on z we get:

$$U_{\text{def,i}} = -\rho g \partial_i S \left[\mathcal{B}_{AT,1}\frac{H^2}{3} + (\rho g)^2\left(\partial_x S^2 + \partial_y S^2\right)\mathcal{B}_{AT,3}\frac{H^4}{5}\right],\ i = x, y \tag{1.12}$$

Regarding the sliding velocity $\boldsymbol{U}_{\text{slid}}$, there exist many approximations. The basic idea is to start from the quasi static equilibrium (1.2) and to use perturbation theory. At order 0 we get the SIA approximation for the sliding velocity:

$$\rho g H \boldsymbol{\nabla} S = \boldsymbol{\tau}_b = -\beta \boldsymbol{U}_{\text{slid}} \tag{1.13}$$

where the basal drag $\boldsymbol{\tau}_b$ is proportional to the sliding velocity:

$$\boldsymbol{\tau}_b = -\beta \boldsymbol{U}_{\text{slid}} \tag{1.14}$$

There exist also more complex sliding laws, e.g., non-linear (Cuffey and Paterson, 2010) but we will not go in further details here.

At order 1, $\boldsymbol{U}_{\text{slid}}$ is given as the solution of a non-linear elleiptic equation, called the Shallow-Shelf Approximation (SSA):

$$\begin{cases} \dfrac{\partial}{\partial x}\left(2\overline{\eta}H\left(2\partial_x U_{\text{slid,x}} + \partial_y U_{\text{slid,y}}\right)\right) + \dfrac{\partial}{\partial y}\left(\overline{\eta}H\left(\partial_y U_{\text{slid,x}} + \partial_x U_{\text{slid,y}}\right)\right) &= \rho g H \partial_x S - \tau_{b,x} \\ \dfrac{\partial}{\partial y}\left(2\overline{\eta}H\left(2\partial_y U_{\text{slid,y}} + \partial_x U_{\text{slid,x}}\right)\right) + \dfrac{\partial}{\partial x}\left(\overline{\eta}H\left(\partial_y U_{\text{slid,x}} + \partial_x U_{\text{slid,y}}\right)\right) &= \rho g H \partial_y S - \tau_{b,y} \end{cases} \tag{1.15}$$

Boundary conditions are complex, in particular in 2D. We sometimes consider kinematic (null velocity) or dynamic (if a forces sum is possible, e.g. at the ice/water front). We refer the reader to Rommelaere (1997); Peyaud (2006) for the details about modelling and implementation of such conditions.

Other complex points are the surface/basal mass balances $\dot{b}$ and $\dot{f}$. At the base $\dot{f}$ measures the melt. Simple models set f as a constant number, more complex modelling involves coupling with temperature (geothermal flux) and/or subglacial hydrology. At the ice surface $\dot{b}$ is the net sum of accumulation (precipitation) and ablation (melt):

$$\dot{b} = \mathrm{Acc} + \mathrm{Abl} \tag{1.16}$$

In realistic frameworks, it is necessary to have good data for $\dot{b}$. To do so we can either use a climate model, or observations. This highly complex question of observing/modelling $\dot{b}$ is the main point of interest of a large group of glaciologists (Gallée et al., 2011; Lenaerts et al., 2012; Favier et al., 2013; Frezzotti et al., 2013). In our simplified models we use explicit formulation of accumulation and ablation, as functions of the surface temperature:

$$\mathrm{Acc} = \mathrm{Acc}_0 e^{-c_1 T_s} \tag{1.17}$$

$$\mathrm{Abl} = \begin{cases} \mathrm{Abl}_0 \left(\dfrac{T_s - T_{\text{no melt}}}{T_{\text{no melt}}} \right)^2 & \text{if } T_s > T_{\text{no melt}} \\ 0 & \text{otherwise} \end{cases} \tag{1.18}$$

where the parameters are given by the gaciologists expertise. The surface temperature T_s depends on the surface elevation S, the latitude x and the climate scenario F_{clim} (temperature in $x = 0$, $S = 0$), according to the formula:

$$T_s(x, y, t) = F_{\text{clim}} + \lambda\, x + \gamma\, S(x, y, t) \tag{1.19}$$

where λ and γ are given parameters.

1.2.2 Introduction to inverse modelling in glaciology

Model initialization for the sea level problem

The contribution of glaciers and ice caps to sea level change is significant and crucial to make good predictions for the future (Hanna et al., 2013). It is essentially a combination of two factors: the change in surface mass balance (due to climate change and / or ice cap elevation) on the one hand, and ice discharge by icebergs calving in ice streams and ice-shelves on the other hand. Here we do not consider the contribution due to changes in the surface mass balance. Indeed, these changes are intrinsically linked to climate change, are also very complex and subject to active research[3].

The mass loss of polar caps by iceberg calving is controlled by a small number of ice streams. For example 10% of the periphery of Antarctica is estimated to control 90% of the ice discharge. The presence or absence of ice streams is closely linked to the nature of the basal conditions that allow or not a strong sliding and thus high flow velocities. Another key parameter is the geometry of the bedrock (elevation and slope), especially in coastal

[3]See the fifth report of the IPCC (2013-14): `http://www.ipcc.ch`

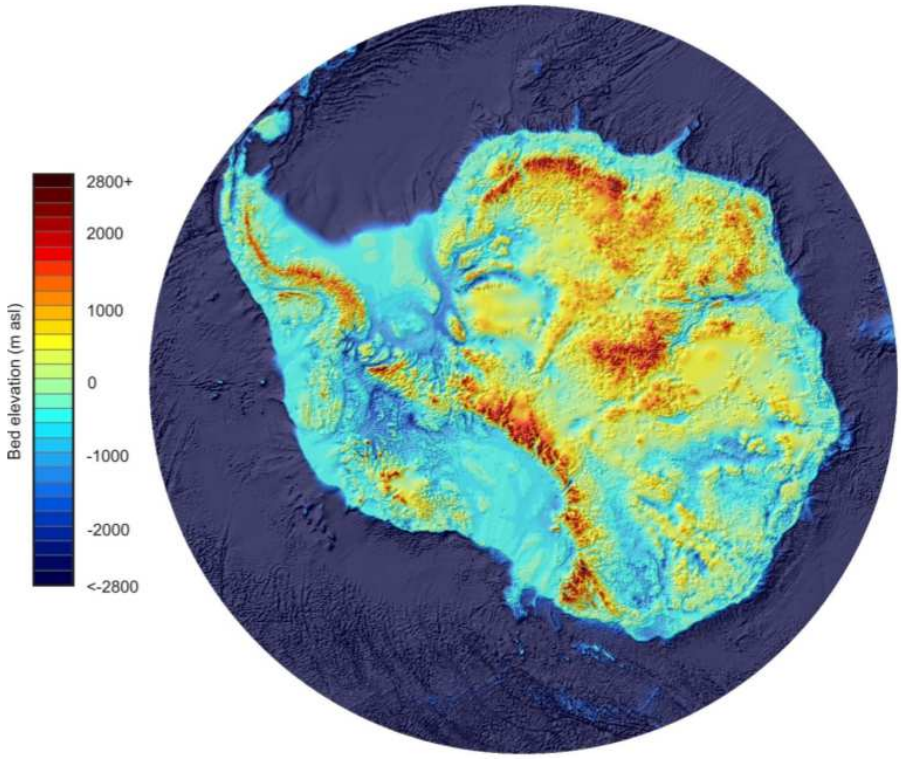

Figure 1.4: Bedrock topography observation map Bedmap2 of the Antarctica, from Fretwell et al. (2013). Measures are performed by aircrafts flying above the continent. The highest point reaches more than 4500 meters. Because of the ice weight and isostasy, whole areas are situated around 1000m under sea-level.

areas. Indeed the deformation velocity depends on both the surface elevation $S(t,x)$ and the ice thickness $H(t,x)$, and therefore on the elevation of the base $B(t,x) = S - H$. Moreover, the depth of the base also influences the ice thickness (for a given surface elevation), and therefore the pressure conditions at the base of ice, which in turn affect the presence or absence of liquid water.

The problem of model initialization consists essentially in obtaining a good geometry of the ice-sheet and good basal conditions, in order to correctly initialize the evolution models. This is an inverse problem, where we wish to estimate these sensitive parameters thanks to available observations (see below).

Identification of basal conditions. On a more local scale (glacier or watershed), glaciologists generally have a more precise knowledge of the geometry, through regional measurement campaigns. In this case, the local study is essentially to identify the sliding/friction conditions at the base. It can be done either by identifying the coefficient β of our equations, or by seeking to identify more complex friction laws, as $\boldsymbol{\tau}_b = -\beta \|\boldsymbol{U}_{\text{slid}}\|^{\alpha} \boldsymbol{U}_{\text{slid}}$, or also by studying subglacial hydrology more precisely, see e.g. de Fleurian (2010) and references therein, and in paragraph 1.2.3 the summary of paper [6].

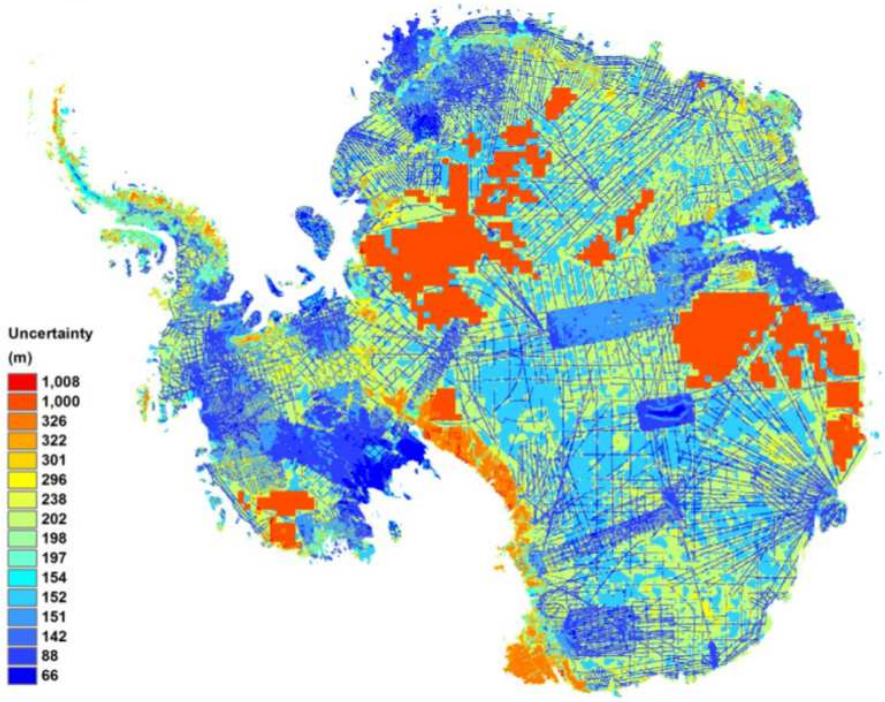

Figure 1.5: Estimated errors for the Antarctica's bedrock topographies, from Fretwell et al. (2013). The maximal uncertainty reaches 1000 meters in unobserved areas, and is around 20 meters on measure points (flight tracks).

Observations of ice caps and glaciers

As noted above, the conditions at the base of the ice are related to the depth and nature of the bedrock and the hydrological and thermal conditions.

Observations for the friction conditions at the base are very limited. In fact it is almost impossible to do measurements under the ice, except in rare points of deep drilling where the base has been reached. In these cases, the analysis of ice cores provides information on these basal conditions. Laboratory experiments are poorly representative, as it is impossible to restore the pressure equivalent to thousands of meters of ice thickness. Another critical uncertainty is the nature of the base: is it of sediment, rock, rock debris? The presence of liquid water, crucial for sliding, is also linked to poorly known parameters such as heat flux. So we do not have reliable measures for the friction law and associated coefficients.

Regarding the elevation of the base, we have a limited number of measurements made by aircrafts[4]. The observations are thus restricted to aircraft tracks. In measurement points, the accuracy is about twenty meters. Outside measuring points, interpolation strategies are used, but the uncertainty in unobserved areas can be up to several hundred meters. Moreover, the maps are obtained by kriging, regardless of the ice flow. Figures 1.4 and 1.5 show the state of the art of such maps for Antarctica (Fretwell et al., 2013):

[4]Satellite measurements are possible, but unfortunately the radar frequencies required to observe the bedrock beneath the ice are military restricted. For the same reason, the aircraft campaigns are expensive and complex to implement.

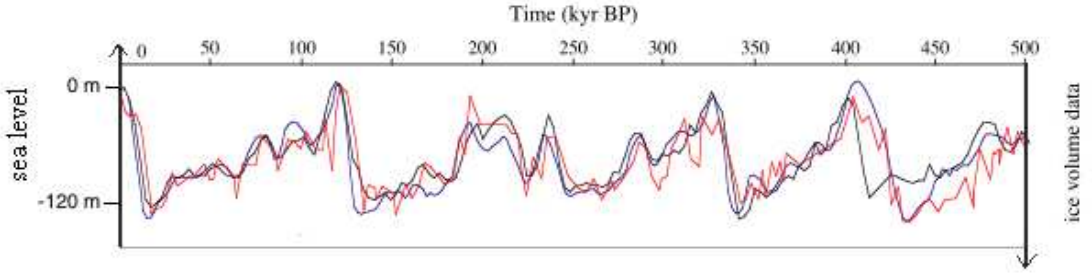

Figure 1.6: Ice volume observations. In black: measures from Raymo (1997). In grey: results obtained from varioux models. Figure from Paillard and Parrenin (2004).

the first is a bedrock elevation map, the second represent the associated estimated errors. We can clearly see on this second map the aircraft tracks, where accuracy is good, and the unobserved areas, with large potential errors. It should be noted here that the relief of the Antarctica is very bumpy, and quite similar to the Alps, with abrupt changes in elevation and mountain ranges.

The other observations that we have, and from which we extract information to find the unobserved parameters are remote-sensing surface data: surface elevation, ice surface velocity. The surface elevation has been observed since the last twenty years by satellite (ERS-1, Envisat radar, ICESat laser). The accuracy is relatively good, usually about 2 meters, except in mountainous areas where the RMS error can rise to 130 meters (Griggs and Bamber, 2009). For the surface velocity we also have good coverage, spatial resolution is of the order of kilometers, as is the surface elevation. Errors for velocity are of the order of 1 to 17 meters per year (Rignot et al., 2011; Joughin et al., 2010).

Paleoclimatology

Several inverse questions arise for paleoclimatology (study of past climates). Best known is the dating of ice cores, for which recent advances using inverse methods were obtained by Lemieux-Dudon et al. (2008, 2010); Buiron et al. (2011). Another issue that has interested us is related to a very specific kind of observations: total volume of the polar ice caps. Indeed, this volume is directly related to sea level, which could be measured on huge time scales (hundreds of thousands of years), thanks to biostratigraphic markers such as foraminifera (Paillard and Parrenin, 2004). Figure 1.6 presents such data. The question states as follows: considering that the surface temperature directly influences the evolution of the ice-sheet and thus its volume, can a climate scenario be estimated from of ice volume measurements? With the simplified model presented above, this amounts to find the F_{clim} parameter. We studied such a problem in [17], and we will summarise the results later on.

State of the art of inverse methods in glaciology

Data assimilation, primarily by control method, is more recent in glaciology than it is in meteorology or oceanography. MacAyeal (1992, 1993) introduced control methods to identify the friction coefficient β at the base of an ice stream (equation SSA only), using the

self-adjoint property of the equation. Several applications in various ice-streams followed, for example, Rommelaere and MacAyeal (1997); Vieli and Payne (2003). More recently, the adjoint method (always called control method by glaciologists) was also implemented in an approximate way for a full-Stokes model by Morlighem et al. (2010), using as an adjoint the model itself. This is an approximation, because the full-Stokes equations of the model are not self-adjoint unless the viscosity is linear (law Glen with $n = 1$). Heimbach and Bugnion (2009) used an automatic differentiation tool to generate the full adjoint code SICOPOLIS (Greve, 1997) to do sensitivity analyses.

Other inverse methods have recently been introduced. BLUE method and optimal interpolation (OI) have been used by Arthern and Hindmarsh (2003) and Berliner et al. (2008). A method due to Chaabane and Jaoua (1999) was also used by Arthern and Gudmundsson (2010). It is called Robin method and it consists in minimizing a cost function measuring the misfit to observations by a gradient descent on the coefficient β. This is done by successive iterations of Full-Stokes model resolutions with either a Dirichlet condition at the surface (by imposing the observed velocities), or a homogeneous Neumann condition (the natural condition of the model). At convergence, the solution satisfies both the Dirichlet and the Neumann condition and produce the desired β field.

Most of these articles focus on the basal friction β identification, but only for local problems at the scale of a glacier, an ice stream or a watershed. The reconstruction of β for all Greenland is very recent: see Arthern and Hindmarsh (2006) with a BLUE / OI type method, and [8] with a control method and Robin. More recently, glaciologists studied joint reconstruction of both the friction β and the base B_{soc}, see Raymond-Pralong and Gudmundsson (2011) (with a Bayes method which is actually the direct minimization of the BLUE with an approximate gradient) and van Pelt et al. (2013) (single Picard iteration to reduce the observation misfit). This question is more difficult because it seems that uniqueness is not guaranteed: the same surface velocity can be explained either by a low B_{soc} (large deformation velocity) and no sliding or a higher base with more sliding.

As for inverse methods for paleoclimatology, the question of climate reconstruction thanks to ice volume observations is addressed by Bintanja et al. (2004, 2005) using a simple correction method, similar to nudging (Newtonian relaxation). For the problem of ice core dating, state-of-the-art inverse methods have been developed, see e.g. Lemieux-Dudon et al. (2008, 2010).

In the following paragraphs we summarise the works we did in glaciology.

1.2.3 Study of the basal conditions of Variegated glacier

This paragraph summarises the results contained in [6], about the surge[5] of Variegated glacier in 1982–83.

Introduction

The Variegated Glacier in Alaska is known to surge regularly. The first recorded surge took place in 1905-1906, and there were seven others until the last in 2003-04. The study presented in this paper focuses on the surge of 1982-1983 because it has been well

[5] *Glacial surges* are short-lived events where a glacier can advance substantially, moving at velocities up to 100 times faster than normal.

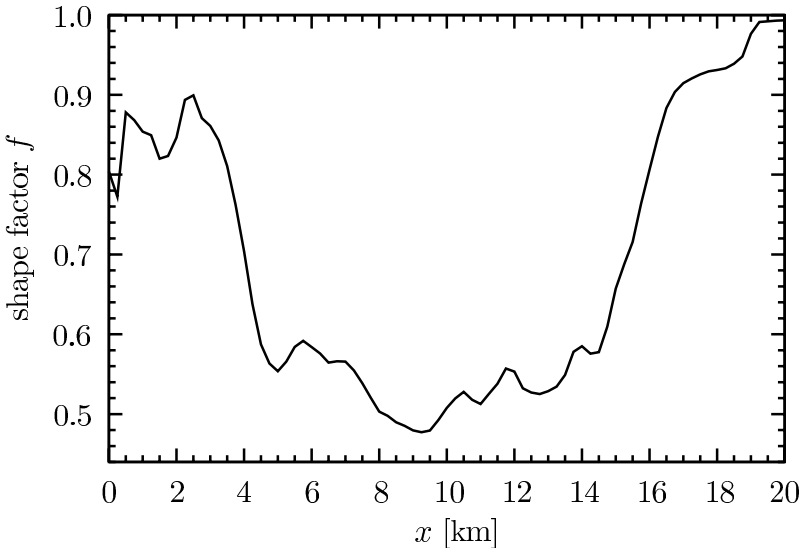

Figure 1.7: Evolution of the shape factor $f(x)$ along the central flowline of Variegated glacier for the surface topography $z_s(x)$ of 1973.

observed. According to Raymond (1987) we know that surges for temperate[6] glaciers are due to changes in the subglacial hydrological system, going from an effective system to an ineffective one. An effective system corresponds to a good drainage of the water under the ice, with large channels, causing low water pressure under the glacier. On the contrary, an inefficient system does not have these wide channels but small connected cavities, resulting in an increase in subglacial pressure and changes in sliding conditions. The passage of an effective system to an inefficient system (by opening and closing of the wide channels) is governed by changes in geometry (surface elevation and slope) and temperature (the seasonal alternation, which influences melting). Kamb et al. (1985) made measurements of strain rate in a drillhole during the surge and showed that 95% of the glacier velocities are explained by sliding the base. This paper therefore focuses on the identification of basal conditions throughout the glacier before and during the surge to try and confirm this hypothesis.

Observations and model

The surface elevation and surface velocities were measured during the decade 1973–1983 (Bindschadler et al., 1977; Kamb et al., 1985; Raymond and Harrison, 1988), which covers part of the quiescent phase and the surge. There are data twice a year before the surge and eight times during the two years of the surge. In space, the data were collected every 250 meters along the 20 kilometers of the center line of the glacier, with some gaps (in particular due to the presence of cracks).

As measurements are available only on a flow line, we used a 2D model (x, z). The glacier base $b(x)$ is fixed, and the surface elevation is denoted by $z_s(x)$, where x is the horizontal direction, with $x = 0$ at the top of the glacier (at an elevation of about 2000 meters) and $x = 20$ kilometers at the front, where the glacier ends in the sea. The

[6]The ice of a *temperate* glacier is near to melting point.

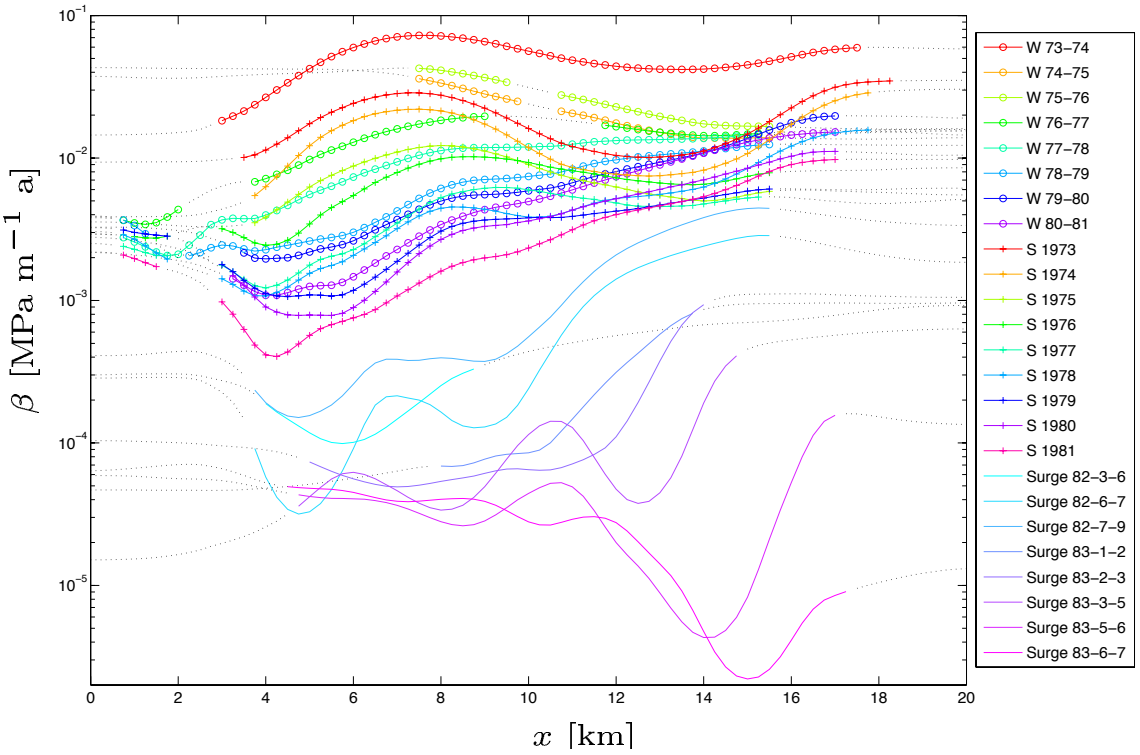

Figure 1.8: Distribution of the basal friction coefficient β given by the Robin inverse method along the central flowline, for the 25 observing dates. Dotted curves indicate where measured surface velocities are missing. In the legend, W Y1-Y2 represents winters between year Y1 and year Y2 ; S Y summer of year Y ; Surge Y-M1-M2 for year Y from month M1 to month M2.

chosen model solves the full-Stokes equations presented above, but in 2D and not 3D. In particular, the equation of conservation of momentum (1.2) then reads:

$$\text{div}\ \boldsymbol{\sigma} + \rho_i \boldsymbol{g} + \boldsymbol{f}_1 = 0, \ \text{ for } x \in [0, 20], z \in [b(x), z_s(x)]$$

where $\boldsymbol{f}_1$ is a parameterisation of lateral effects:

$$\boldsymbol{f}_1 = \rho_i \boldsymbol{g}.\boldsymbol{t}\,(1 - f)\,\boldsymbol{t}$$

where $\boldsymbol{t}$ is the unitary tangent vector and f is the shape factor. If $f = 1$ then $\boldsymbol{f}_1 = 0$, leading to an infinitely wide glacier. On the contrary, a small f modellised narrow sections. The formula for f is:

$$f(x) = \frac{2}{\pi} \arctan\left(\frac{0.8146}{\sqrt{a(x)(z_s(x) - b(x))}}\right)$$

where $a(x)$ represente the local shape of the bedrock, see [6] for more details, and figure 1.7 for the corresponding $f(x)$ function.

Surface and basal boundary conditions are the same as before (1.5,1.6,1.7), in particular the basal drag law (1.7) features the β coefficient we want to identify with DA.

Numerical resolution is conducted using the finite elements model Elmer/Ice (Gagliardini et al., 2007; Gagliardini and Zwinger, 2008; Gagliardini et al., 2013).

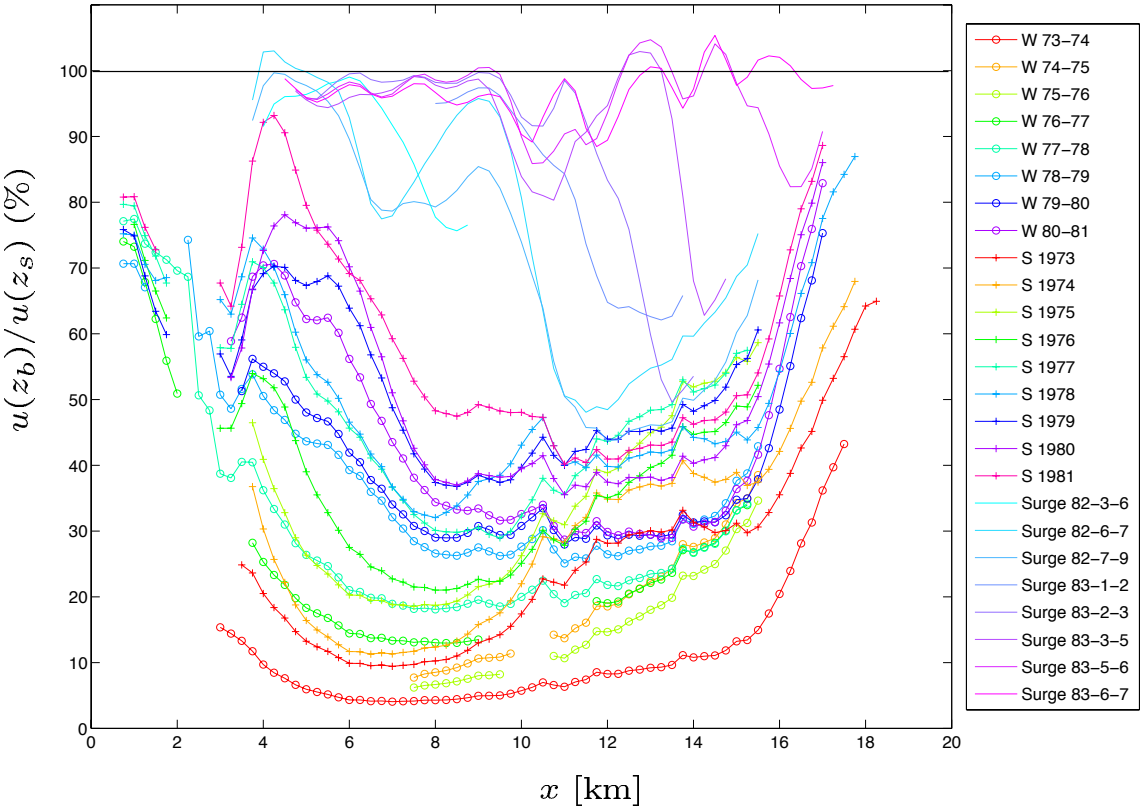

Figure 1.9: Distribution of the ratio of the modelled horizontal basal velocity $u(z_b)$ over the surface velocity $u(z_s)$ along the central flow line for the 25 dates of measurements. Results are shown only where velocity have been measured. Legend is similar to figure 1.8.

Inverse method

The issue of recovering basal conditions from surface observations has been well studied in glaciology, see section 1.2.2 for a brief review. In this article, we used the Robin method of Chaabane and Jaoua (1999); Arthern and Gudmundsson (2010), which was slightly modified to introduce Tikhonov regularization. As mentioned above, the principle of the Robin method is to solve alternately the Full-Stokes equations first with the Dirichlet conditions:

$$u(z_s) = u^{\text{obs}}$$

then with the Neumann condition (1.6). The cost function, which measures the difference between the solution of the Dirichlet problem $\boldsymbol{u}^D$ and of the Neumann problem $\boldsymbol{u}^N$, is defined as follows:

$$\mathcal{J}_o = \int_{\Gamma_s} (\boldsymbol{u}^N - \boldsymbol{u}^D).(\boldsymbol{\sigma}^N - \boldsymbol{\sigma}^D).\boldsymbol{n}\, d\Gamma$$

where Γ_s represents the surface boundary of the glacier.

One can easily calculate the directional derivative of $\mathcal{J}_o$ from β (in the direction β') to

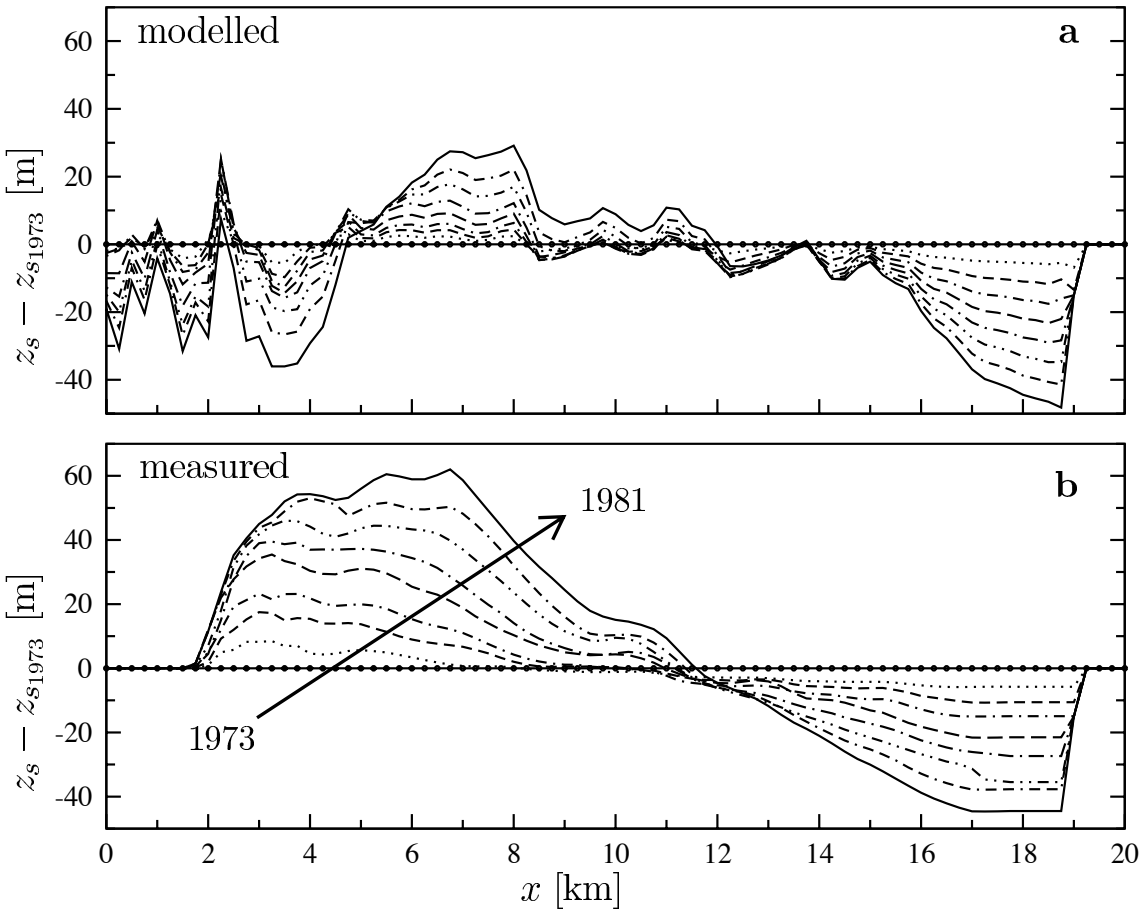

Figure 1.10: Comparison of modelled and measured surface geometry for each dates during the quiescent phase.(a) Relative modelled surface topography to 1973.(b) Relative observed and reconstructed surface topography to 1973 used to diagnostic basal conditions.

implement a descent method:

$$d_\beta \mathcal{J}_o(\beta') = \int_{\Gamma_b} \beta' \left(|\boldsymbol{u}^D|^2 - |\boldsymbol{u}^N|^2 \right) \, d\Gamma$$

where Γ_b is the basal boundary. It is important to note here that this derivative is accurate only in the case of a linear rheology (ie law Glen with $n = 1$). In the realistic case $n = 3$, the derivative is only an approximation.

As β is positive and varies by several orders of magnitude, it makes more sense to change the variable β into α by setting:

$$\beta = 10^\alpha$$

Finally, the problem is regularized by adding a regularization term :

$$\mathcal{J}_{\text{tot}}(\alpha) = \mathcal{J}_o(\alpha) + \frac{1}{2} \lambda \, \overline{u}_{\text{obs}} \, \mathcal{J}_{\text{reg}}(\alpha), \quad \mathcal{J}_{\text{reg}}(\alpha) = \int_{\Gamma_b} (\partial_x \alpha)^2 \, d\Gamma$$

The term $\overline{u}_{\text{obs}}$ is the average surface velocities observed for the considered dataset. It is a normalization factor between the different years of observation. Indeed, we observe

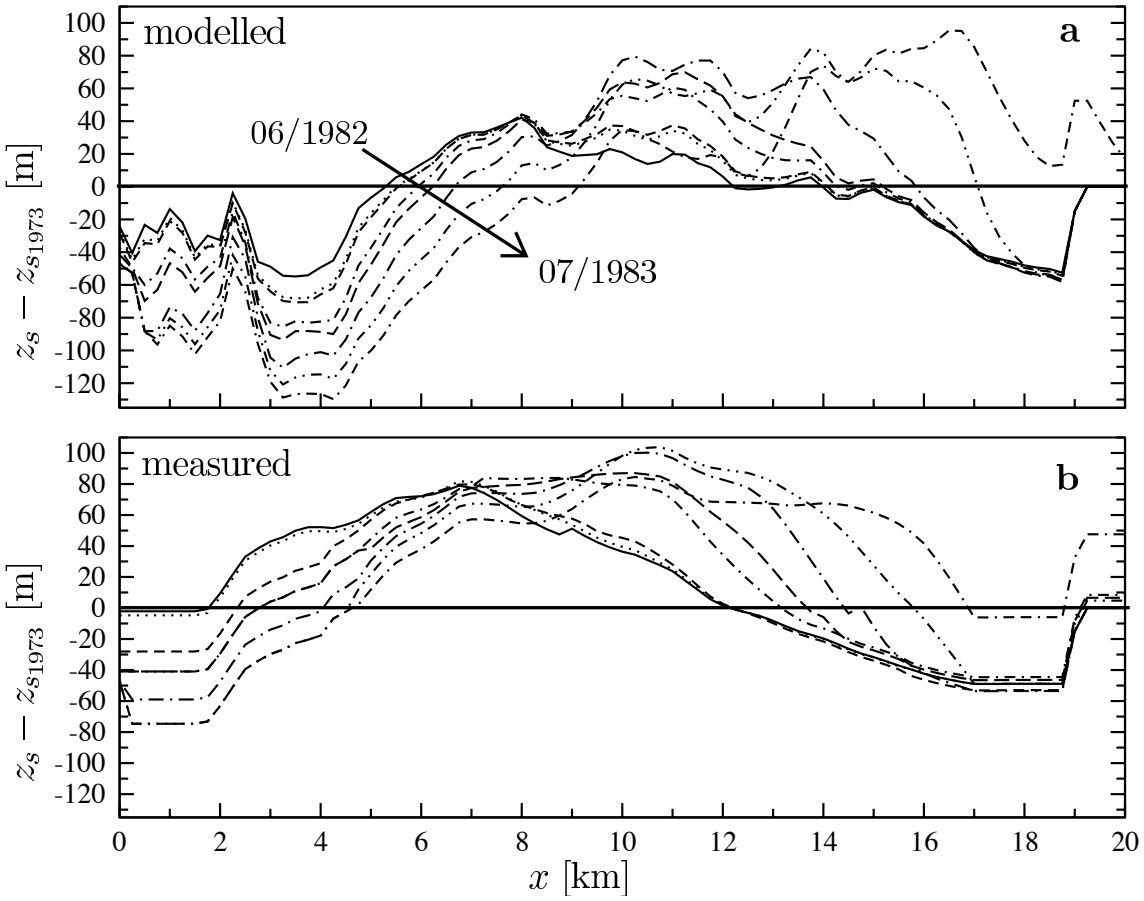

Figure 1.11: Comparison of modelled and measured surface geometry for each dates during the surge.(a) Relative modelled surface topography to 1973.(b) Relative observed and reconstructed surface topography to 1973 used to diagnostic basal conditions.

large variations in $\overline{u}_{\text{obs}}$ over the years. Its addition allows to choose a weight between observation and regularization which is independent of the data set.

Technical aspects, such as the choice of the parameter λ, are described in the article.

It should be noted that this Robin method applies to the velocity equation only, and not to the coupling with the free surface evolution: at each time step we implement the inverse method. Thus, when there is no observation at a certain time, there is no estimate of β.

Results

The model and the method are implemented in the finite element code Elmer/Ice (parallel, Fortran 95) (Gagliardini et al., 2013).

The results are described in detail in the article, here we quickly show the main figures. Figure 1.8 shows the beta coefficient β obtained by assimilation. We see, in addition to seasonal alternation winter / summer, that β decreases gradually over the years during the quiescent phase and is very low during the surge. In addition, we see that during the quiescent phase, β decreases more strongly in the upper part of the glacier (x close to

0). We also see very clearly the regime change associated to the surge, and the gradual decrease of β from the top to the bottom of the glacier.

Figure 1.9 shows the ratio between the basal velocity $u(z_b)$ and the surface velocity $u(z_s)$. We also see a gradual change in this ratio, from 10% in 1973 to 60% in the summer of 81, even 90% in 1981 at the top of the glacier. This suggests that the acceleration occurs from a gradual increase in sliding (and not a sudden outbreak), and that the sliding explains a large part of the acceleration of the glacier during the surge, but also during the quiescent phase. In this figure we also clearly identify two regimes: surge / quiescent, with ratios close to 100 % for the surge, and the increase of this ratio from the top of the glacier to the bottom.

The paragraph §6 of the paper presents results to which I have not contributed, offering a more complex sliding law, to take into account the pressure of subglacial water, I will not go into details here.

Figures 1.10 and 1.11 present direct simulations with the identified parameters β during the quiescent phase and during the surge, compared to observations. To do this, we run the direct model with β and we solve the following evolution equation for the free surface:

$$\partial_t z_s + u_x \partial_x z_s - u_z = a_s$$

where a_s is the surface mass balance, modeled by an explicit function depending linearly on z_s. The differences between the observations and the model can be explained by errors in the mass balance and/or by the three-dimensional effects that have been neglected. Despite this, we get to highlight correctly the following points:

- the surge is consistent with observations, in other words the field β allows to generate the glacier surge;
- the model can represent the typical characteristic of glacier thinning at the top and thickening at the bottom.

In conclusion, the ability of the model to account for many of the key features of the surge offers a posteriori validation of the reconstruction of the coefficient β with the method of Chaabane and Jaoua (1999); Arthern and Gudmundsson (2010). This paper proposed the first application of this method to a real case, and demonstrates its feasibility and relevance to study basal friction.

1.2.4 Contribution of Groenland to sea level rise

This paragraph summarise the paper [8], in which we study the impact of Greenland on sea level change.

Introduction

Greenland is losing mass at an increasing rate (Rignot et al., 2011). It seems that this is due to the combination of two factors: the change in surface mass balance (more melt and / or less precipitation) and the increase of ice discharge (iceberg calving). Previous studies (Howat et al., 2007; Pritchard et al., 2009; Joughin et al., 2010) showed that the acceleration of calving was highly variable in time and space, so that realistic predictions must necessarily use both a high precision model, an accurate initial state and reliable climate projections. The problem of initializing a small-scale model for Greenland is

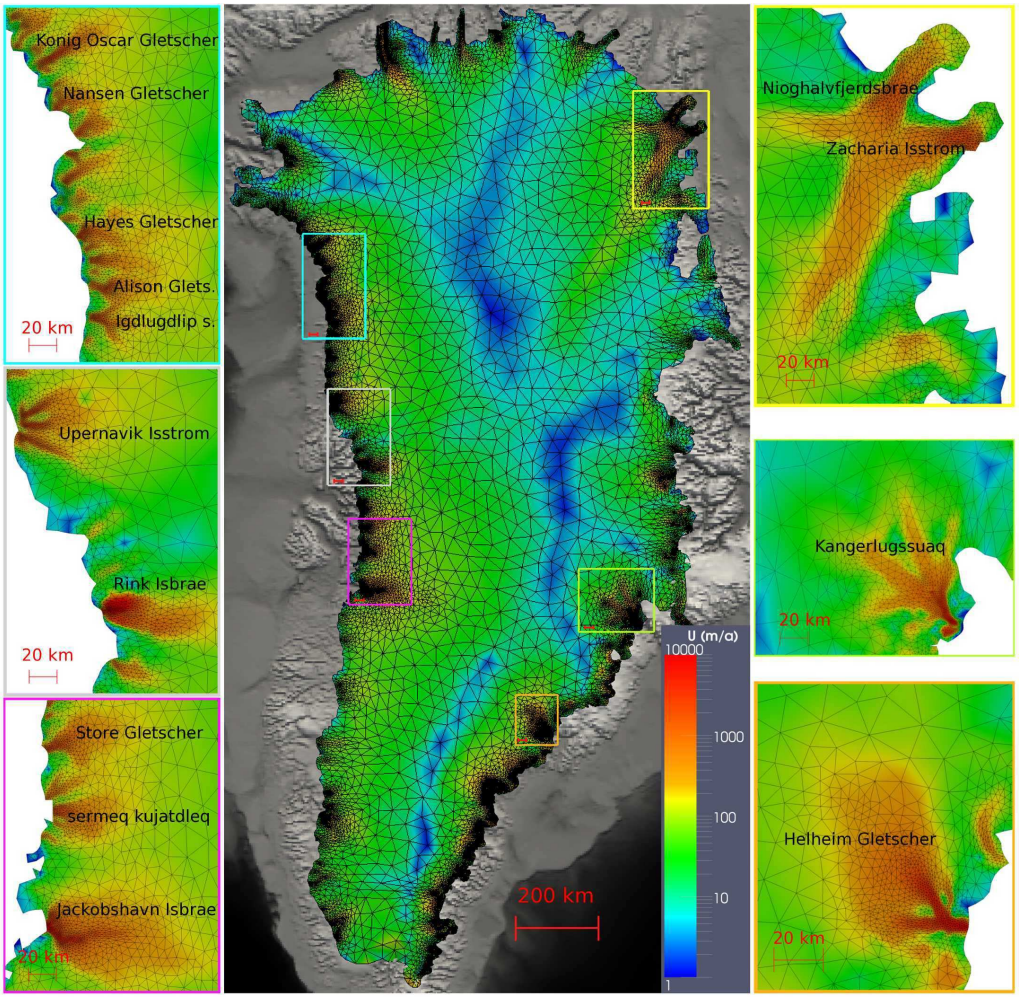

Figure 1.12: Unstructured finite element mesh and model surface velocities after optimisation of the basal friction coefficient β with the Robin inverse method. Colored boxes show close-up views for various outlet glaciers of interest.

the motivation of this article. The basic ingredients are: a Full-Stokes model on an unstructured grid and inverse methods to make the most of the available observations. This article is the first attempt to use all these elements across Greenland. More specifically, the objective is to identify the field of basal friction $\beta(x, y)$ in a full-Stokes model from available observations in order to produce forecasts of Greenland's dynamics.

Model and data

The model solves the nonlinear 3D full-Stokes equations (Glen's law with $n = 3$) (1.1) to (1.8) described on page 26. The coefficient $\mathcal{B}_{AT,n}$ in equation (1.3) actually depends on the temperature in the ice (according to an Arrhenius law, see details in the article). The temperature field in the ice is given by the SIA model SICOPOLIS (Greve, 1997; Seddik et al., 2012), constant in time.

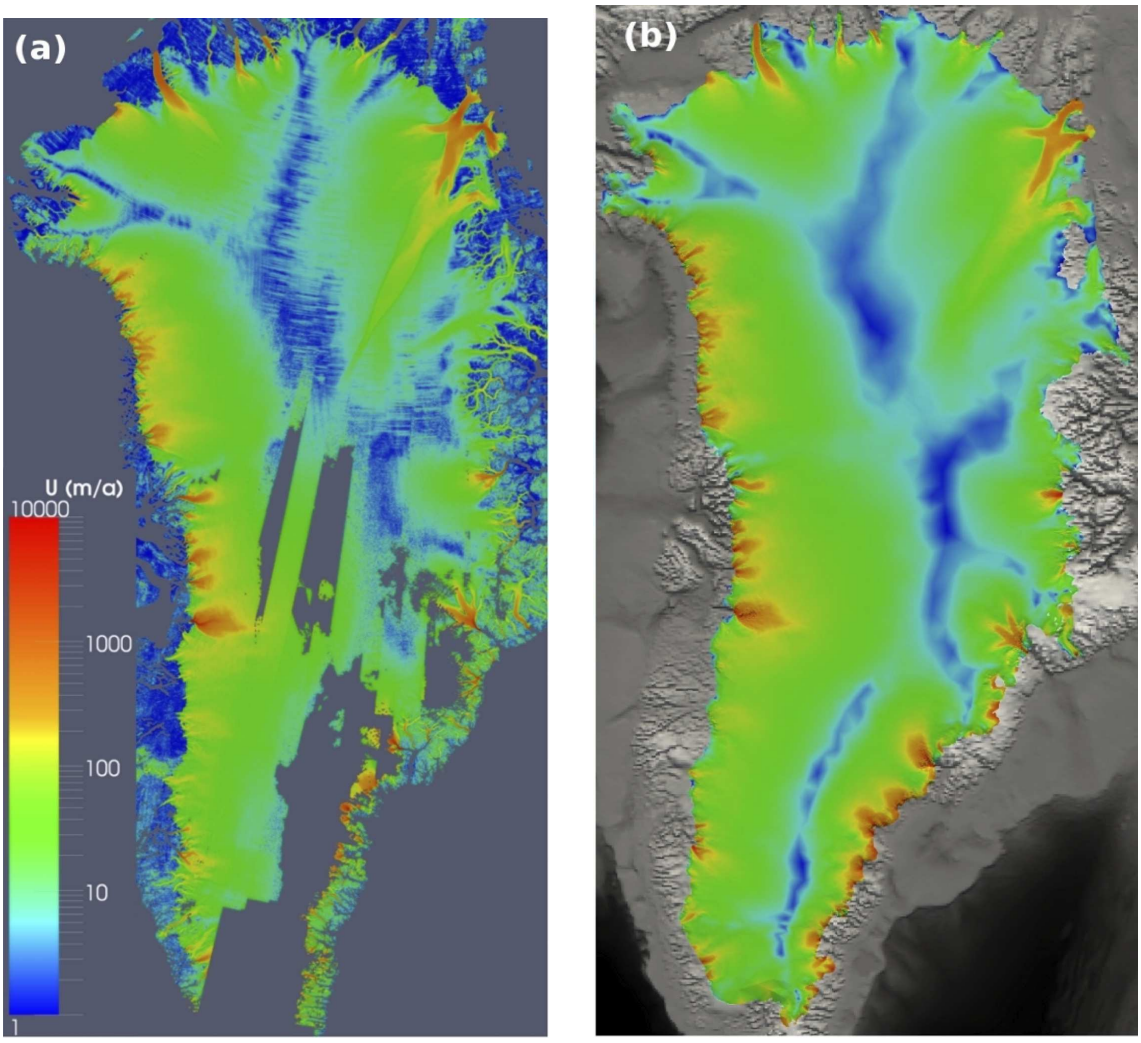

Figure 1.13: Greenland surface velocities, on the left (a) observed velocities; on the right (b) velocities after reconstruction of β with the Robin method.

The numerical code Elmer/Ice[7] Gagliardini et al. (2013) solves these equations over the entire Greenland with an unstructured mesh. The construction of the initial mesh uses classical ingredients: error estimates with the Hessian matrix of the observed velocities and adaptive mesh with YAMS software (Frey and Alauzet, 2005). During the simulation, to some extent, this mesh is adaptive, but nodes can only move vertically. An example of the mesh is shown in Figure 1.12. We refer to Gagliardini and Zwinger (2008) for details of the numerical model.

The bedrock and the surface topography come from SeaRise[8] data (Bamber et al., 2001). The observed velocities are from Joughin et al. (2010), they are shown in Figure 1.13 (a). We also have the rate of change for surface elevation (Pritchard et al., 2009). Note here that the observed velocities are produced from distributed data over the decade 2000–2009, while the surface topography was produced in 2001 (although it was updated

[7] `http://elmerice.elmerfem.org`
[8] `http://tinyurl.com/srise-umt`

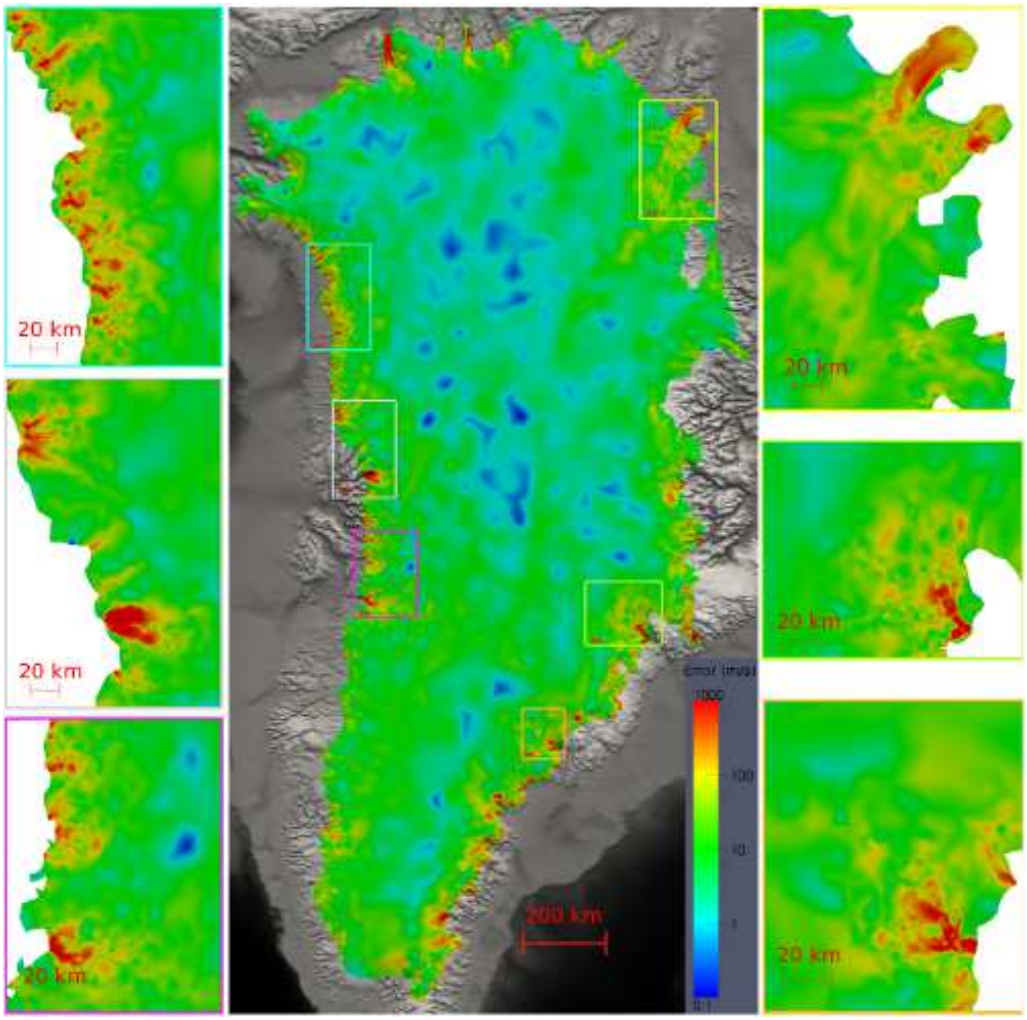

Figure 1.14: Absolute error on surface velocities $|\boldsymbol{u}^{\text{mod}} - \boldsymbol{u}^{\text{obs}}|$ in $\text{m}\,\text{y}^{-1}$ at the end of the optimisation using the Robin inverse method.

for the three major outlet glaciers).

Methods

Recall that the objective is to identify the basal friction $\beta(x, y)$. In this paper we use and compare two methods: the Robin and the control method (with the self-adjoint assumption), introduced for the Full-Stokes model by Morlighem et al. (2010).

Robin method has already been presented in section 1.2.3. The control method consist in minimizing the following cost function:

$$\mathcal{J}_o = \int_{\Gamma_s} \frac{1}{2} \left(|\boldsymbol{u}_H| - |\boldsymbol{u}_H^{\text{obs}}| \right)^2 d\Gamma$$

where $\boldsymbol{u}^{\text{obs}}$ are the observed velocities and H represents the horizontal component of the

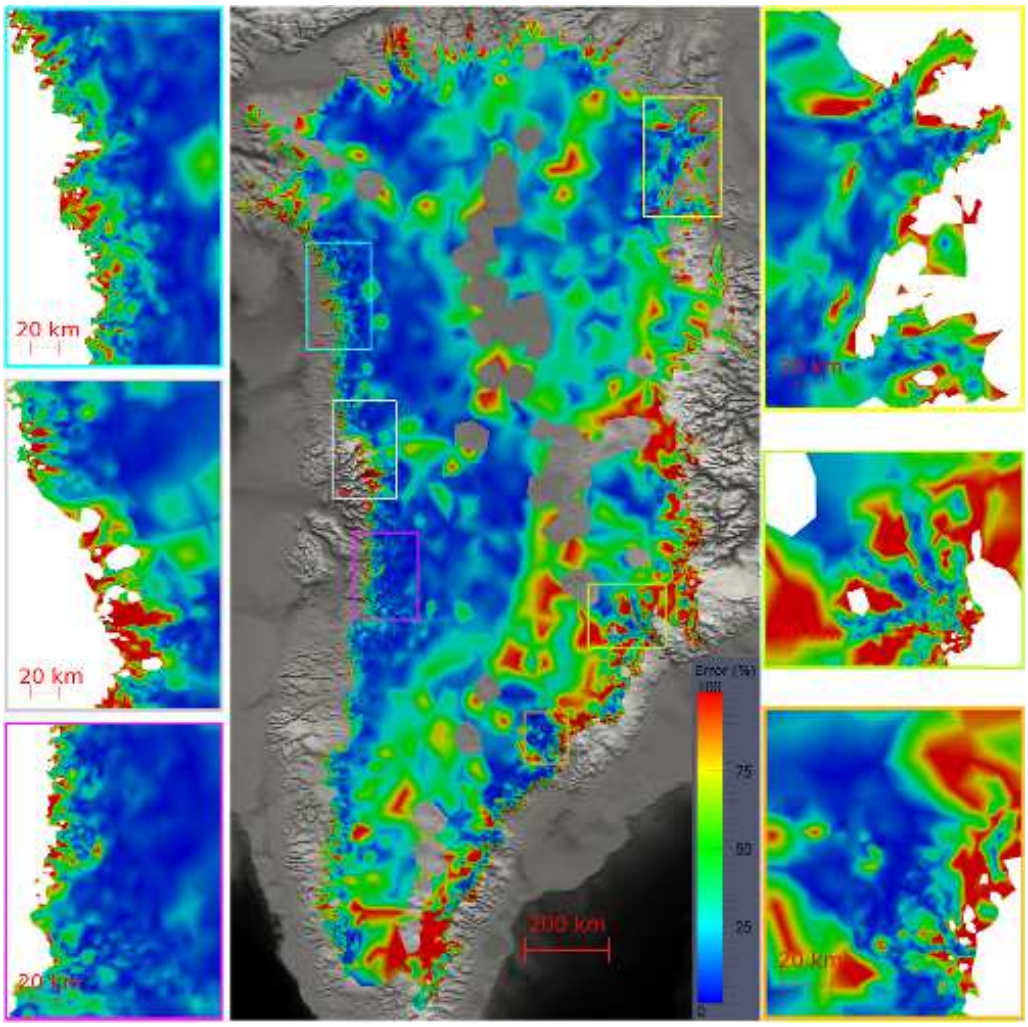

Figure 1.15: Relative error on surface velocities $|\boldsymbol{u}^{\text{mod}} - \boldsymbol{u}^{\text{obs}}|/|\boldsymbol{u}^{\text{obs}}|$ in % at the end of the optimisation using the Robin inverse method. Areas where $|\boldsymbol{u}^{\text{obs}}| < 2.5\,\text{m}\,\text{a}^{-1}$ have been removed from display.

velocity. The derivative of the velocity is given by

$$d_\beta \mathcal{J}_o(\beta') = \int_{\Gamma_b} -\beta' \boldsymbol{u}.\boldsymbol{\lambda}\, d\Gamma$$

where $\boldsymbol{\lambda}$ is the solution of the adjoint equations.

As previously we can note that these methods have two drawbacks:

1. the derivatives of the cost functions are accurate for linear rheology only ($n = 1$), and therefore are approximate in the realistic case here, where the viscosity follows the Glen's law with $n = 3$;

2. moreover, they fail to assimilate time series data, since both work on the diagnostic part of the model only (equation for velocities) and not on the evolution equation of the free surface.

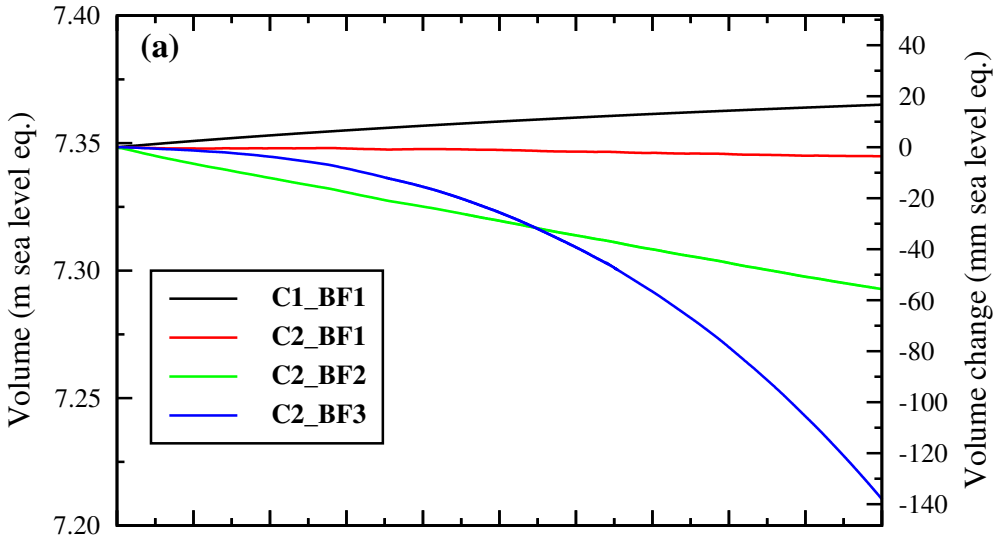

Figure 1.16: Future level changes for the climatic scenarios C1 (today's conditions), C2 (IPCC A1B) and the basal friction scenarios BF1 (constant), BF2 (half BF1), BF3 (decreasing of 1 order of magnitude after 100 years).

However, these methods have the advantage of being easily implementable and fairly inexpensive. Conversely, to implement the adjoint model is complex in practice. Indeed, the non-linearity is processed numerically by Picard iterations and the adjoint of such an algorithm is as expensive as it is delicate (Griewank and Walther, 2008).

These two methods are implemented by changing variable with α such that $\beta = 10^{\alpha}$, and are regularized as before:

$$\mathcal{J}_{\text{tot}}(\alpha) = \mathcal{J}_o(\alpha) + \lambda\,\mathcal{J}_{\text{reg}}(\alpha), \quad \mathcal{J}_{\text{reg}}(\alpha) = \frac{1}{2}\int_{\Gamma_b} (\partial_x \alpha)^2 + (\partial_y \alpha)^2 \, d\Gamma$$

The choice of λ is done with the L-curve method, and the minimization is carried out by quasi-Newton method M1QN3 by Gilbert and Lemaréchal (1989), we refer to the article for details.

Results

The model and the method are implemented into Elmer/Ice finite elements models (parallel, in fortran 95) (Gagliardini et al., 2013).

Surface velocities reconstruction. Figures 1.12 and 1.13 (b) show the velocities obtained after identification of β by the Robin method. The results obtained with the control method are very similar. The main features of the flow are well reproduced: low velocities in the central areas, ice streams individualized and well localized, good rendering of the largest outlet glaciers and their watersheds.

Figures 1.14 and 1.15 present the absolute and relative errors between reconstructed and observed velocities. As for velocities, the errors vary by several orders of magnitude between the interior and the coast. The largest errors lie on the coasts. Several possible explanations to these can be drawn:

1. observations of surface velocities and surface topography do not match, since they are not measured on the same dates;
2. some ice streams, especially in the north, end with long ice-shelves, unresolved by the model;
3. the minimization is carried out with an approximate gradient;
4. $\beta(x, y)$ only is controled, and not the other sources of model uncertainties (bedrock in particular);
5. model resolution is worse than velocities data resolution;
6. ice thickness data resolution is lower than that of the model, especially in the outlet glaciers where a good resolution is crucial.

Sensitivity experiments and projections. The objective of the identification of $\beta(x, y)$ is to initialize the model in order to predict the ice volume evolution on Greenland. This poses several problems and questions:

1. the issue (well known by glaciologists for any inverse method that does not incorporate time series data) of the initialization shock: the free surface has non-physical growth rate, especially around the edges, and the adjustment to realistic rates may take a few decades;
2. which surface mass balance scenario must be chosen (precipitation − melt), in connection with which climate scenario?
3. how is the beta parameter β expected to vary over time?

To address the first point, we begin by relaxing the model, that is to say, let it run freely for 50 years, keeping the surface mass balance constant. This helps to stabilize the ice-cap a little and partially correct velocity and calving in outlet glaciers errors (see paper for details).

Regarding the other points, we choose two scenarios for the surface mass balance (C1: current conditions, C2: A1B[9] of IPCC[10]), and three scenarios for the evolution of β (BF1: constant; BF2: half; BF3: decreasing by 1 order of magnitude over 100 years), and experiments have been run for each of these scenarios. Figure 1.16 shows the evolution of the volume of Greenland (and the equivalent in terms of sea level change), and shows a high sensitivity to basal friction conditions. BF3 scenario corresponds to the simultaneous acceleration of all outlet glaciers, so it is an upper bound for our projections. Combined with climate scenario C2, the projection states 14 cm rise in sea level in 100 years for Greenland. This value is within the limits provided by other work on the subject. The intermediate scenario C2-BF2 also gives results comparable with those available in the literature. We refer to the article for more detailed discussions of these results.

In conclusion, we showed that we could achieve satisfactory results with the approximate data assimilation methods currently available in Glaciology and the realistic model Elmer/Ice (Gagliardini et al., 2013). We saw that there were still many uncertainties,

[9] A1B scenario: stong economic growth, balance between various energy sources, see `http://en.wikipedia.org/wiki/Special_Report_on_Emissions_Scenarios`

[10] IPCC : International Panel on Climate Change.

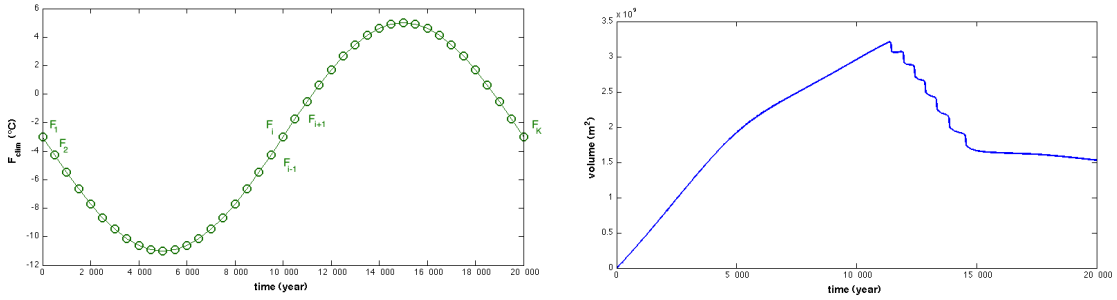

Figure 1.17: Reference state (true) for the twin experiments. On the left, the chosen climatic scenario T_{clim}; on the right the associated ice volume observations Vol^{obs}.

so there is still room for improvement. However, this system can already provide first estimates of the contribution of the dynamics of Greenland to its mass change and sea level rise.

1.2.5 Paleoclimatology: climatic scenario reconstruction

In this paragraph we summarise the problem, model and method contained in the conference proceeding [17]. The results we present here are more advanced, and were presented in various conferences as well.

Problem presentation

The problem studied in this work is the one that was mentioned on page 31: with observations of ice volume over time, how to reconstruct the temperature scenario causing these variations? We study this problem in the simplified framework of twin experiments, that is to say that we generate our own observations from a model. The model chosen is a SIA model (see section 1.2.1 page 27) on a flow line. The choice of the SIA approximation is justified by the time scales: the experiments duration is 20 000 years! The choice of a 2D flowline model is questionable, it would be better in practice to consider multiple flow lines (one for each of the major ice sheets), but we start with a single flowline to study the feasibility of problem.

As mentioned earlier, there are currently few inverse methods used to solve such a problem, a first experiment with the adjoint method is proposed here.

Model and adjoint method

The chosen model is the SIA approximation in 2D (x, z). The above equations are used without the variable y: conservation of mass (1.9), the dynamic equation for $\boldsymbol{U} = \boldsymbol{U}_{\text{def}}$ with $\boldsymbol{U}_{\text{def}}$ given by (1.12) and $\boldsymbol{U}_{\text{slid}}$ null, surface mass balance given by equations (1.16) to (1.19). Numerically, we use the code Winnie developed by LGGE (C. Ritz), which is a prototype of the 3D code GRISLI (Ritz et al., 2001). For this first experiment we chose a flat base $B(t, x) = 0$ and a zero basal mass balance $\dot{f} = 0$. The surface temperature is given by

$$T_S(t, x) = T_{\text{clim}}(t) + b\,x + c\,S(t, x)$$

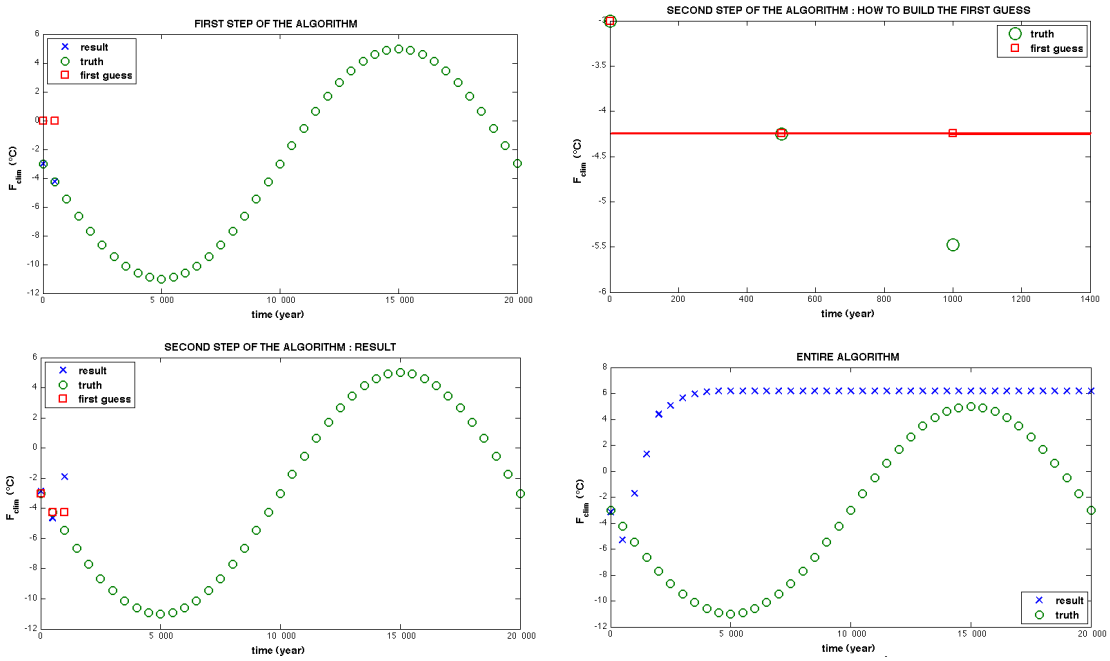

Figure 1.18: Identification of the temperature from volume observations in twin experiments. Increasing window method, background is equal to the previous analysis. Top left: 1st step. Top right: choice of the background for the 2nd step. Bottem left: 2nd step. Bottom right: final result.

and the purpose of the paper is to find $T_{\text{clim}}(t)$ knowing the observations of the ice volume over time:

$$\text{Vol}(t) = \int_x H(t,x)\,dx$$

To do so we choose a reference state, the true state, which ise used to generate observations of ice volume for 20 000 years. Then we form a cost function that measures the distance to the observations, to which is added a regularisation background term.

The cost function is minimized by a Quasi-Newton descent method. The gradient is computed using the adjoint model, which was derived by hand following the recipes by Giering and Kaminski (1998). The adjoint is validated by the gradient tests, which verify that the gradients computed by the adjoint and by finite difference coincide at order 1 and order 2. Specifically, we choose a temperature T^0_{clim}, and a perturbation T, we compute $\mathcal{J}(T^0_{\text{clim}}+\alpha T)-\mathcal{J}(T^0_{\text{clim}})$ for various α with the direct model, then the gradient is calculated with the adjoint model and we check the Taylor formula at order 1 and 2.

Numerical results

We work here with the Matlab version of Winnie.

Numerical experiments have shown a very high sensitivity to the choice of the background and difficulties to obtain algorithm convergence to the desired scenario, we will illustrate this with some tests.

First, we started with the climate scenario shown in Figure 1.17. To start, we chose an oscillating signal with a 20 000 year period ranging from $-11°$C and $5°$C. The choice

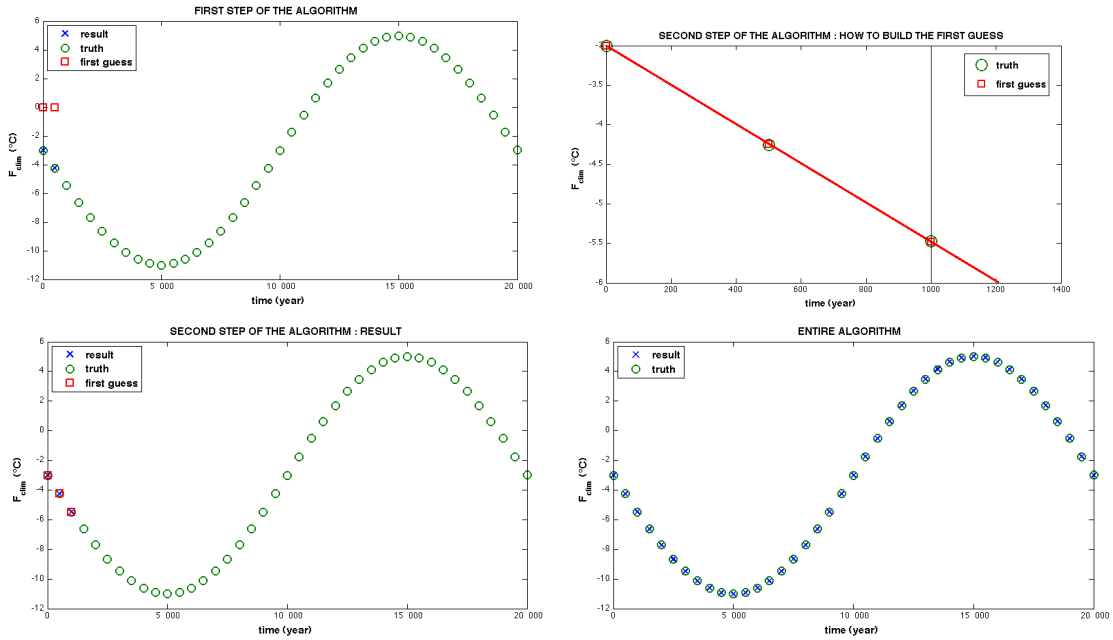

Figure 1.19: Identification of the temperature from volume observations in twin experiments. Increasing window method, background computed by interpolation of the two previous analysis. Top left: 1st step. Top right: choice of the background for the 2nd step. Bottem left: 2nd step. Bottom right: final result.

of the background and the starting point for the minimization was decisive: starting from zero temperature, the algorithm was never able to converge to something approaching the truth. We decided to use an icreasing window, that is to say to make several successive assimilation experiments: one on the interval $[0; 500]$, the second on $[0; 1\,000]$, then $[0; 1\,500]$ and so on to assimilate observations on $[0; 20,000]$. For each new experiment the background is taken as the pevious analysis, and we choose a new estimate for the new point where the background is required.

Figure 1.18 presents the first option we have chosen: after making assimilation on $[0; 500]$ we take $T^b(1\,00) = T^b(500)$. This gives poor results, the algorithm is instantly lost in a local minimum and can not get out.

Figure 1.19 shows another strategy: $T^b(1\,000)$ is calculated by extending the straight line between $T^b(0)$ to $T^b(500)$. This time, the convergence is very good, but it is a little "too easy" because the choice of the background is very close to the true solution, since it is a very regular sine function, well approximated by its tangent.

We therefore conducted another type of experiments, namely assimilating globally (ie directly on $[0; 20,000]$) an actual temperature that is not a sine wave but a perturbation of a sinus, and choosing the background as a perfect sinusoidal function. This gave good results (not shown here). Next, we sought to increase the reference temperature to make it more realistic. We have therefore increased to $[-6°\text{C}; 2°\text{C}]$, and we present the results in Figure 1.20. For higher temperatures, the reconstruction performs very badly. This can be easily explained by the fact that when the temperature is high, in the second part of the period, the ice-cap is loosing mass through melt. The problem here is that any temperature above a certain threshold can explain this deglaciation: therefore there is no

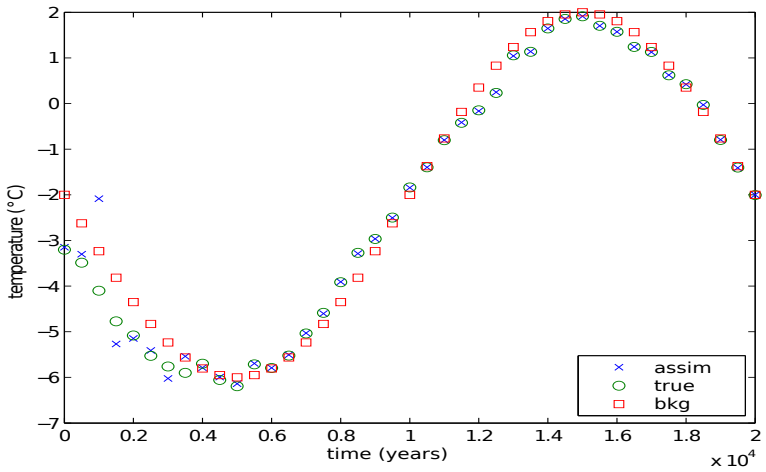

Figure 1.20: Identification of the temperature from volume observations in twin experiments. Global window method. Result for a reference temperature ranging between -6°Cand 2°C.

more uniqueness of the global minimum, thus loss of controllability, which explains our difficulties.

1.2.6 ETKF initialisation of a large scale ice-sheet model

This paragraph summarises the results contained in the submitted paper [22]*, in the framework of B. Bonan PhD thesis, in collaboration with C. Ritz and V. Peyaud from LGGE.*

Presentation

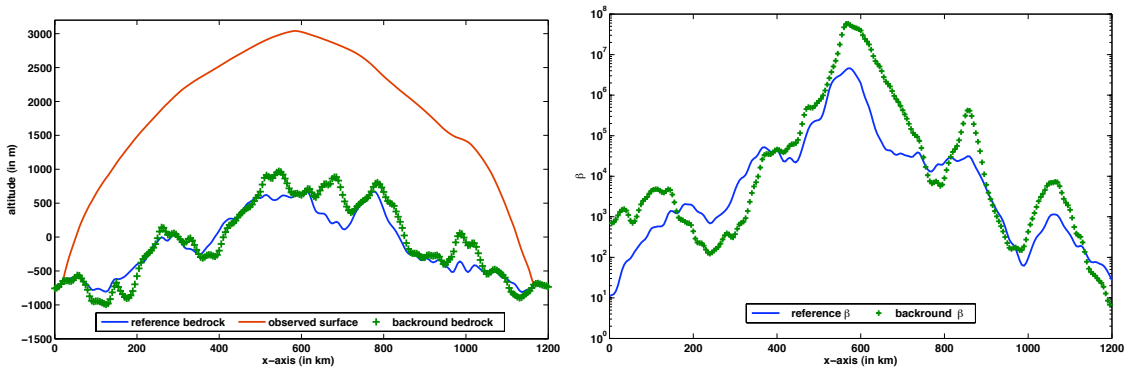

Figure 1.21: Ice sheet geometry (left) and basal sliding parameter $\beta(x)$ (right) for the reference and background states. The x-axis represents the horizontal extent of the ice-sheet (in km). On the left, reference and background surface elevation are identical.

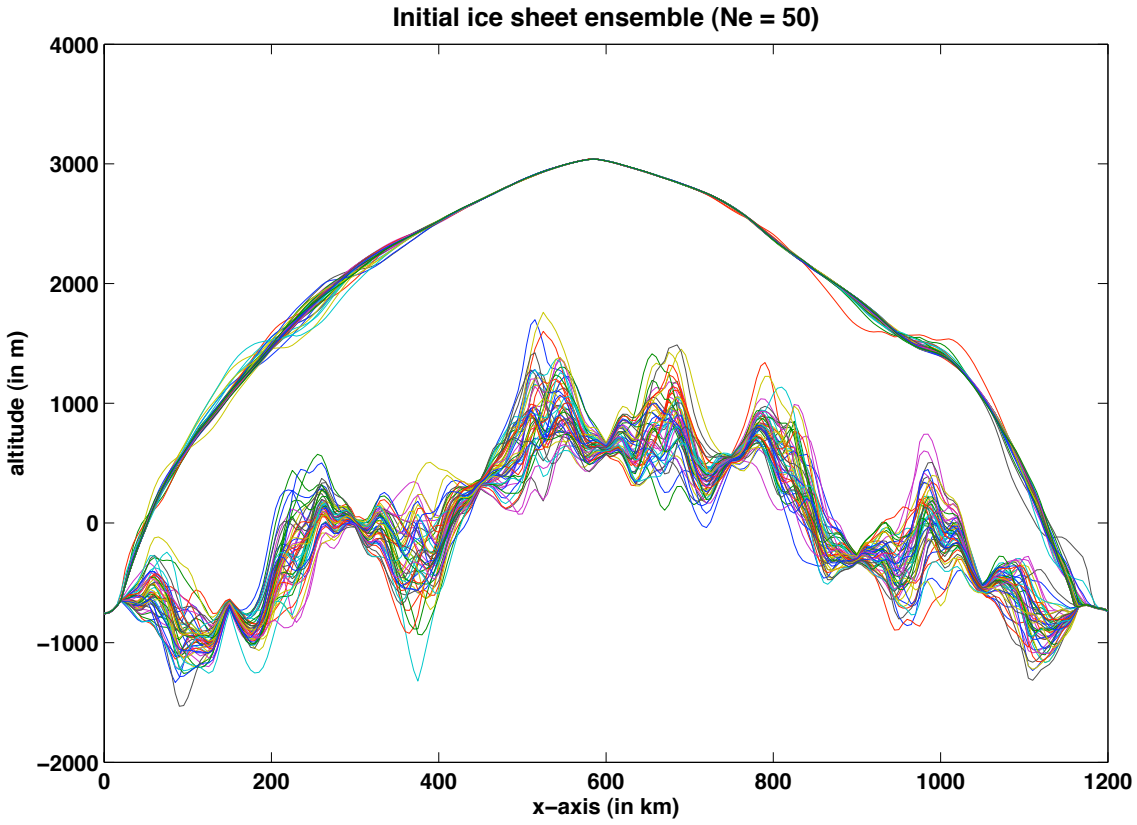

Figure 1.22: Example of initial ice sheets ensemble (50 members): bedrock topographies $B_{\text{soc}}(x)$ and surface elevation $S(x)$, as functions of the horizontal distance x.

This article addresses the problem of the polar ice-caps contribution to sea level change, as described in Section 1.2.2: how to take into account the available observations to build a good initial state, in order to produce predictions of ice volume gained or lost by the ice-cap. In section 1.2.2 we presented the problem, the available observations, and past work on the subject. Here we will look at the initialization problem in the following context:

- modern assimilation method (ensemble Kalman filter ETKF);
- large scale SIA model (currently 2D flow line);
- simultaneous inversion of the friction coefficient $\beta(x)$ and the bedrock $B_{\text{soc}}(x)$.

The chosen model is the 2D x, z SIA, specifically equations (1.10) for the conservation of mass, with $\dot{f} = 0$, equations (1.11,1.12,1.13) for dynamic (with SIA sliding velocity), and finally equations (1.16) to (1.19) for the surface mass balance.

For now, the use of the SSA (1.15) to calculate the sliding velocity $\boldsymbol{U}_{\text{slid}}$ does not work. I think we are faced with controllability problems already mentioned above: the total velocity $\boldsymbol{U}$ is divided into a deformation cunterpart which depends strongly on B_{soc} and a sliding counterpart which depends strongly on β, so that two distinct pairs B_{soc}, β can lead to two distinct pairs $\boldsymbol{U}_{\text{def}}, \boldsymbol{U}_{\text{slid}}$ leading to the same total velocity $\boldsymbol{U}$. We may have some ideas to solve this issue later, but in the meantime, the results presented here are obtained with the SIA model only.

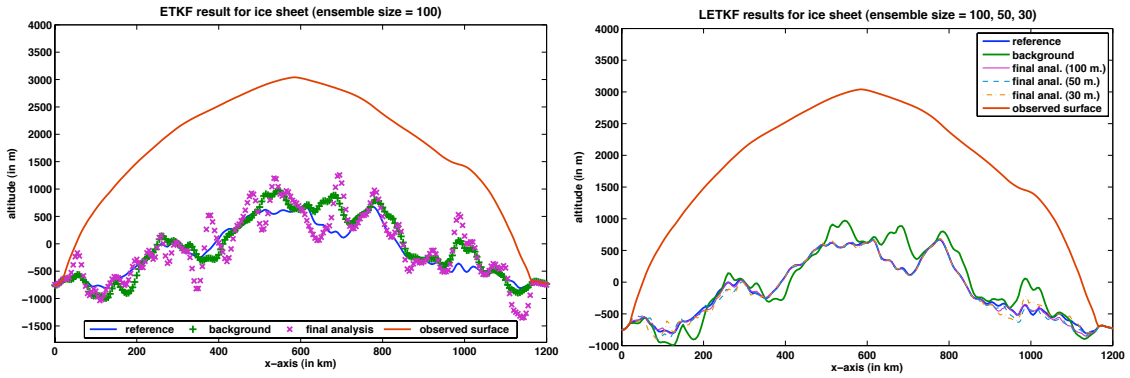

Figure 1.23: Bedrock topography after 20 years, without inflation/localisation for the 100-member ETKF (left), and with inflation/localisation for 30-, 50- and 100-member ETKF (right).

The use of a flow line model rather than a 3D model is not restrictive from a methodological point of view. Indeed, the 2D code used, Winnie, is a prototype of the 3D code GRISLI (Ritz et al., 2001), and is used for validation of the methodology. The transition to GRISLI should not pose a problem other than computing time, since it is significantly more expensive. However, the possibilities for parallelization of EnKF algorithms allow to think that the transition to GRISLI will be possible in the near future.

Methods

The assimilation method is the ETKF filter, described in Section 1.1.5. Twin experiments were performed to validate the filter, figure 1.21 presents the true state and the background chosen for $B_{\text{soc}}(x)$, $S(x)$ and $\beta(x)$, which are our control variables and parameters. The reference is a flow line of Greenland, from the east to the west, chosen so that the ends of the line lie in fast outlet glaciers (Jakobshavn on the west). In practice, fairly realistic errors between the reference and the background were imposed. The article details the construction and the choice of these values.

The elements of the ensemble are generated as realizations of a Gaussian distribution with mean equal to the background and a prescribed covariance matrix. For the bedrock, the covariance matrix is given by a pair $\boldsymbol{\Sigma}, \boldsymbol{C}$ of variances / correlations. The variances are realistic, larger where the background is very bad and smaller on the edges. Correlations are isotropic, they are given by a correlation function which is a sum of two Gaussian distributions, for capturing large and small-scale correlations. The procedure is similar for $\beta(x)$ and $S(x)$ (see the paper for more details). Figure 1.22 shows an example of ensemble members.

The observations are generated once a year for 20 years (meaning 20 analysis steps in the ETKF filter). We then observe the surface $S(x)$ and the surface velocity $U_s(x)$ at each grid point (that is to say, every 5 km). The bedrock B_{soc} is observed every 60 kilometers (every 30 grid points). To these observations is added a realistic noise: Gaussian white noise with standard deviation 2 meters for S, 3 meters / year for U_s and 20 meters for B_{soc}.

Numerical results

Here we work with the fortran 95 version of Winnie.

Large ensemble size. We first perform an validation experiment with a large ensemble (size $N_e = 1\,000$), in order to avoid problems related to undersampling. For this experiment, the results are very good: the RMS error for the bedrock goes from 207m (background0) to 46m after 20 years of ETKF. For β it is also a good reconstruction, however the RMS errors do not make much sense: indeed, beyond a certain value, the effect of β is the absence of sliding. In other words, the model can not distinguish between $\beta = 10^6$ or 10^7. Therefore, the assimilation performance assessment focuses on the "useful" counterpart of β, namely sliding veolcities. In this case, the RMS errors are not much reduced, going from 238 m/y to 230 m/y after 20 years. However, this masks good results almost everywhere on the ice-cap, with the exception of a few poorly restituted points around $x = 1\,000$. At these points, the dynamic is very singular, so that the SIA approximation is no longer valid, and the filter is also struggling to recover β. We refer to the paper for the figures.

Small ensemble sizes. We then turn to ensembles of smaller sizes, in a realistic framework for future experiments with a 3D model. Therefore, experiments were carried out with $N_e = 100$, 50 and 30. For these filter sizes it is necessary to develop inflation and localisation strategies. It can be seen in figure 1.23 (left) that without it, the results with $N_e = 100$ are poor. There is even a 50% increase of the RMS error for the bedrock after 20 analyses.

So we set up inflation and location (see the paper for details). The results, at least for the bedrock topography, are much better. Figure 1.23 (right) presents the bedrocks obtained after 20 years, we see a clear improvement over the background, even for small ensemble size.

For sliding velocities, the filter performance is less clear. They are reasonably good in most of the extent of the cap, but poor in some areas, which are those where the model itself seems to be in trouble.

This probably comes from the fact that the selected flow line crosses through fast outlet glaciers and mountain areas, and the SIA fails under these conditions. Despite this, the distribution of sliding velocity / strain rate is still better after assimilation.

1.2.7 Large scale initialisation using a variational method

This paragraph presents ongoing work, presented orally at EGU 2012, but not yet in article form.

Model and configuration

In collaboration with C. Ritz (LGGE), we also studied the problem of the joint identification of the bedrock and the sliding coefficient by a variational method, in a slightly more complex configuration than the previous one. We also work with the Winnie code (FORTRAN), still 2D (x, z), always with the SIA (1.10 to 1.12), but this time we combine it with the SSA for the contribution $\boldsymbol{U}_{\text{slid}}$ (1.15) of the velocity. The mass balance is the

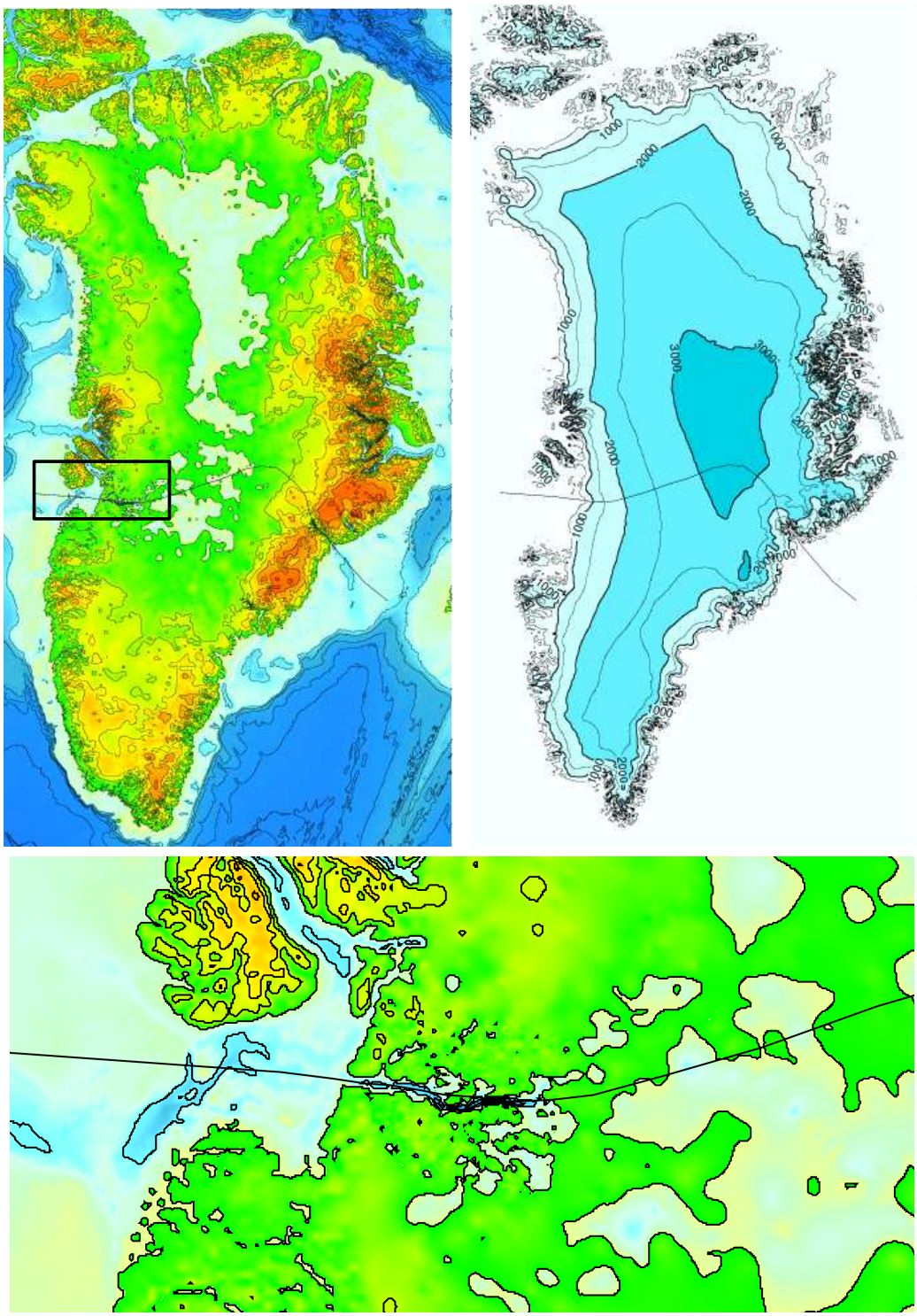

Figure 1.24: Greenland flowline. Top left, the state-of-the-art bedrock topography, and a zoom around Jakobshavn outlet glacier (bottom). Top right the observed elevation of the ice-sheet.

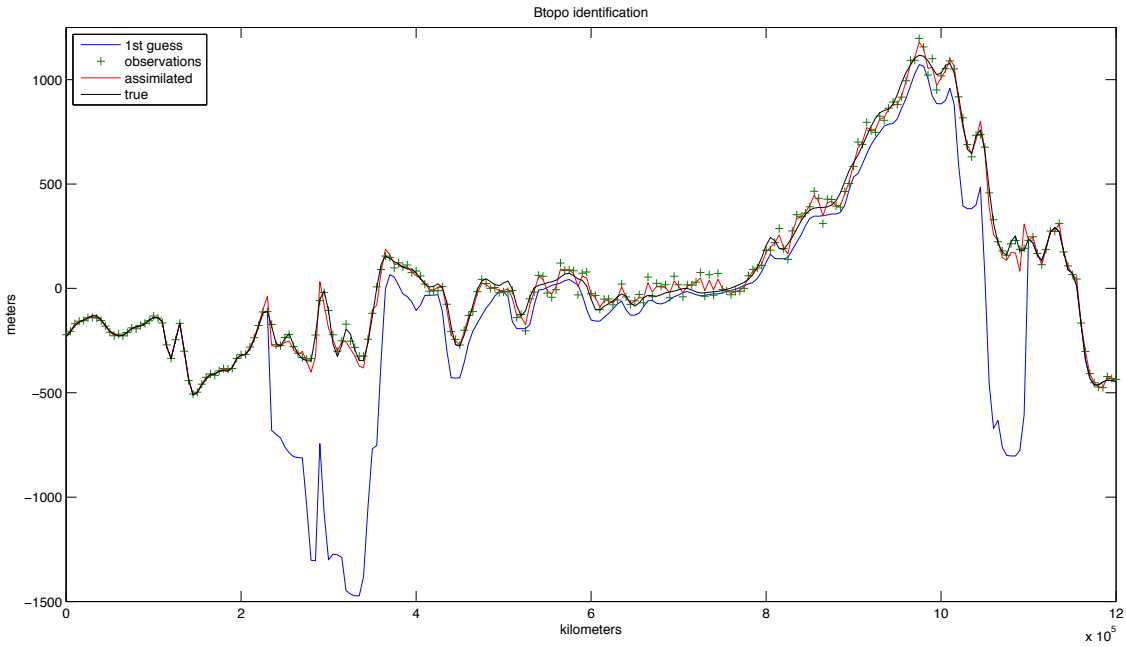

Figure 1.25: Reconstruction of the bedrock: true state, background, analysis and observations.

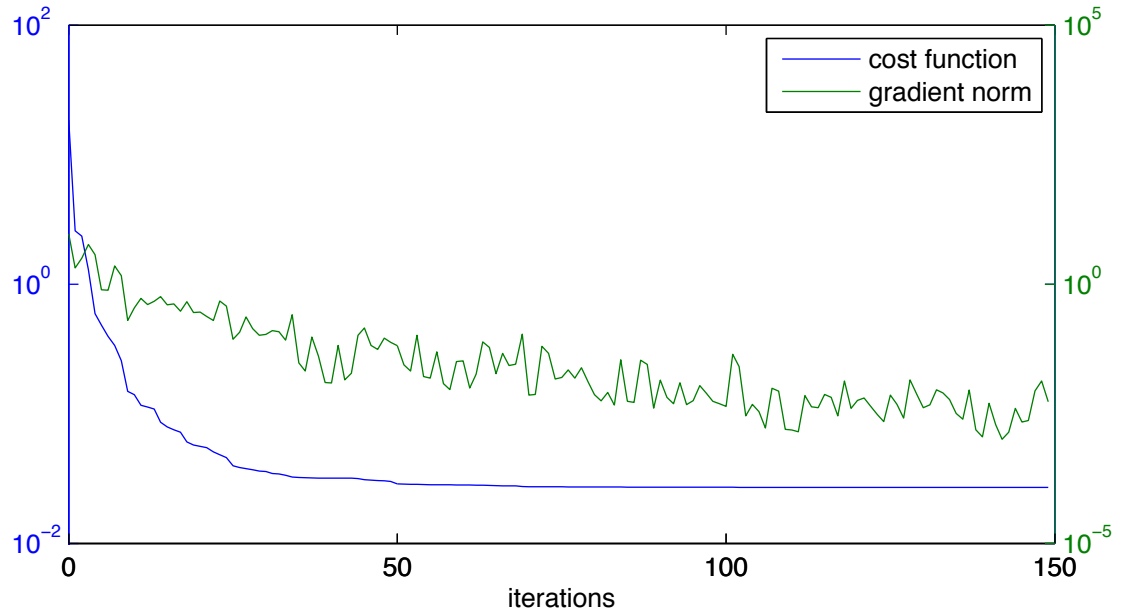

Figure 1.26: Reconstruction of β: cost function and gradient norm decrease as a function of the minimisation iteration number.

same, given by equations (1.16 1.19). The bedrock topography used for the twin experiments is also different, it is based on a real flow line of Greenland, as shown in Figure 1.24.

For the adjoint model, we use the automatic differentiation tool TAPENADE (Hascoët and Pascual, 2013). Validation tests show a high sensitivity of the quality of the results to the background choice for the bedrock and the sliding coefficient, suggesting strong nonlinearities.

We also suspect a problem of non-controllability here because, as we have said above, there is usually not uniqueness for pairs (B_{soc}, β) producing a given set of surface observations.

Twin experiments

At present, the joint identification of B_{soc} and β does not work, we present below the positive results, obtained with a 2-step assimilation (first bedrock and then sliding).

As previously twin experiments are performed. We are given a true state that is used to generate observations of surface velocities, bedrock and surface elevation. Observation noise is then added:

- for the bedrock: 20 meters in coastal areas and 100 meters inland, which is underestimated;
- for sliding: we write $\beta = 10^{\alpha}$ and take an error of 1 for α.

Regarding the background, the surface velocities and the equation of the SIA are used to estimate β, and we take for the bedrock the minimum value within a 20km-disk (on the map) of the considered point.

We then proceed in two steps:

1. β fixed to the background, DA to estimate B_{soc};
2. with the obtained bedrock, DA to estimate β.

First step: bedrock identification. Figure 1.25 shows the result. This step consists essentially in smoothing the observations. We can indeed write the cost function associated with this problem:

$$J(B) = \frac{1}{2}\|GB - B^{\text{obs}}\|^2_{R^{-1}} + \varepsilon\frac{1}{2}\|B - B^{\text{1st guess}}\|^2_{C^{-1}}$$

It is quadratic, its gradient is explicit:

$$\nabla J(B) = G^T R(GB - B^{\text{obs}}) + \varepsilon C(B - B^{\text{1st guess}})$$

At the minimum, $\nabla J(B) = 0$, and we have :

$$B^{assim} = \left(G^T RG + \varepsilon C\right)^{-1}\left(G^T RB^{\text{obs}} + CB^{\text{1st guess}}\right)$$

In practice, we did not calculate directly the bedrock with the formula above, but we used a 4D-Var algorithm with the adjoint given by TAPENADE.

Second step: basal sliding identification. In a second step, we identified $\alpha = \log_{10}(\beta)$. Figure 1.26 shows the decrease of the cost function and its gradient. The following table shows the RMS errors after assimilation and confirms the convergence :

	β	α	surface velocities error
before assimilation	74%	16%	18
after assimilation	9%	1%	0.007

where the RMS error is given by

$$RMS(X) = \frac{\|X^{\text{tru}} - X\|}{\|X^{\text{tru}}\|}.$$

Next we will have to study and correct the non-controlability, in order to jointly assimilate both variables.

1.3 Lagrangian data assimilation in oceanography

The assimilation of Lagrangian data in oceanography has been my thesis [0] *subject. In this section, we recall briefly the results* [1] [3] [12] [13]*, and we explain the extension that was done in collaboration with A. Vidard and C. Chauvin, during her post-doctoral work* [24].

1.3.1 Problem presentation

Lagrangian data

As discussed in Section 1.1.2, variational assimilation was first born in meteorology. It was then introduced in oceanography (Thacker and Long, 1988; Sheinbaum and Anderson, 1990) and is now widely used, in particular in operational oceanography (Brasseur et al., 2005). Lagrangian data are a particular type of data whose assimilation began more recently. Traditionally, the available observations in oceanography are of two kinds: in-situ (ships, buoys, moorings), or satellite. The satellite data provide a lot of information, with good spatial and temporal coverage. Their availabilty has greatly improved our knowledge of the ocean and allowed the establishment of operational forecasting systems of the ocean. However, these data cover mainly the surface of the ocean, or at least its first few meters. In-situ data, although fewer and unevenly distributed in time and space, provide information on the deeper areas of the ocean, and thus complement the satellite data. Lagrangian observations (positions of floats drifting in the ocean) are of this type. There are several types of drifting floats. Some are tracked in depth by an acoustic system, but this involves an important technical deployment and only a few campaigns have been carried out in small areas. Others derive at the surface, but in this case they are extremely sensitive to meteorological conditions and their use in a purely ocean model (without wind modelling) is complex. The last type of float is the Argo floats (or Med-Argo in the Mediterranean sea): these floats drift at a parking depth (around 1,000 meters), and every ten days (5 days in the Mediterranean) they dive down to 2 000 meters and then rise to the surface measuring the vertical profile of temperature and salinity on the way up. Once they reach the surface, they are located by GPS and transmit their data. When I started my thesis, these floats were mostly used for their temperature and salinity data, and the question of using the information in their positions was just starting to grow interest (Özgökmen et al., 2000; Ide et al., 2002; Kuznetsov et al., 2003).

Previous works

Trajectories / positions of Lagrangian floats are used in two different ways: either to get information about the Eulerian current velocities (method of pseudo-observations) or by direct assimilation (Kalman filtering or variational method). This distinction occurs because float positions are not state variables of an ocean model, which are generally the temperature T, salinity S the horizontal velocities (u, v) and the free surface of the ocean η. The relationship between the state variables and the positions is non-linear (it involves solving an advection equation), unlike most of the observations used in oceanography (which are direct observations of u v, T, S and / or η).

The method of pseudo-observations consists in converting the positions of floats into velocity information, thanks to a simple formula using growth rate, and then use these rates as new observations in a forecasting system. This simple method has been successfully used in particular for real-data studies in the Mediterranean, see Chang et al. (2011); Molcard et al. (2006); Nilsson et al. (2011); Taillandier et al. (2006, 2008).

Furthermore, direct assimilation was also studied. Unlike the method of pseudo-observations, it allows to use the observations directly. For this, it is sufficient either to use a complex observation operator or to add to the model an equation for float advection. This was done with full and Ensemble Kalman filters (see Ide et al. (2002); Kuznetsov et al. (2003); Salman et al. (2006)), and also by variational method (see my work [0] [1] [12] [13]) in the OPA model (Madec et al., 1998).

1.3.2 Lagrangian data assimilation in an operational framework

NEMOVAR

The direct assimilation works mentioned above were carried out in an idealized setting, either with simplified models or realistic models with simplified configurations. The work presented here [24] presents an implementation in the NEMO / NEMOVAR operational model. NEMO (Madec (2008)) is an ocean modeling platform, for research and operational purposes, following the ocean model OPA (Madec et al. (1998)). The NEMOVAR initiative provides tools around variational assimilation in NEMO (Mogensen et al., 2009; Vidard et al., 2010, 2012), and is currently used operationally at ECMWF and the Met-Office in the United Kingdom, and also for research by various groups.

In NEMOVAR are available: the tangent model and adjoint (NEMOTAM, Vidard et al. (2010)), implementations of variational algorithms (incremental 3D-and 4D-Var, 3D-FGAT) and several test cases (applications at different scales: local, regional, global). We refer the reader to the VODA project[11] and to Vidard (2012) for more details.

The configuration used here, called SQB (Cosme et al. (2010))), is that of an idealized ocean at midlatitudes with mesoscale resolution (1/4°) forced by a stationary surface wind, so as to obtain a double-gyre circulation. There are thus an unstable central jet and mesoscale turbulence similar to that found around the Gulf Stream.

Lagrangian floats observation operator

As mentioned above, the state vector in the ocean is composed of variables (u, v, T, S, η). The observation operator for floats is the link between the state variables (here u and v) and the observed variables, which are the positions of a float drifting at fixed depth z_0 denoted $\mathcal{X}_0\mathcal{X}_1, \ldots, \mathcal{X}_m$ at m observation times in the assimilation time window $[0, T]$. The observation operator consists in computing the trajectory on $[0, T]$, using the model velocity $U(t, x) = (u, v)$ and the initial position $\mathcal{X}_0$ at depth z_0. The equation that we consider is the following:

$$\begin{cases} \dfrac{d\mathcal{X}}{dt} = U(t, (\mathcal{X}(t), z_0)), \\ \mathcal{X}(t_0) = \mathcal{X}_0. \end{cases}$$

[11] `http://voda.gforge.inria.fr`

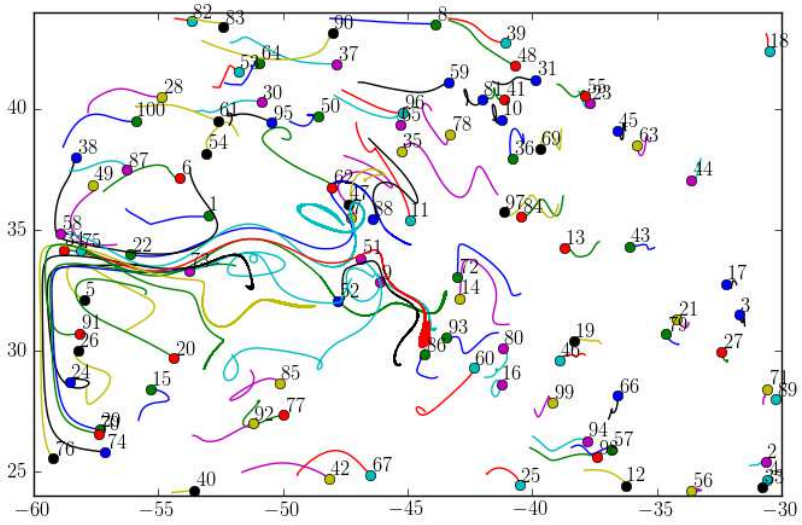

Figure 1.27: 100 float trajectories during 2 months, in the SQB configuration, between longitudes $-60°W, -30°W$ and latitudes $24°N, 44°N$.

Direct code. This equation is discretised with a leap-frog scheme:

1. initialisation

$$\left\{\begin{array}{lcl} \mathcal{X}_0 & & \text{given,} \\ \mathbb{U}_0 & = & \boldsymbol{I}(U_0, \mathcal{X}_0). \end{array}\right. \qquad \left\{\begin{array}{ll} \mathcal{X}_1 & = \mathcal{X}_0 + \Delta t\, \mathbb{U}_0, \\ \mathbb{U}_1 & = \boldsymbol{I}(U_1, \mathcal{X}_1). \end{array}\right.$$

2. for $t_k,\ k = 2, \ldots, n$:

$$\left\{\begin{array}{l} \mathcal{X}_k = \mathcal{X}_{k-2} + 2\Delta t\, \mathbb{U}_{k-1}, \\ \mathbb{U}_k = \boldsymbol{I}(U_k, \mathcal{X}_k). \end{array}\right.$$

The time step Δt is equal (or multiple) to the direct ocean model time step. The operator $\boldsymbol{I}(U, \mathcal{X})$ is an interpolation operator for $U(t, \mathcal{X})$. Indeed, in the discrete model U is a vector available only on the grid, while the float generally drifts off grid points. Assume for simplicity that z_0 is a vertical level of the grid (see [24] for the general case). In this case, the interpolation consists in identifying the four horizontal grid-points around $\mathcal{X}$, then look for the weight a_i such that

$$\mathcal{X} = \sum_{i=1}^{4} a_i Q_i,$$

and then setting

$$\boldsymbol{I}(f, \mathcal{X}) = \sum_{i=1}^{4} a_i f(Q_i)$$

Figure 1.27 presents a hundred trajectories of floats drifting for two months in the SQB configuration. These trajectories clearly show the chaotic nature of the flow, since you can see floats close initially take different paths, especially in the area around latitude 34 °N and longitudes between -60 and -40 °W, which is that of the jet.

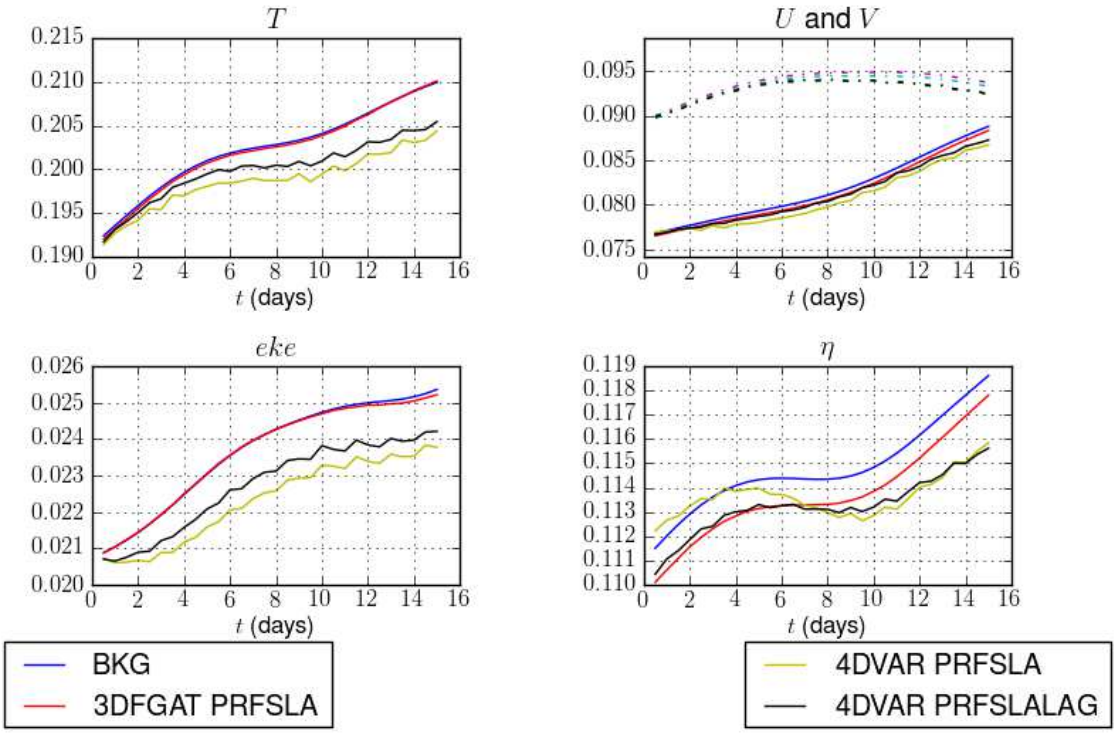

Figure 1.28: Comparison of RMS errors for the five variables T, U, V, eke and η. Three experiments are compared to the background (blue): 3D FGAT with observations of profiles and sea level height (red), incremental 4D-Var with observations of profiles and sea level height (yellow) and then with also the Lagrangian observations (black).

Tangent code. We derive the leap-frog scheme to obtain the tangent code:

$$\begin{cases} \delta\mathcal{X}_k = \delta\mathcal{X}_{k-2} + 2\Delta t\, \delta\mathbb{U}_{k-1}, \\ \delta\mathbb{U}_k = \boldsymbol{I}(\delta U_k, \mathcal{X}_k) + \delta\mathcal{X}_k . \dfrac{\partial \boldsymbol{I}}{\partial \mathcal{X}_k}(U_k, \mathcal{X}_k). \end{cases}$$

Here we see that it is necessary to derive the interpolation operator $\boldsymbol{I}$. Its derivative with respect to U is simple, because $\boldsymbol{I}$ is linear in U. On the contrary, the derivative with respect to the position is more complex, and it relies on a good choice of the method for calculating the weights a_i. We use the method proposed by Daget (2006) It is an iterative method which has the advantage of being both accurate for interpolation, and quite easily derivable with respect to the a_i. We refer to [24] for details.

Numerical results

We refer to the document [24] for the description and validation of algorithms 3D-FGAT and incremental 4D-Var (and sections 1.1.2 and 1.1.3 for a reminder on these algorithms). Experiments of 15 or 30 days are carried out in our idealized but realistic configuration, in the framework of twin experiments: a true state is chosen, and used to generate observations. We selected observations according to what was available in the actual area SQB

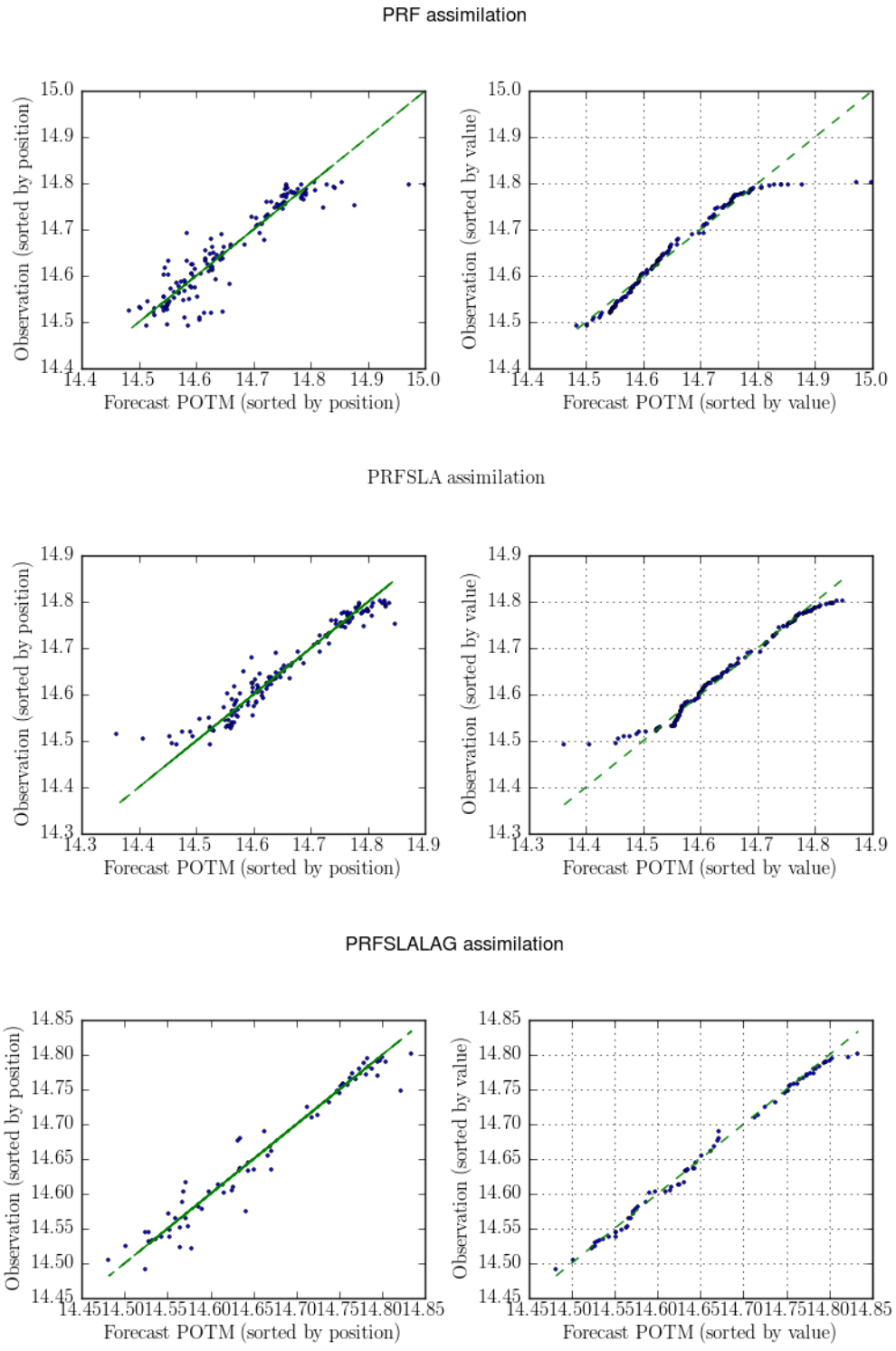

Figure 1.29: Statistics charts for temperature profiles for different assimilation experiments (top: profiles only, middle: plus sea level height in the middle, bottom: plus Lagrangian observations). On the left, the cloud of observed / predicted temperature for each measurement point. On the right, diagram quantile-quantile for the observed / predicted temperatures.

in January 2010:

- 49 floats drift at about a thousand feet deep, and measure vertical profiles of temperature and salinity between 2 000 m and 200 m. 84 profiles in total are available for this month. The associated observations are denoted PRF in the sequel.
- ENVISAT satellite periodically measures the sea level anomalies, denoted in the SLA later on. We have about 12,800 measurements for a month throughout the area.
- Finally, each float gives its position every 10 or 15 days, we denote these observations LAG.

The document [24] shows that the assimilation of profiles PRF and sea level anomaly SLA performs well and that these two types of information are complementary. So here we focus only on the results associated with Lagrangian data LAG. Figure 1.28 presents the RMS errors for the five variables T, U, V, eke (turbulent kinetic energy) and η, either for the background (no assimilation), or for the PRF + SLA observations (3D-FGAT and incremental 4D-Var) or PRF + SLA + LAG (incremental 4D-Var). It is then found that the addition of Lagrangian observations does not improve the RMS errors, and even slightly degrades the temperature and turbulent kinetic energy. We can suggest several explanations for this: first, "large scale" data assimilation (with PRF and SLA) introduce small-scale phenomena into the analysis increment. They disrupt the float trajectories and thus perturb the minimisation. Moreover, an incremental algorithm (which supposes to linearize the model) is used here with a 15-day assimilation window. We see in the document [24] that the validity period of the tangent linear hypothesis depends on which observations are considered: it is long enough for the state variables (more than 30 days), but for the floats positions it is around 8 days, which is less than the position time sampling and probably poses a problem here. However, the choice of 15 days is a compromise between the tangent linear hypothesis (the shorter the better) and the number of data (longer window means more observations).

However, we see a gain of assimilating Lagrangian positions when comparing the distributions of observed and predicted temperatures. For this, we present in Figure 1.29 two types of statistical charts. In the left column, we simply draw the cloud of points formed by the temperature observed of one profiler (y axis) and the temperature forecast of the same profiler (x axis). The proximity to the line $y = x$ shows the reliability of the prediction with respect to the observations. In the left column, we draw a quantile-quantile plot (QQ plot). To do so, we class in ascending order all temperature observations, then all the predicted temperature. Then the smallest observed temperature is associated to the smallest predicted temperature, and we draw the point on the graph. We apply the same procedure for the second smallest value, and so on. Therefore we have a plot of the quantiles of the observed distribution as a function of those of the predicted distribution. The proximity to the line $y = x$ shows the match between the two distributions. For this type of diagnosis we could see the advantage of assimilating Lagrangian data: the adequacy between observation / prediction is improved with the addition of Lagrangian positions, especially for the extreme values of temperature.

However, the document presents the same diagrams for η and these are instead degraded by the assimilation of Lagrangian observations.

These mixed results were disappointing, so we gave up trying to apply this method to real data and I set aside this research direction at the moment.

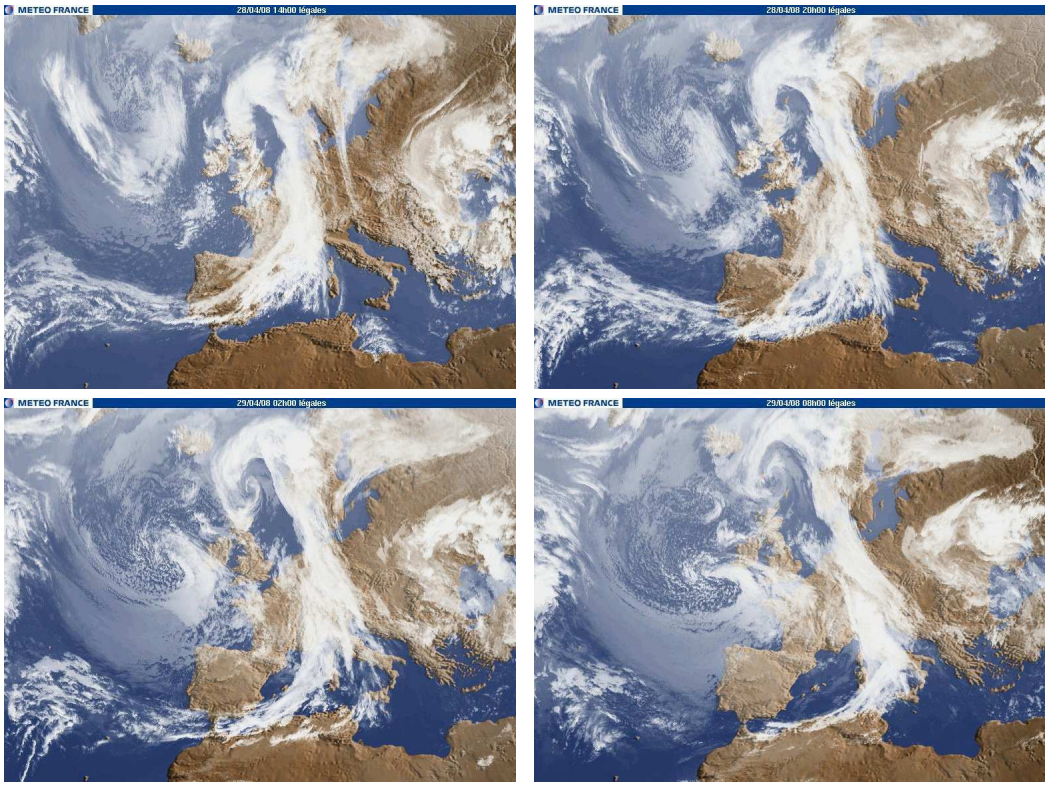

Figure 1.30: Meteosat image sequence, April 2008, 6h gap between each image (source : Météo France).

1.4 Image sequences data assimilation

Assimilation of image sequences is conceptually very close to Lagrangian data assimilation, as we will see below. When I joined the MOISE team it became a natural interest, because A. Vidard, F.-X. The Dimet and (post)-graduate students already worked on this issue. This section first presents the specificities of images and reports on the state of the art of image assimilation, especially on the earlier MOISE work (F.-X. Le Dimet, A. Vidard, O. Titaud, I. Souopgui). Finally, I present the work in progress [23] *as part of the PhD of V. Chabot, of whom A. Vidard and myself are co-advisors. I also present the conference papers* [19] [20]*, in collaboration with N. Papadakis and A. Makris.*

1.4.1 Image sequences: interests and challenges

Image sequences are a particular type of observation that is used (or that we would like to use) in data assimilation in different domains: meteorology, oceanography, glaciology, agronomy, seismology, etc. The work presented in [23] is intended to meteorology and oceanography, so the examples are restricted to these areas.

Image sequences have both advantages and disadvantages in terms of data assimilation.

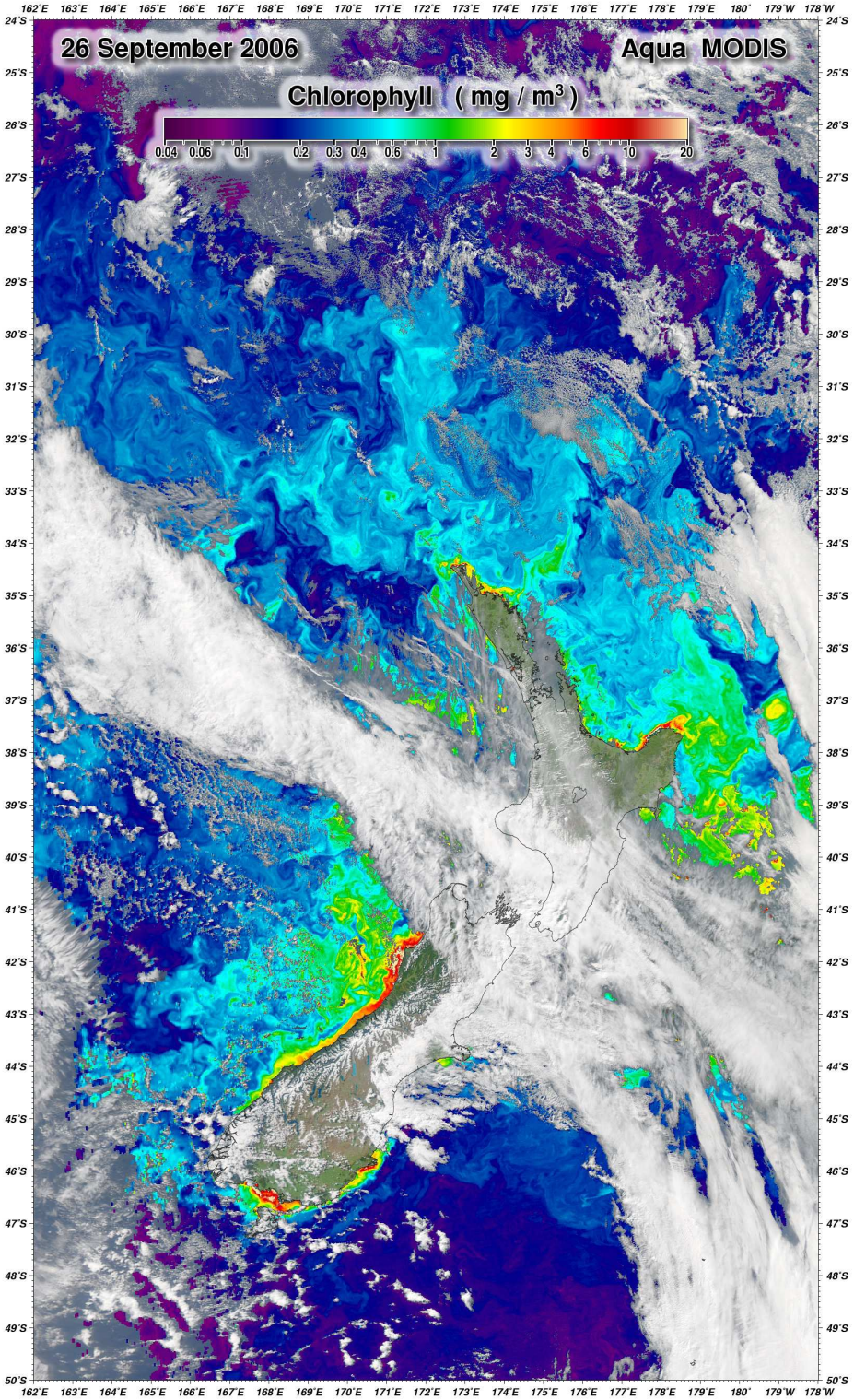

Figure 1.31: New Zealand Eddies. (source : image MODIS)

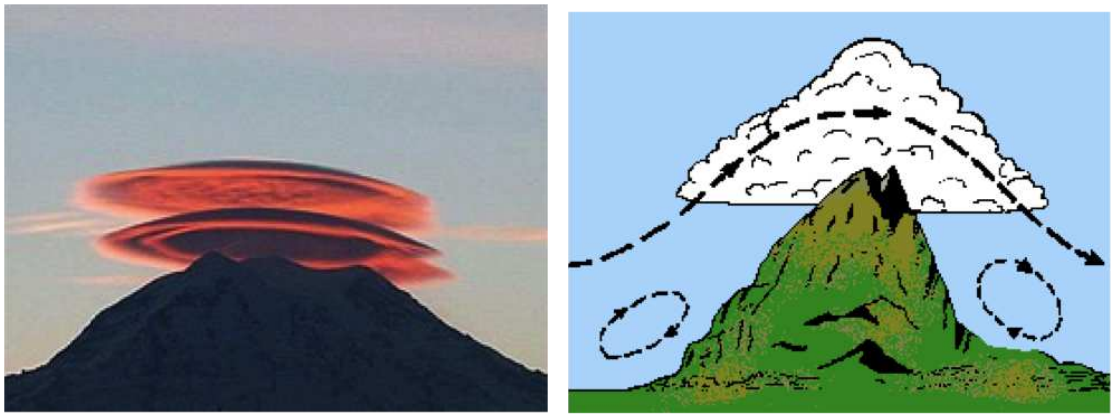

Figure 1.32: Lenticular clouds. They appear not to move, despite the strong horizontal wind at their location.

A large informative potential, but exploitable with difficulty. On the plus side, this data type clearly has a great informative potential. Just to be convinced we can look at figure 1.30, which presents a sequence of four successive Meteosat images (six hour interval): it clearly shows the movement of fronts, and an experienced forecaster can draw from this sequence valuable information.

However, it is difficult to use these images as is in environmental prediction systems. Indeed, images are not (in general) state variables of the model, as the Lagrangian data. This is a 2D interpretation of 3D processes involving other variables (passive or active tracer: humidity, temperature, chlorophyll, etc.). It therefore requires complex observation operators, including partial differential equations resolution (as for Lagrangian observations).

In addition, as for Lagrangian data, the images are a reflection of multi-scale processes, and in particular small scale processes that are not resolved by the model.

A large amount of data, but of questionable quality. Satellites, either geostationary or with polar orbit, provide daily a large amount of images. However, the images produced are composite, that is to say, they are the combination of several shots. MeteoSat takes fifteen minutes to produce a shot-by-shot image, which is therefore quite homogeneous. Conversely, sea level height images are produced by a polar orbiting satellite that can take several days to cover a given area. It is easily seen that this can cause problems in assimilation, because of inconsistencies in data or between model and data whose dates do not match.

In addition, in particular in oceanography, there are often "gaps" in the images because of concealment by clouds, as can be seen in figure 1.31, which presents chlorophyll around New Zealand.

In meteorology, knowing the height of clouds from 2D images is also an open problem.

Another problem, common to weather forecasting and oceanography, is the aliasing issue, where the apparent motion can be very different from reality. E.g., lenticular clouds seem to be motionless whereas there is a strong horizontal wind, see Figure 1.32.

1.4.2 Previous works

Pseudo-observations

Currently, the data are not directly used in weather forecasting systems, but they are transformed into usable information (called pseudo-observation) that is fed to the DA system. We briefly explain below what it is, and we refer the reader to Vidard (2012); Souopgui (2010) for more details and references on the subject.

Bogus. The easiest way is to track some structures in the image sequence, and to assimilate them as position data in the model. Historically done by hand, this following of structures has now been automated by Michel and Bouttier (2006), and applied to the potential vorticity in Michel (2011). Similarly, Thomas et al. (2010) track convective cells to do atmospheric variational DA.

Atmospheric Motion Vectors (AMV). Other methods of pseudo-observations consist in using the image sequence to derive an apparent velocity field, which can then be assimilated, see eg Schmetz et al. (1993). The idea is similar to the PIV (Particle Image Velocimetry, see Wikipedia for introduction and Adrian (1991) for the reference article). The idea is to put particles in the fluid, which will be visible on the images. Then we identify each particle and follow it in the sequence of images to obtain a velocity vector. This is done by a cross-correlation statistical method, to match particles in different images.

The AMV are produced in the same way, atmospheric clouds playing the role of particles in the flow.

Optical flow. The optical flow is another class of method aiming to produce effective velocity fileds. The idea is to look for a vector field w which transports images while preserving luminosity I (Horn and Schunck, 1981):

$$\partial_t I + \nabla I.w = 0, \quad I(0) = I_0 \tag{1.20}$$

As this constant brightness hypothesis provides only one scalar equation and we seek a motion vector, the problem of optical flow has an infinite number of solutions (aperture problem). Therefore it must be regularised, see eg Auroux and Fehrenbach (2010) for a comparison of regularisations. One can also cite Corpetti et al. (2002), who interpret the brightness conservation as a continuity equation in a fluid, and gives better results for images from fluids.

Image model. As the optical flow provides a vector field *between two successive images*, the obtained velocity field is not necessarily consistent over time. The idea of image model by Herlin et al. (2006) is to add to the optical flow equation an evolution model for w:

$$\partial_t w = \mathcal{M}(w), \quad w(t=0) = w_0 \tag{1.21}$$

where $\mathcal{M}$ is a simplified 2D dynamical model. Then we minimise the cost function:

$$\mathcal{J}(w_0) = \|I - I^{\text{obs}}\|^2 + \text{regularisation}$$

under the constraints (1.20,1.21).

Direct assimilation

Pseudo-observations use is convenient, because it is (relatively) easy to implement into an existing DA system. However, the transformations required to create the pseudo-observations generate errors, which we poorly know and are usually correlated in space.

Thus we would like to avoid pseudo-observations, and to directly assimilate the images using an appropriate observation operator. In the formalism of 4D-Var, this amounts to minimize a cost function $\mathcal{J} = \mathcal{J}^o + \mathcal{J}^b$ consisting of an observation term and a background term, under constraint of the model equation.

Pixels. The first idea to build the observation operator is simply to use

$$\mathcal{J}^o(\boldsymbol{x}_0) = \sum_{t_0}^{t_f} \|\boldsymbol{H}(\boldsymbol{x}_0)(t) - \boldsymbol{y}^o(t)\|^2_{\boldsymbol{R}_{pix}}$$

where $\boldsymbol{y}^o$ is the vector containing the value of the image brightness and $\boldsymbol{R}_{pix}$ the observation error covariance matrix. The size of $\boldsymbol{y}^o$ is equal to the number of pixels in the image. The observation operator then contains the image production from the model state variables. In our work, it consists in considering the density q of a tracer transported by the fluid:

$$\partial_t q + \nabla q.\boldsymbol{U} - \nu\Delta q, \quad q(t_0) = q_0 \tag{1.22}$$

where $\boldsymbol{U}$ is the 2D velocity field at the image vertical level, ν is the diffusion coefficient, and q_0 is the initial concentration (obtained for example thanks to the first image). E.g., figure 1.33 presents a comparison between an observed image and its model equivalent.

The first works on the subject include Huot et al. (2010) and Papadakis and Mémin (2008) (with a different observation operator, based on the optical flow equation). The latter study showed that the direct assimilation gave better results (in a simple case of 2D flow) that the one using pseudo-observations of optical flow. However, this type of "pixel by pixel" comparison between the model and the image seems poorly appropriate, because it does not take any account of the image structures. Thus, other direct approaches have been developed that attempt to extract the relevant information from the images.

Multiscale decomposition. The first approach is that of Titaud et al. (2010); Souopgui (2010), which is to decompose the image in a multi-scale basis of curvelets (Candes and Donoho, 2000; Candes et al., 2006) or wavelets (Mallat, 1998) and compare the multi-scale decompositions of the image and its model equivalent. The cost function then writes

$$\mathcal{J}^o(\boldsymbol{x}_0) = \sum_{t_0}^{t_f} \|W(q(t)) - W(\boldsymbol{y}^o(t))\|^2_{R_{wav}}$$

where W is the chosen wavelet decomposition.

As these multi-scale decompositions verify a Parseval equality type, multi-scale distance is equivalent to the pixel distance. The idea of these works is to keep only a portion of the coefficients. This is called "thresholding" and it consists in keeping only the leading coefficients (eg the 5% most important coefficients of the image, or 5% for each major scale, etc.). Souopgui (2010) showed that the choice of threshold was crucial in the assimilation

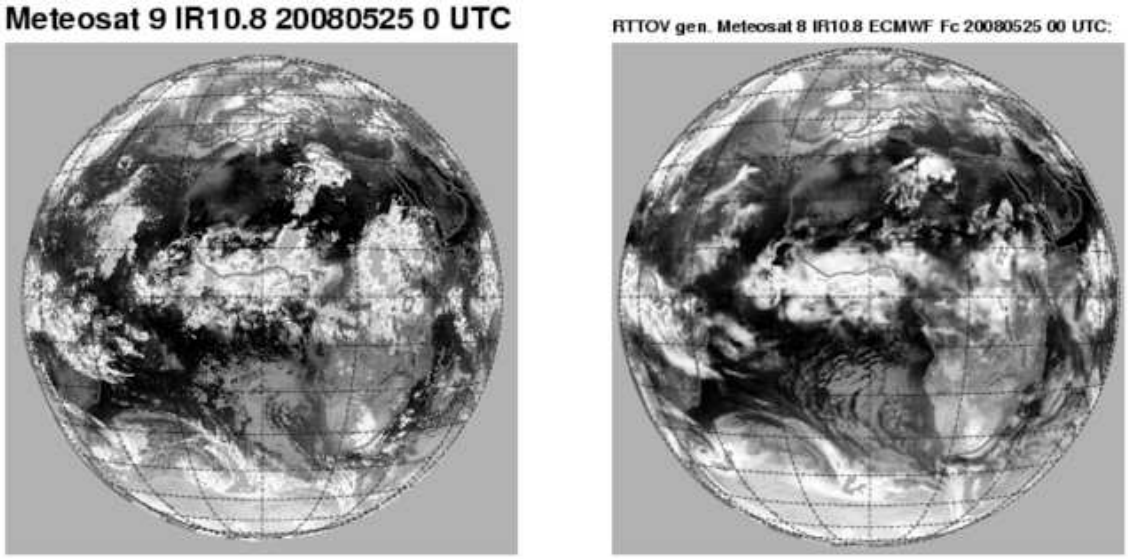

Figure 1.33: Model (right) data (left) comparison (source: ECMWF).

of multi-scale images. The cost function then is

$$\mathcal{J}^o(\boldsymbol{x}_0) = \sum_{t_0}^{t_f} \| \mathbb{1}_{\Omega_I} \circ W(q(t)) - \tau \circ W(\boldsymbol{y}^o(t)) \|^2_{\tilde{R}_{wav}}$$

where τ is the thresholding operator, applied to the observed image. This allows to define a working subspace Ω_I in which we project the model equivalent, in order to compare it to the observation. In the following study, thresholding consists in keeping the largest coefficients and discarding the smallest.

Other approach. Another way to extract information relative to image structures has been explored in Titaud et al. (2011), who make a map of Lagrangian Coherent Structures (LCS), related to the Lyapunov exponents of the fluid (see Vidard (2012) for a review).

1.4.3 Current works

The model is a Shallow-Water code in FORTRAN 90, with the image assimilation library BALAISE (Souopgui, 2010), which we enhance with the methods and operators presented below.

Gradient based observation operators

The starting point of this study is as follows: the relevant information of the image is contained in the fronts, ie areas of high gradient in the image. Thus, it is proposed in [23] to consider two observation operators based on gradients.

Gradient operator. The first operator simply computes the image gradients, leading to the following cost function:

$$\mathcal{J}^{\text{grad}}(\boldsymbol{x}_0) = \frac{1}{2}\sum_{i=1}^{N} \|\nabla I_i - \nabla q_i\|^2_{R_i^{-1}}$$

where $(I_i)_{i=1..N}$ is the observed image sequence and $(q_i)_{i=1..N}$ the tracer defined by equation 1.22 (discretised), where $\boldsymbol{U}$ is given by the fluid model, initialised with $\boldsymbol{x}_0$.

Angular operator. For the second operator, we would like to measure the angular difference between the gradients of the image and those produced by the model. For this we want to compare the unit vectors $\nabla I/\|\nabla I\|$ and $\nabla q/\|\nabla q\|$. Here $\|.\|$ represents the Euclidean norm in two dimensions, so that at each pixel (x_k, y_k) of the image the unit vector can be defined as follows:

$$\frac{\nabla I}{\|\nabla I\|}(x_k, y_k) = \frac{1}{\sqrt{\partial_x I(x_k, y_k)^2 + \partial_y I(x_k, y_k)^2}}(\partial_x I(x_k, y_k), \partial_y I(x_k, y_k))$$

where the derivative ∂_x, ∂_y is computed using finite differences.

Naturally, this formula cannot be applied where ∇I is null, so we replace the norm $\|.\|$ by $\|.\|_\varepsilon$, with

$$\|a\|^2_\varepsilon = a_x^2 + a_y^2 + \varepsilon$$

where ε is well-chosen (see [23] for more details), such that $\nabla I/\|\nabla I\|_\varepsilon$ is either zero either close to $\nabla I/\|\nabla I\|$. The cost function then writes:

$$\mathcal{J}^{\text{ang}}(\boldsymbol{x}_0) = \frac{1}{2}\sum_{i=1}^{N} \| \frac{\nabla I}{\|\nabla I\|_\varepsilon} - \frac{\nabla I}{\|\nabla I\|_\varepsilon} \|^2_{R_i^{-1}}\, dt$$

Validation with perfect data

The relevance of these two operators is studied through twin experiments with perfect data (not noisy). The experimental conditions are those of the experimental Coriolis platform[12], ie a Shallow-Water model with β-plane Coriolis forcing, ie $f = f_0 + \beta y$ (where y is the latitude and f the Coriolis force). The state variables are the horizontal velocities $\boldsymbol{U} = (u, v)$ and the water height h. They also are the control variables, ie the variables we try to identify through data assimilation. The simulation is done on a square subdomain of the platform, and figure 1.34 shows the initial velocities, tracer and vorticity $\zeta_0 = \partial_x v_0 - \partial_y u_0$. These initial values allow to generate observations, which we later use in our DA system with the various observation operators. To validate quantitatively the results we compute the following ratio:

$$\frac{RMSE(x_0^a)}{RMSE(x_0^b)}, \text{ with } RMSE(x) = \|x - x^t\|$$

using for x successively each variable u_0, v_0, h_0 (exponent a for analysis, b for background and t for true). Figure 1.35 presents the evolution of this RMSE quotient for u_0 as a function of the number of minimisation iterations. We can see that every observation operator allows a decrease of the RMSE under 10% of the background error (without assimilation), the angular operator being the most efficient.

[12] `http://coriolis.legi.grenoble-inp.fr`

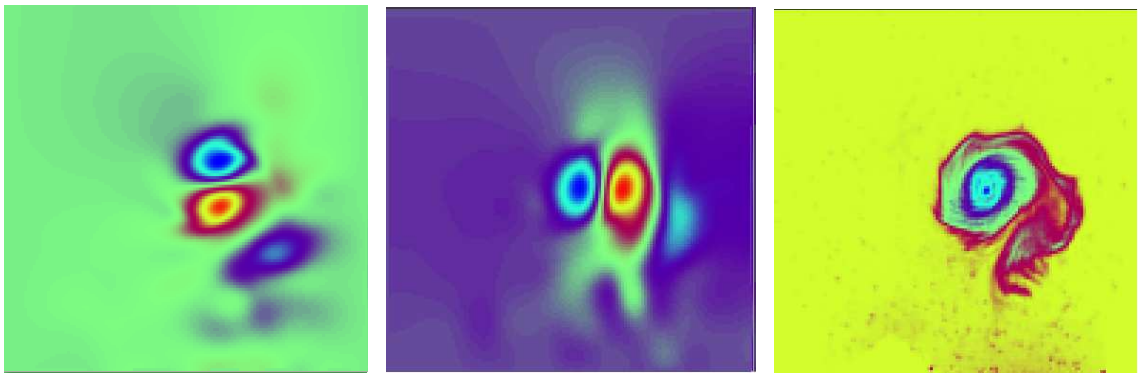

Figure 1.34: Initial values for the twin experiments: on the left and in the middle the "true" horizontal velocities u_0 and v_0. On the right the first image of the passive tracer q_1.

Image assimilation with noisy observations

As work on this subject is still in progress, I will not go into details but I will present the preliminary results [20]. The idea of this work is to consider the assimilation of noisy images with spatially-correlated Gaussian noise. As a result, the observation error covariance matrix cannot be chosen proportional to the identity as we do in general.

Noisy observations. Three noise levels are considered, presented in figure 1.36. For these images the correlation matrix of the noise is identical, the only difference lies in the noise intensity, which is measured using the Signal to Noise Ratio (SNR):

$$SNR = 10 \log_{10} \left(\frac{\sum_{\boldsymbol{x} \in \Omega} (I^t(\boldsymbol{x})^2)}{\sum_{\boldsymbol{x} \in \Omega} (I^t(\boldsymbol{x}) - I^o(\boldsymbol{x}))^2} \right)$$

Observation error covariance matrix modelling. In the sequel $\boldsymbol{R}^t_{pix}$ represents the true observation error covariance matrix in the pixels space. As the noise is space-correlated, this matrix is not diagonal. As the noise level is homogeneous, its diagonal is constant, equal to σ^2_{true}.

In the preliminary experiments of [20], we chose to consider only diagonal $\boldsymbol{R}$ matrices, and we compare the following distances:

- *Pixels.* We choose the diagonal of the true matrix:

$$\boldsymbol{R}_{pix} = \text{diag}(\boldsymbol{R}^t_{pix}) = \sigma^2_{true} \boldsymbol{I}_n, \quad n = \#\text{pixels}$$

- *Wavelets with thresholding.* We then choose to quantify the impact of thresholding τ on the previous distance. To do so, we transport $\boldsymbol{R}_{pix}$ (which is diagonal) into the thresholded wavelet space (Daubechies here). We get:

$$\boldsymbol{R}_{W_\tau} = \tau W_{D8} \, \text{diag}(\boldsymbol{R}^t_{pix}) W^T_{D8} \tau^T = \sigma^2_{true} \boldsymbol{I}_k, \quad k = \#\Omega_I$$

  where the identity matrix is taken over the space Ω_I. We can see that if thresholding vanishes we find the pixels distance. This matrix choice allows to evaluate the impact of thresholding only, for a diagonal matrix in pixel space.

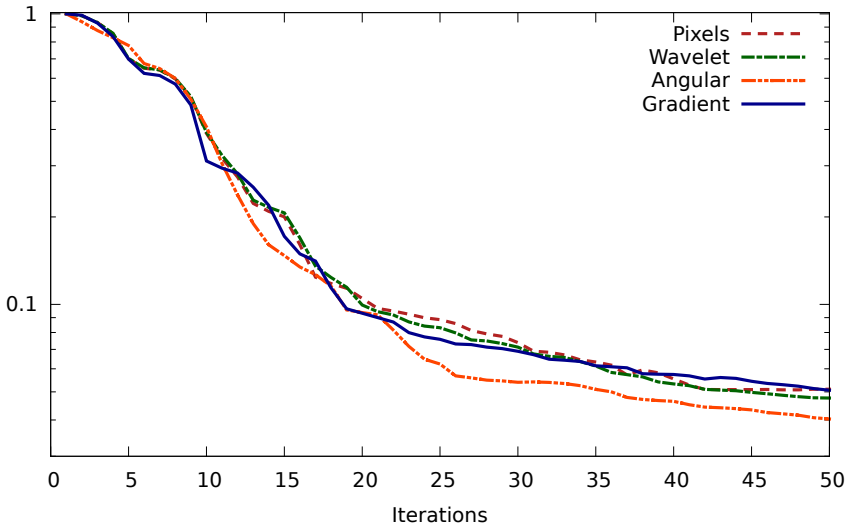

Figure 1.35: Evolution of the ratio of RMS errors of the velocity u with respect to 4D-Var iterations. Perfect data are observed and the four observators are compared.

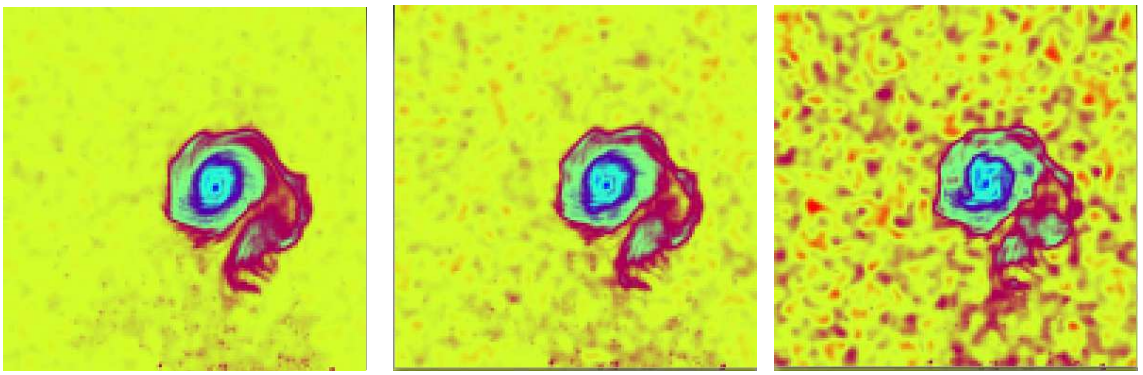

Figure 1.36: Example of noisy observations for each noise level. The SNR (signal to noise ratio) on the left is 26.8dB, in the middle 20.8dB and on the right 14.8dB.

- *Gradients.* The true matrix in this space is $\nabla \boldsymbol{R}_{pix}^t \nabla^T$, we take its diagonal:

$$\boldsymbol{R}_{grad} = \mathrm{diag}(\nabla \boldsymbol{R}_{pix}^t \nabla^T)$$

  As the correlations are isotropic, this matrix is also proportional to the identity matrix.

- *Haar wavelets without thresholding.* The true covariance matrix is $W_{Haar} \boldsymbol{R}_{pix}^t W_{Haar}^T$, we choose its diagonal:

$$\boldsymbol{R}_{Haar} = \mathrm{diag}(W_{Haar} \boldsymbol{R}_{pix}^t W_{Haar}^T)$$

- *Daubechies wavelets without thresholding.* Finally, without thresholding, we choose:

$$\boldsymbol{R}_{D8} = \mathrm{diag}(W_{D8} \boldsymbol{R}_{pix}^t W_{D8}^T)$$

  which is the diagonal of the true covariance matrix.

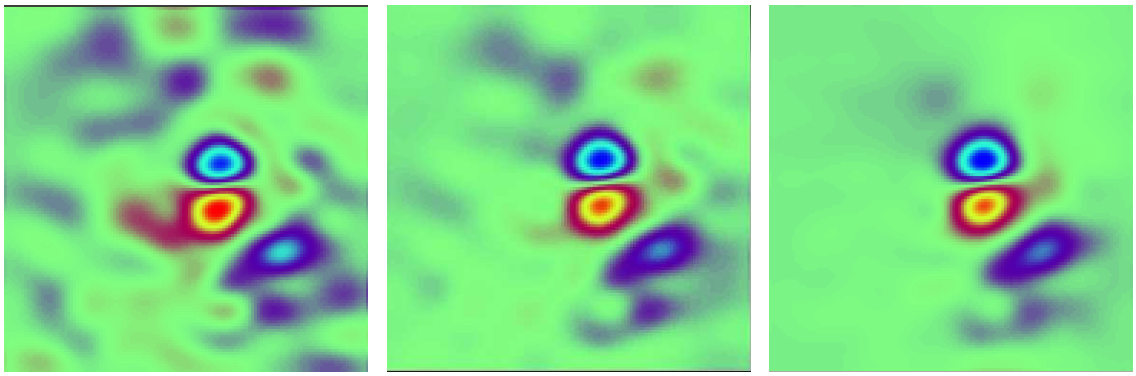

Figure 1.37: Analysis u for an image sequence with large noise (SNR 14.8 dB). On the left, analysis with the pixel distance, in the middle with the gradients, on the right with Daubechies wavelets.

Table 1.1: Residual error in the analysis, averaged over 10 experiments, with respect to the background, as a function of the noise level (SNR).

	Pixels	W_τ	Gradients	D8	Haar
14.8 dB	60.8%	60.1%	34.0%	9.3%	22.8%
20.8 dB	26.2%	28.5%	17.8%	7.6%	12.5%
26.8 dB	15.6%	17.1%	12.4%	7.2%	8.4%
Perfect data	7.6%	8.5%	7.4%	7.1%	6.4%

Note that if we change variable to bring back the matrices into the pixel space, we find that the last three $\boldsymbol{R}$ produce non diagonal covariance matrices. Conversely, the first two assume that the error in pixel space is uncorrelated.

Note also that it would have been nice to compare the impact of thresholding *with a non diagonal matrix*, e.g. with

$$\boldsymbol{R} = \mathrm{diag}(\tau W_{D8} \boldsymbol{R}^t_{pix} W^T_{D8} \tau^T)$$

but this is still under development.

Results. Table 1.1 presents the ratio between RMS for the analysis and RMS for the background, for the three various noise levels, and the various distances/matrices choices, as presented before. We can first notice that the pixel distance is not robust to noise, as is not W_τ with a matrix proportional to the identity. However, in particular for a high noise level, we can see that gradients and wavelets without thresholding give the best results. So, a well chosen diagonal matrix is preferable to the identity matrix.

Finally, figure 1.37 shows the analysed velocity field u with a strong noise for pixels, gradients and D8, confirming the good performance of the last two compared to the pixels.

These results are of course preliminary, as diagonal matrices were used. However, the high sensitivity of the results with respect to the matrix choice is encouraging. It shows that modelling efforts toward $\boldsymbol{R}$, even modest, can improve the results.

1.5 Bibliography 1

R. Adrian. Particle imaging techniques for experimental uid mechanics. *Annal Rev. Fluid Mech.*, 23:261304, 1991.

Jeffrey L Anderson and Stephen L Anderson. A monte carlo implementation of the nonlinear filtering problem to produce ensemble assimilations and forecasts. *Monthly Weather Review*, 127(12):2741–2758, 1999.

R. J. Arthern and R. C. A. Hindmarsh. Optimal estimation of changes in the mass of ice sheets. *Journal of Geophysical Research*, 108:6007, 2003.

Robert J Arthern and G H Gudmundsson. Initialization of ice-sheet forecasts viewed as an inverse Robin problem. *Journal of Glaciology*, 56(197):527–533, 2010.

Robert J Arthern and R C A Hindmarsh. Determining the contribution of Antarctica to sea-level rise using data assimilation methods. *Philosophical Transactions of the Royal Society A: Mathematical, Physical and Engineering Sciences*, 364(1844):1841–1865, July 2006.

Didier Auroux and Jérôme Fehrenbach. Identification of velocity fields for geophysical fluids from a sequence of images. *Experiments in Fluids*, 50(2):313–328, July 2010.

J. L. Bamber, R. L. Layberry, and S. P. Gogineni. A new ice thickness and bed data set for the greenland ice sheet 1. measurement, data reduction, and errors. *J. Geophys. Res.*, 106:33773–33780, 2001.

J N Bassis. Hamilton-type principles applied to ice-sheet dynamics: new approximations for large-scale ice-sheet flow. *Journal of Glaciology*, 56(197):497–513, 2010.

L Berliner, K. Jezek, N. Cressie, Y. Kim, C. Q. Lam, and C. J. van der Veen. Modeling dynamic controls on ice streams: a Bayesian statistical approach. *Journal of Glaciology*, 54(1):705–714, 2008.

R. Bindschadler, W. D. Harrison, C. F. Raymond, and R. Crosson. Geometry and dynamics of a surge-type glacier. *J. Glaciol.*, 18:181194, 1977.

Richard Bintanja, Roderik S W van de Wal, and Johannes Oerlemans. A new method to estimate ice age temperatures. *Clim Dyn*, 24(2-3):197–211, December 2004.

Richard Bintanja, Roderik S W van de Wal, and Johannes Oerlemans. Modelled atmospheric temperatures and global sea levels over the past million years. *Nature*, 437 (7055):125–128, September 2005.

Craig H. Bishop, Brian J. Etherton, and Sharanya J. Majumdar. Adaptive sampling with the ensemble transform kalman filter. part i: Theoretical aspects. *Monthly Weather Review*, 129:420–436, 2001.

Marc Bocquet. Ensemble kalman filtering without the intrinsic need for inflation. *Nonlinear Processes in Geophysics*, 18(5):735–750, 2011.

Bertrand Bonan. *Assimilation de données pour l'initialisation et l'estimation de paramètres d'un modèle d'évolution de calotte polaire*. PhD thesis, Université de Grenoble, 2013. en préparation.

Pierre Brasseur, P Bahurel, L Bertino, F Birol, J-M Brankart, N Ferry, S Losa, Elisabeth Rémy, Jens Schröter, Sergey Skachko, et al. Data assimilation for marine monitoring and prediction: The mercator operational assimilation systems and the mersea developments. *Quarterly Journal of the Royal Meteorological Society*, 131(613):3561–3582, 2005.

D. Buiron, J. Chappellaz, B. Stenni, M. Frezzotti, M. Baumgartner, E. Capron, A. Landais, Bénédicte Lemieux-Dudon, V. Masson-Delmotte, M. Montagnat, F. Parrenin, and A. Schilt. TALDICE-1 age scale of the Talos Dome deep ice core, East Antarctica. *Climate of the Past*, 7(1):1–16, January 2011. doi: 10.5194/cp-7-1-2011. URL `http://hal-insu.archives-ouvertes.fr/insu-00649642`.

Gerrit Burgers, Peter Jan van Leeuwen, and Geir Evensen. Analysis scheme in the ensemble Kalman filter. *Monthly Weather Review*, 126:1719–1724, 1998.

Emmanuel Candes, Laurent Demanet, David Donoho, and Lexing Ying. Fast discrete curvelet transforms. *Multiscale Modeling & Simulation*, 5(3):861–899, 2006.

Emmanuel J Candes and David L Donoho. Curvelets: A surprisingly effective nonadaptive representation for objects with edges. Technical report, DTIC Document, 2000.

S Chaabane and M Jaoua. Identification of Robin coefficients by the means of boundary measurements. *Inverse Problems*, 15:1425, 1999.

Y. Chang, D. Hammond, A.C. Haza, P. Hogan, H.S. Huntley, A.D. Kirwan Jr., B.L. Lipphardt Jr., V. Taillandier, A. Griffa, and T.M. Özgökmen. Enhanced estimation of sonobuoy trajectories by velocity reconstruction with near-surface drifters. *Ocean Modelling*, (36):179–197, 2011.

T. Corpetti, E. Mmin, and P. Prez. Dense motion analysis in uid imagery. page 676691, 2002.

E. Cosme, J.-M. Brankart, J. Verron, P. Brasseur, and M. Krysta. Implementation of a reduced-rank, square-root smoother for ocean data assimilation. *Ocean Modelling*, (33): 87–100, 2010.

K. M. Cuffey and W. S. B. Paterson. *The physics of glaciers*. Butterworth-Heinemann, 2010.

N. Daget. Interpolation d'une grille orca2 vers une grille régulière. Technical Report TR/CMGC/06/18, CERFACS, 2006.

Basile de Fleurian. *Développement d'un modèle d'hydrologie sous-glaciaire dédié à la simulation du glissement basal des glaciers*. PhD thesis, Université de Grenoble, November 2010.

P. Duval. Creep and recrystallization of polycrystalline ice. *Bulletin de Minéralogie*, 102 (2-3):80–85, 1979.

Geir Evensen. Sequential data assimilation with a nonlinear quasi-geostrophic model using monte carlo methods to forecast error statistics. *Journal of Geophysical Research*, 99: 10143–10162, 1994.

V. Favier, C. Agosta, S. Parouty, G. Durand, G. Delaygue, H. Gallée, A.-S. Drouet, A. Trouvilliez, and G. Krinner. An updated and quality controlled surface mass balance dataset for antarctica. *The Cryosphere*, 7(2):583–597, 2013. doi: 10.5194/tc-7-583-2013. URL `http://www.the-cryosphere.net/7/583/2013/`.

M A Freitag, Nancy K Nichols, and C J Budd. Resolution of sharp fronts in the presence of model error in variational data assimilation. *Quarterly Journal of the Royal Meteorological Society*, pages n/a–n/a, August 2012.

P Fretwell, H D Pritchard, D J Vaughan, J L Bamber, N E Barrand, R Bell, C Bianchi, R G Bingham, D D Blankenship, G Casassa, G Catania, D Callens, H Conway, AJ Cook, H F J Corr, D Damaske, V Damm, F Ferraccioli, R Forsberg, S Fujita, Y Gim, P Gogineni, JA Griggs, R C A Hindmarsh, P Holmlund, J W Holt, R W Jacobel, A Jenkins, W Jokat, T Jordan, E C King, J Kohler, W Krabill, M Riger-Kust, K A Langley, G Leitchenkov, C Leuschen, B P Luyendyk, K Matsuoka, J Mouginot, N O Nitsche, Y Nogi, O A Nost, S V Popov, E Rignot, D M Rippin, A Rivera, J Roberts, N Ross, M J Siegert, A M Smith, D Steinhage, M Studinger, B Sun, B K Tinto, B C Welch, D Wilson, D A Young, C Xiangbin, and A Zirizzotti. Bedmap2: improved ice bed, surface and thickness datasets for Antarctica. *The Cryosphere*, 7:375–393, 2013.

P. Frey and F. Alauzet. Anisotropic mesh adaptation for CFD computations. *Comput. Method Appl. M.*, 194:5068–5082, 2005.

M. Frezzotti, C. Scarchilli, S. Becagli, M. Proposito, and S. Urbini. A synthesis of the antarctic surface mass balance during the last 800 yr. *The Cryosphere*, 7(1):303–319, 2013. doi: 10.5194/tc-7-303-2013. URL `http://www.the-cryosphere.net/7/303/2013/`.

O. Gagliardini and T. Zwinger. The ismip-hom benchmark experiments performed using the finite-element code elmer. *The Crysophere*, 2008.

O. Gagliardini, D. Cohen, P. Raback, and T. Zwinger. Finite-element modeling of subglacial cavities and related friction law. *Journal of Geophysical Research (Earth Surface)*, 2007.

O. Gagliardini, T. Zwinger, F. Gillet-Chaulet, G. Durand, L. Favier, B. de Fleurian, R. Greve, M. Malinen, C. Martín, P. Råback, J. Ruokolainen, M. Sacchettini, M. Schäfer, H. Seddik, and J. Thies. Capabilities and performance of elmer/ice, a new-generation ice sheet model. *Geoscientific Model Development*, 6(4):1299–1318, 2013. doi: 10.5194/gmd-6-1299-2013. URL `http://www.geosci-model-dev.net/6/1299/2013/`.

Hubert Gallée, Cécile Agosta, Luc Gential, Vincent Favier, and Gerhard Krinner. A downscaling approach toward high-resolution surface mass balance over antarctica. *Surveys in Geophysics*, 32(4-5):507–518, 2011. ISSN 0169-3298. doi: 10.1007/s10712-011-9125-3. URL `http://dx.doi.org/10.1007/s10712-011-9125-3`.

R. Giering and T. Kaminski. Recipes for adjoint code construction. *ACM Transactions on Mathematical Software (TOMS)*, 24(4):437–474, 1998.

Jean Charles Gilbert and Claude Lemaréchal. Some numerical experiments with variable-storage quasi-Newton algorithms. *Math. Programming*, 45(3, (Ser. B)):407–435, 1989. ISSN 0025-5610.

R. Greve. Application of a polythermal three-dimensional ice sheet model to the greenland ice sheet: response to steady-state and transient climate scenarios. *J. Climate*, 10:901–918, 1997.

Andreas Griewank and Andrea Walther. *Evaluating derivatives: principles and techniques of algorithmic differentiation*. Siam, 2008.

J A Griggs and J L Bamber. A new 1 km digital elevation model of antarctica derived from combined radar and laser data-part 2: Validation and error estimates. *The Cryosphere*, 3:113–123, 2009.

Thomas M Hamill, Jeffrey S Whitaker, and Chris Snyder. Distance-dependent filtering of background error covariance estimates in an ensemble kalman filter. *Monthly Weather Review*, 129(11):2776–2790, 2001.

E Hanna, FJ Navarro, F Pattyn, CM Domingues, X Fettweis, ER Ivins, RJ Nicholls, C Ritz, B Smith, S Tulaczyk, PL Whitehouse, and HJ Zwally. Ice-sheet mass balance and climate change. *Nature*, 2013.

L. Hascoët and V. Pascual. The Tapenade Automatic Differentiation tool: Principles, Model, and Specification. *ACM Transactions On Mathematical Software*, 39(3), 2013. URL `http://dx.doi.org/10.1145/2450153.2450158`.

Laurent Hascoet and Valérie Pascual. The Tapenade Automatic Differentiation tool: principles, model, and specification. *ACM Transactions on Mathematical Software (TOMS)*, 39(3):20, 2013.

Patrick Heimbach and Véronique Bugnion. Greenland ice-sheet volume sensitivity to basal, surface and initial conditions derived from an adjoint model. *Annals of Glaciology*, 50: 67–80, October 2009.

Isabelle Herlin, Etienne Huot, Jean-Paul Berroir, François-Xavier Le Dimet, and Gennady Korotaev. Estimation of a motion field on satellite images from a simplified ocean circulation model. In *Image Processing, 2006 IEEE International Conference on*, pages 1077–1080. IEEE, 2006.

B. Horn and B. Schunck. Determining optical flow. *Artificial Intelligence*, 17:185203, 1981.

Peter L Houtekamer and Herschel L Mitchell. A sequential ensemble kalman filter for atmospheric data assimilation. *Monthly Weather Review*, 129(1):123–137, 2001.

Ian M Howat, Ian Joughin, and Ted A Scambos. Rapid changes in ice discharge from greenland outlet glaciers. *Science*, 315(5818):1559–1561, 2007.

Brian R. Hunt, Eric J. Kostelich, and Istvan Szunyogh. Efficient data assimilation for spatiotemporal chaos: A local ensemble transform Kalman filter. *Physica D*, 230:112 – 126, 2007.

Etienne Huot, Isabelle Herlin, Nicolas Mercier, and Evgeny Plotnikov. Estimating apparent motion on satellite acquisitions with a physical dynamic model. In *International Conference on Pattern Recognition (ICPR'10)*, volume 1, pages 41–44, 2010.

Kolumban Hutter. *Theoretical Glaciology: Mathematical Approaches to Geophysics*. D. Reidel, 1983.

K. Ide, L. Kuznetsov, and C.K.R.T. Jones. Lagrangian data assimilation for a point-vortex system. *J. Turbulence*, 3(53), 2002.

Ian Joughin, Ben E Smith, Ian M Howat, Ted Scambos, and Twila Moon. Greenland flow variability from ice-sheet-wide velocity mapping. *Journal of Glaciology*, 56(197): 415–430, 2010.

Barclay Kamb, C F Raymond, W D Harrison, Hermann Engelhardt, K A Echelmeyer, N Humphrey, M M Brugman, and T Pfeffer. Glacier surge mechanism: 1982–1983 surge of Variegated Glacier, Alaska. *Science*, 227(4686):469–479, 1985.

L. Kuznetsov, K. Ide, and C.K.R.T. Jones. A method for assimilation of lagrangian data. *Monthly Weather Review*, 131:2247–2260, 2003.

F.-X. Le Dimet. A general formalism of variational analysis. Technical Report 73091 22, CIMMS, Norman, Oklahoma, 1982.

F.-X. Le Dimet and O. Talagrand. Variational algorithms for analysis and assimilation of meteorological observations: theoretical aspects. *Tellus Series A*, 38:97–+, 1986.

Bénédicte Lemieux-Dudon, Frédéric Parrenin, and Eric Blayo. A probabilistic method to construct a common and optimal chronology for an ice core. In Kaori Kidahashi, editor, *Physics of Ice Core Records*. Hokkaido University Collection of Scholarly and Academic Papers, 2008. URL `http://hal.inria.fr/inria-00344659`.

Bénédicte Lemieux-Dudon, Eric Blayo, Jean-Robert Petit, Claire Waelbroeck, Anders Svensson, Catherine Ritz, Jean-Marc Barnola, Bianca Maria Narcisi, and Frédéric Parrenin. Consistent dating for Antarctic and Greenland ice cores. *Quaternary Science Reviews*, 29(1-2):8–20, January 2010. doi: 10.1016/J.QUASCIREV.2009.11.010. URL `http://hal-insu.archives-ouvertes.fr/insu-00562239`.

J. T. M. Lenaerts, M. R. van den Broeke, W. J. van de Berg, E. van Meijgaard, and P. Kuipers Munneke. A new, high-resolution surface mass balance map of antarctica (19792010) based on regional atmospheric climate modeling. *Geophysical Research Letters*, 39(4):n/a–n/a, 2012. ISSN 1944-8007. doi: 10.1029/2011GL050713. URL `http://dx.doi.org/10.1029/2011GL050713`.

J.-L. Lions. *Contrôle optimal de systèmes gouvernés par des équations aux dérivées partielles*. Dunod, Paris, 1968.

Louis Lliboutry. Anisotropic, transversely isotropic nonlinear viscosity of rock ice and rheological parameters inferred from homogenization. *International journal of plasticity*, 9(5):619–632, 1993.

D. R. MacAyeal. The basal stress distribution of ice stream e, antarctica, inferred by control methods. *Journal of Geophysical Research*, 1992.

D. R. MacAyeal. A tutorial on the use of control methods in ice-sheet modeling. *Journal of Glaciology*, 1993.

G. Madec. *NEMO ocean engine*. Note du Pole de modélisation, Institut Pierre-Simon Laplace (IPSL), France, no 27 issn no 1288-1619 edition, 2008.

Gurvan Madec, Pascale Delecluse, Maurice Imbard, and Claire Lévy. OPA 8.1 ocean general circulation model reference manual. *Note du Pôle de modélisation, Institut Pierre-Simon Laplace*, 11, 1998.

S. Mallat. *A wavelet tour of signal processing*. Academic Press, 1998.

Y Michel and F Bouttier. Automated tracking of dry intrusions on satellite water vapour imagery and model output. *Quarterly Journal of the Royal Meteorological Society*, 132 (620):2257–2276, October 2006.

Yann Michel. Displacing Potential Vorticity Structures by the Assimilation of Pseudo-Observations. *Monthly Weather Review*, 139(2):549–565, August 2011.

K Mogensen, MA Balmaseda, AT Weaver, M Martin, and A Vidard. Nemovar: A variational data assimilation system for the nemo ocean model. *ECMWF newsletter*, 120: 17–22, 2009.

A. Molcard, A.C. Poje, and T.M. Özgökmen. Directed drifter launch strategies for lagrangian data assimilation using hyperbolic trajectories. *Ocean Modelling*, 12:268–289, 2006.

M. Morlighem, E. Rignot, H. Seroussi, E. Larour, H. Ben Dhia, and D. Aubry. Spatial patterns of basal drag inferred using control methods from a full-stokes and simpler models for pine island glacier, west antarctica. *Geophysical Research Letters*, 2010.

J. Nilsson, S. Dobricic, N. Pinardi, V. Taillandier, and P.M. Poulain. On the assessment of argo float trajectory assimilation in the mediterranean forecasting system. *Ocean Dynamics*, (preprint), 2011.

J. Nocedal and S.J. Wright. *Numerical optimization*. Springer Verlag, 1999.

Edward Ott, Brian R Hunt, Istvan Szunyogh, Aleksey V Zimin, Eric J Kostelich, Matteo Corazza, Eugenia Kalnay, DJ Patil, and James A Yorke. A local ensemble kalman filter for atmospheric data assimilation. *Tellus A*, 56(5):415–428, 2004.

T.M. Özgökmen, A. Griffa, L. I. Piterbarg, and A. J. Mariano. On the predictability of the lagrangian trajectories in the ocean. *J. Atmos. Ocean. Tech.*, 17(3):366–383, 2000.

Didier Paillard and Frédéric Parrenin. The Antarctic ice sheet and the triggering of deglaciations. *Earth and Planetary Science Letters*, 227(3-4):263–271, November 2004.

N. Papadakis and É. Mémin. A variational method for the tracking of curve and motion. *Journal of Mathematical Imaging and Vision*, 31(1):81–103, 2008.

V Peyaud. *Role de la dynamique des calottes glaciaires dans les grands changements climatiques des periodes glaciaires-interglaciaires*. PhD thesis, Université Joseph-Fourier-Grenoble I, October 2006.

Dinh-Tuan Pham. A singular evolutive interpolated Kalman filter for data assimilation in oceanography. Technical report 163, IMAG-LMC, September 1996.

Dinh-Tuan Pham. Stochastic methods for sequential data assimilation in strongly nonlinear systems. *Mon. Weather Rev.*, 129(5):1194–1207, May 2001.

Dinh-Tuan Pham, Jacques Verron, and Marie-Christine Roubaud. A singular evolutive extended Kalman filter for data assimilation in oceanography. Technical report 162, IMAG-LMC, September 1996.

Dinh-Tuan Pham, Jacques Verron, and Lionel Gourdeau. Filtres de Kalman singuliers évolutif pour l'assimilation de données en océnographie. *C. R. Acad. Sci., Paris, Sci. terre planètes*, 326(4):255–260, February 1998.

H. D. Pritchard, R. J. Arthern, D. G. Vaughan, and L. A. Edwards. Extensive dynamic thinning on the margins of the greenland and antarctic ice sheets. *Nature*, 461:971–975, 2009.

M. E. Raymo. The timing of major climate terminations. *Paleoceanography*, 12(4):577–585, 1997.

C. F. Raymond. How do glaciers surge? a review. *J. Geophys. Res.*, 92:91219134, 1987.

C. F. Raymond and W. D. Harrison. Evolution of variegated glacier, alaska, usa, prior to its surge. *J. Glaciol.*, 34:154–169, 1988.

Mélanie Raymond-Pralong and G H Gudmundsson. Bayesian estimation of basal conditions on Rutford Ice Stream, West Antarctica, from surface data. *Jounral of Glaciology*, 57(202), 2011.

E Rignot, J Mouginot, and B Scheuchl. Ice flow of the antarctic ice sheet. *Science*, 333 (6048):1427–1430, 2011.

C. Ritz, V. Rommelaere, and C. Dumas. Modeling the evolution of Antarctic ice sheet over the last 420, 000 years- Implications for altitude changes in the Vostok region. *Journal of Geophysical Research*, 106:31, 2001.

Catherine Ritz. *Un modèle thermo-mécanique d'évolution pour le bassin glaciaire Antarctique Vostok-Glacier Byrd : Sensibilité aux valeurs des paramètres mal connus.* PhD thesis, Université Joseph Fourier, 1992.

V. Rommelaere and D. R. MacAyeal. Large-scale rheology of the ross ice shelf, antarctica, computed by a control method. *Annals of Glaciology*, 1997.

Vincent Rommelaere. *Trois Problemes Inverses En Glaciologie.* PhD thesis, Université Joseph-Fourier-Grenoble I, 1997.

H. Salman, L. Kuznetsov, C.K.R.T. Jones, and K. Ide. A method for assimilating lagrangian data into shallow-water equation ocean model. *Mon. Weather Rev.*, 134:1081–1101, 2006.

Johannes Schmetz, Kenneth Holmlund, Joel Hoffman, Bernard Strauss, Brian Mason, Volker Gaertner, Arno Koch, and Leo Van De Berg. Operational cloud-motion winds from Meteosat infrared images. *Journal of Applied Meteorology*, 32(7):1206–1225, 1993.

Christian Schoof and R C A Hindmarsh. Thin-Film Flows with Wall Slip: An Asymptotic Analysis of Higher Order Glacier Flow Models. *The Quarterly Journal of Mechanics and Applied Mathematics*, 63(1):73–114, January 2010.

H. Seddik, R. Greve, T. Zwinger, F. Gillet-Chaulet, and O. Gagliardini. Simulations of the greenland ice sheet 100 years into the future with the full stokes model Elmer/Ice. *J. Glaciol.*, 58(427–440), 2012.

Julio Sheinbaum and David LT Anderson. Variational assimilation of xbt data. ii, sensitivity studies and use of smoothing constraints. *Journal of physical oceanography*, 20 (5):689–704, 1990.

I Souopgui. *Assimilation d'images pour les fluides géophysiques*. PhD thesis, Université de Grenoble, 2010.

V. Taillandier, A. Griffa, and A. Molcard. A variational approach for the reconstruction of regional scale eulerian velocity fields from lagrangian data. *Ocean Modelling*, (13): 1–24, 2006.

V. Taillandier, A. Griffa, P.M. Poulain, R. Signell, J. Chiggiato, and S. Carniel. On the assessment of argo float trajectory assimilation in the mediterranean forecasting system. *Journal of Geophysical Research*, (113), 2008.

Tapenade. *http://www-sop.inria.fr/tropics/tapenade.html*, 2002.

W. C. Thacker and R. B. Long. Fitting dynamics to data. *J. Geosphys. Res.*, 93:1227–1240, 1988.

Claire Thomas, Thomas Corpetti, and Étienne Memin. Data Assimilation for Convective-Cell Tracking on Meteorological Image Sequences. *IEEE Transactions on Geoscience and Remote Sensing*, 48(8):3162–3177, 2010.

O. Titaud, A. Vidard, I. Souopgui, and F-X. Le Dimet. Assimilation of image sequences in numerical models. *Tellus Series A: Dynamic Meteorology and Oceanography*, 62(1): 30–47, 2010.

O. Titaud, J-M. Brankart, and J. Verron. On the use of finite-time lyapunov exponents and vectors for direct assimilation of tracer images into ocean models. *Tellus Series A: Dynamic Meteorology and Oceanography*, 63(5):1038–1051, 2011.

WJJ van Pelt, Johannes Oerlemans, and C H Reijmer. An iterative inverse method to estimate basal topography and initialize ice flow models. *The Cryosphere*, 2013.

A Vidard, Eric Blayo, Francois-Xavier Le Dimet, and Andrea Piacentini. 4D variational data analysis with imperfect model. *Flow, Turbulence and Combustion*, 65(3-4):489–504, 2000.

A Vidard, Andrea Piacentini, and Francois-Xavier Le Dimet. Variational data analysis with control of the forecast bias. *Tellus A*, 56(3):177–188, 2004.

Arthur Vidard. Assimilation de données et méthodes adjointes pour la géophysique. Habilitation à diriger des recherches, Université Joseph-Fourier-Grenoble I, July 2012.

Arthur Vidard, Franck Vigilant, Charles Deltel, and Rachid Benshila. Nemovar: Short and long term development strategies. Technical report, ANR VODA deliverables, 2010.

Arthur Vidard, Franck Vigilant, Charles Deltel, and Rachid Benshila. Nemo tangent and adjoint models reference manual and users guide. Technical report, ANR VODA deliverables, 2012.

A. Vieli and A. J. Payne. Application of control methods for modelling the flow of pine island glacier, west antarctica. *Annals of Glaciology*, 2003.

A. Weaver and P. Courtier. Correlation modelling on the sphere using a generalized diffusion equation. *Quarterly Journal of the Royal Meteorological Society*, 127:1815–1846, July 2001.

2

Methods for inverse problems and sensitivity analysis

Contents

2.1 Model reduction

In this section, we present the problems of model reduction that have been studied with C. Prieur, in the framework of the PhD thesis of A. Janon whom we co-advised. To begin with, we present the principles of reduced basis and certified error bounds. Then the published and submitted papers [10] [21] are summarised.

2.1.1 Presentation

The idea of model reduction is as follows. Suppose we want to solve a system of partial differential equations with a computer. After discretization, it is reduced to a very large finite dimensional system (possibly nonlinear), whose size is the number of grid points, the number of finite element functions, the number of cells of finite volume, etc. Then there are various reasons for wanting to avoid computing in large dimension: we may want to calculate very quickly the solution (real-time applications), or want to perform a large number of calculations (Monte Carlo iterative optimization, etc.). Model reduction then is to seek the solution as a linear combination of a small number of independent vectors. The unknowns of the system are then the small number of coefficients and the size of the workspace is reduced.

Framework

The framework is that of parameterised partial differential equations (PDE). For example we will see later an application to the viscous Burgers equation, in which the parameters are the viscosity and the boundary conditions. We will also consider the benchmark problem of Venturi, in which the geometry of the domain plays the role of parameters. Thus, the system can be written as an input / output model:

$$\mu \mapsto u(\mu) \mapsto s(\mu) = s(u(\mu))$$

where $\mu \in \mathbb{R}^p$ is the parameters vector, u the solution of the PDE system, and s the output, which is a function of u (ie the mean, the trace on a boundary, etc.). The classical framework of model reduction (see Prud'homme et al. (2002); Veroy et al. (2003); Prud'homme and Patera (2004); Cuong et al. (2005); Grepl et al. (2007)) involves a linear PDE with the following variational formulation:

$$a(u(\mu), v; \mu) = l(v; \mu), \quad \forall v \in H, \text{ for every parameter } \mu \tag{2.1}$$

with $u(\mu) \in H$ a Hilbert space of dimension $\mathcal{N}$ of finite element, $a(.,.;\mu)$ a bilinear form on H and $l(.;\mu)$ a linear form. The linearity of the PDE is assumed here to simplify the presentation, but we can see in Grepl and Patera (2005); Urban and Patera (2012); Knezevic et al. (2010); Veroy and Patera (2005) and [10] applications to nonlinear PDEs. Then we will supose (for readability), that a and l depend on μ in the so-called affine form as follows:

$$a(.,.;\mu) = \sum_{q=1}^{Q} \theta_q(\mu) a_q(.,.), \quad l(.;\mu) = \sum_{q'=1}^{Q'} \gamma_{q'}(\mu) l_{q'}(.), \quad \forall \mu$$

where Q and Q' are integers, θ_q and $\gamma_{q'}$ are real function and a_q and $l_{q'}$ are bilinear and linear forms which do not depend on μ. In the nonlinear case, the method of the *magic*

points (empirical interpolation, Grepl et al. (2007)) allows to reduce any formulation to an approximate affine form.

Finally, we assume that a is coercive, when μ is fixed:

$$\forall \mu, \quad \exists \alpha(\mu) > 0, \quad a(u, v; \mu) \geq \alpha(\mu)\|u\|\|v\|, \quad \forall u, v \in H$$

Reduced system

In the previous framework (finite element), the solution u can be decomposed in a basis $\phi_1, ..., \phi_{\mathcal{N}}$ of H, where $\mathcal{N}$ is large:

$$u(\mu) = \sum_{i=1}^{\mathcal{N}} u_i(\mu)\phi_i$$

We now seek an approximation of u in small dimension n :

$$\tilde{u}(\mu) = \sum_{i=1}^{n} \tilde{u}_i(\mu)\zeta_i$$

where $(\zeta_1, ..., \zeta_n)$ is a linearly independant family of H (independent of μ) called the *reduced basis*. The reduced space spanned by ζ_i, Vect $(\zeta_1, ..., \zeta_n)$, is denoted $\tilde{H}$.. We then seek $\tilde{u}$ as the solution of the variational problem in $\tilde{H}$:

$$a(\tilde{u}(\mu), v; \mu) = l(v; \mu), \forall v \in \tilde{H}$$

which is equivalent to

$$\sum_{i=1}^{n} \tilde{u}_i \sum_{q=1}^{Q} \theta_q(\mu)\, a_q(\zeta_i, \zeta_j) = \sum_{q'=1}^{Q'} \gamma_{q'}(\mu)\, l_{q'}(\zeta_j), \quad \forall 1 \leq j \leq n$$

This formulation can highlight the online / offline structure of the method:

- Offline: after choosing the basis, the numbers independent of μ are calculated and stored: $a_q(\zeta_i, \zeta_j)$ and $l_{q'}(\zeta_j)$ for all i, j. This can be expensive, since its complexity depends on $\mathcal{N}$, but is done only once.
- Online: for each desired value of the parameter μ, we calculate $\theta_q(\mu)$ and $\gamma_{q'}(\mu)$, and (thanks to the items stored in the online step) a system is formed (of size n) for $\tilde{u}_i$ and solved. The complexity of this phase is independent of $\mathcal{N}$.

Assuming the problem and the choice of the basis allow $n << \mathcal{N}$ while having $\tilde{u}$ close to u, we thus gain in computation time, provided that we can ignore the cost of the offline phase, which is the case if one makes many calculations or works in real time.

A posteriori error bound

The great advantage of the reduction method proposed by Prud'homme et al. (2002); Veroy et al. (2003); Prud'homme and Patera (2004); Cuong et al. (2005); Grepl et al. (2007) is to provide an error bound that is certified and computable online (that is to say with a complexity independent of $\mathcal{N}$) :

$$\|u(\mu) - \tilde{u}(\mu)\| \leq \varepsilon(\mu), \quad \forall \mu$$

In the case where the bilinear form $a(.,.;\mu)$ is symmetric, the bound can be written as:

$$\varepsilon(\mu) = \frac{\rho(\mu)}{\alpha(\mu)} \tag{2.2}$$

where $\rho(\mu)$ is the dual norm of the residual $r(.;\mu)$:

$$\rho(\mu) = \sup_{v\in H, \|v\|=1} |r(v;\mu)|, \quad r(v;\mu) = a(\tilde{u}(\mu), v;\mu) - l(v;\mu)$$

The whole point of the method is obviously that we can implement a offline / online procedure to compute an upper bound of the error, so as to produce a certified approximation $\tilde{u}(\mu)$ (certification without impacting too much the computation time). We refer to Nguyen et al. (2005); Huynh et al. (2007a); Chen et al. (2009) for details of this implementation.

Choice of the reduced basis

Everything we have seen so far can be implemented with any reduced basis (ie any linearly independant family $\zeta_1, ..., \zeta_n$ of H). The next question is of course to find a good basis, that is to say, a basis that ensures small a posteriori error. We review below quickly the various options available in the literature.

Proper orthogonal decomposition (POD). POD has different names depending on the area where it is used (principal component analysis PCA, empirical orthogonal functions EOF, singular value decomposition SVD, Karhunen-Loeve, etc.).

The idea is to find the POD basis $\mathcal{B}$ as the orthonormal basis of size n that minimizes the mean square error projection on this basis $\Pi_{\mathcal{B}}$, averaged over the parameters μ:

$$\mathcal{B} = \underset{b \text{ orthonormal basis of size } n}{\operatorname{argmin}} \int \|u(\mu) - \Pi_b(u(\mu))\|^2 \, d\mu$$

where it was assumed that the parameters μ are distributed according to the probability density function of $d\mu$. In practice, we compute an approximation of the basis $\mathcal{B}$ by the snapshots method, ie we evaluate the above integral by Monte Carlo using a (large) sample M of the law of μ:

$$\mathcal{B} \simeq \underset{b \text{ orthonormal basis of size } n}{\operatorname{argmin}} \sum_{\mu\in M} \|u(\mu) - \Pi_b(u(\mu))\|^2$$

This is done by computing the singular value decomposition of the snapshots matrix. First we form the matrix A by placing in its columns the centered snapshots:

$$A = [u(\mu_1) - \bar{u}; ...; u(\mu_2) - \bar{u}], \quad \bar{u} = \frac{1}{m}\sum_{i=1}^{m} u(\mu_i), \quad M = \{\mu_i, i = 1..m\}$$

then the singular value decomposition of A is carried out:

$$A = U\Sigma V^T$$

where Σ is the diagonal matrix of singular values (listed in decreasing order). The desired $\mathcal{B}$ basis is then formed with the first n columns of V, which are then normalised.

Greedy algorithm. The *greedy* method (see Nguyen et al. (2005); Buffa et al. (2009)) is to iteratively build the basis so that the reduction error bound is smallest as possible. We begin, as before, by choosing a (large) sample M following the probability distribution of μ. Then the basis $\mathcal{B}$ is initialized by taking

$$\mathcal{B} = \{u(\mu_0)\}, \quad \mu_0 \text{ randomly chosen according to the pdf of } \mu$$

and then we iterate the following two steps:

1. calculate $\mu_j = \text{argmax}_{\mu \in M} \varepsilon(\mu)$, where the error bound ε is calculated with the current basis $\mathcal{B}$;
2. update the basis $\mathcal{B}$: add the vector $u(\mu_j)$ and orthonormalise.

Goal-oriented basis. The idea this time is to choose a basis which would no longer minimize the error on the state $\varepsilon(\mu)$, but the on the output $\|s(u(\mu)) - s(\tilde{u}(\mu))\|$. This problem is solved as an optimal control problem in Bui-Thanh et al. (2007) for linear dynamic systems, but the method is very costly to implement in practice.

2.1.2 Certified error bound for the viscous Burger's equation

This paragraph summarizes the results contained in section [10], written in collaboration with C. Prieur and A. Janon, as part of his thesis.

Model and problem presentation

The starting point of this work is to study the implementation of the reduced basis method presented above for a "toy" model of geophysical flow equation, namely the viscous Burgers equation. The question that will arise later will be the sensitivity of the equation to some of its input parameters. As to answer this we will implement a Monte Carlo, we will need to calculate many solutions (associated with various sets of parameters), hence the need for a reliable and inexpensive reduced model.

The problem we consider is the following. Let u be a function of the space $x \in [0;1]$ and time $t \in [0;T]$ (with $T > 0$), smooth enough: $u \in C^1\left([0,T], H^1(]0,1[)\right)$, satisfying the viscous Burgers equation:

$$\frac{\partial u}{\partial t} + \frac{1}{2}\frac{\partial}{\partial x}(u^2) - \nu \frac{\partial^2 u}{\partial x^2} = f \tag{2.3}$$

where $\nu \in \mathbb{R}_*^+$ is the viscosity and $f \in C^0\left([0,T], L^2(]0,1[)\right)$ is the source term. Of course the initial and boundary conditions are added:

$$u(t=0,x) = u_0(x) \ \ \forall x \in [0;1] \tag{2.4}$$

with $u_0 \in H^1(]0,1[)$

$$\begin{cases} u(t, x=0) = b_0(t) \\ u(t, x=1) = b_1(t) \end{cases} \quad \forall t \in [0;T] \tag{2.5}$$

where $b_0, b_1 \in C^0([0,T])$ and u_0 satisfy the following compatibility condition:

$$u_0(0) = b_0(0) \quad \text{and} \quad u_0(1) = b_1(0)$$

The existence and uniqueness of the solution u is a classical result (Hopf, 1950).

The input parameters of this model are ν, u_0, b_0, b_1 and f. Indeed, in an extension to oceanography, these are the important parameters of the model (external forcings, boundary conditions, viscosity, initial conditions), they are generally poorly known.

With the exception of the viscosity, all are functional parameters. As our reduction strategies work with not too many scalar parameters, we choose to parameterize functions in suitable bases (that are not specified here, but which are supposed to be fairly regular, as the Fourier series for example):

$$b_0(t) = b_{0m} + \sum_{l=1}^{n(b_0)} A_l^{b_0} \Phi_l^{b_0}(t) \qquad b_1(t) = b_{1m} + \sum_{l=1}^{n(b_1)} A_l^{b_1} \Phi_l^{b_1}(t)$$

$$s(t,x) = f_m + \sum_{l=1}^{n_T(f)} \sum_{p=1}^{n_S(f)} A_{lp}^{f} \Phi_l^{fT}(t) \Phi_p^{fS}(x) \qquad u_0(x) = u_{0m} + \sum_{l=1}^{n(u_0)} A_l^{u_0} \Phi_l^{u_0}(x)$$

where the basic functions Φ^{b_0}, $\Phi_l^{b_1}$, Φ_l^{fT}, Φ_p^{fS} and $\Phi_l^{u_0}$ are fixed and the integers $n(b_0)$, $n(b_1)$, $n_T(f)$, $n_S(f)$ and $n(u_0)$ are given. Thus, our data set includes the following scalar variables:

$$\nu, b_{0m}, b_{1m}, f_m, u_{0m}$$

$$\left(A_l^{b_0}\right)_{l=1,\dots,n(b_0)}, \left(A_l^{b_1}\right)_{l=1,\dots,n(b_1)}, \left(A_{lp}^{f}\right)_{l=1,\dots,n_T(f);p=1,\dots,n_S(f)}, \left(A_l^{u_0}\right)_{l=1,\dots,n(u_0)}$$

with the compatibility condition:

$$b_{0m} = u_{0m} \quad \text{and} \quad b_{1m} = u_{0m} + \sum_{l=1}^{n(u_0)} A_l^{u_0} \Phi_l^{u_0}(x)$$

Methods

Discretisation and offline / online decomposition. In Nguyen et al. (2005) the authors study the problem by considering only one parameter, the viscosity. We adapted this method to take into account other parameters, but the principle is the same. The idea is to start from the continuous equation and discretise it into a linear system in dimension $\mathcal{N}$, for which we can implement the reduction method described above. The procedure follows Nguyen et al. (2005) (with the exception of step 2 we added):

1. Establishment of the weak formulation (2.3,2.4).
2. Penalisation of the boundary conditions in the weak formulation (2.5).
3. Discretization by finite elements P^1. The result is a system of ordinary differential equations in dimension system $\mathcal{N}$.
4. Discretization in time by backward Euler method. Thus, we get a non-linear system dimension $\mathcal{N}$.
5. Resolution by Newton's method. At each iteration, we must solve a linear system in dimension $\mathcal{N}$.

For a given reduced basis $\zeta_1, ..., \zeta_n$, we can implement on the last linear system an offline / online strategy, which allows to solve it with a complexity independent of $\mathcal{N}$. The overall complexity then depends on n, the number of iterations of Newton and the number of time steps. We refer to **[10]** for details.

Error bound. Detailed technical calculations in [10] allow to establish an error bound for the proposed reduction method. For this we proceed in two steps: first, a theorem giving an estimate of the error $e_k = u(t_k) - \tilde{u}(t_k)$ at each time t_k is established. Then, we propose a strategy to effectively estimate an upper bound of the error that is computable online. The main difficulty lies in the estimation of upper and lower bounds for the numbers C_k called *stability constants*:

$$C_k = \inf_{v \in H, \|v\|=1} 2c(\tilde{u}_k, v, v) + \nu a(v, v)$$

where c and a are the tri-and bi-linear forms associated with $\frac{1}{2}\partial_x(u^2)$ and $-\nu\partial_{xx}u$ in the variational formulation of equation (2.3). For this, the method of successive constraints (SCM) is used (Huynh et al., 2007b; Nguyen et al., 2009), and is detailed in [10].

Choice of the reduced basis. The article compares three basic choices: POD, Greedy, and hybrid. POD and Greedy were presented above.

The hybrid basis is a mix of POD and Greedy strategies proposed in Haasdonk and Ohlberger (2008). The algorithm for constructing the basis is as follows:

1. Choose an integer P.
2. Choose a (large) sample of parameters.
3. Choose a μ at random, and initialize the $\mathcal{B}$ basis with the orthonormalisation of the subspace spanned by $u(t_k, \mu)$, for all times t_k.
4. Iterate the following procedure:
   (a) Find the μ^* that maximizes (for all μ in the sample) the online error indicator, calculated with the current basis $\mathcal{B}$.
   (b) Calculate P first POD modes of the snapshots set $u(t_k, \mu^*)$, for every time step t_k.
   (c) Add these modes to the basis $\mathcal{B}$ (+ orthonormalisation).

To all these bases we added the initial condition, in order to have zero initial error.

Numerical results

First results. Results are presented for a first simplified test case, with only 7 active parameters with the POD basis. Figure 2.1 shows the error bound produced with 7 POD modes, as well as the actual error. This gives an error bound smaller than 1 for 1 000, with a reduction in computation time of 85% (including the calculation of the bound).

Bases comparison. Figure 2.2 compares the error bound obtained with the three proposed bases, as a function of the number of elements in each basis, for a simplified test case, with only one parameter (for the initial condition). The computation time fairly depends on the method (POD-Greedy < POD < Greedy), Greedy costing twice as much as POD-Greedy. The online computation time is the same. The three bases produce similar results, the POD-Greedy is slightly worse, while the POD is better in average error (in time) and the Greedy basis is better for the maximum error (in time).

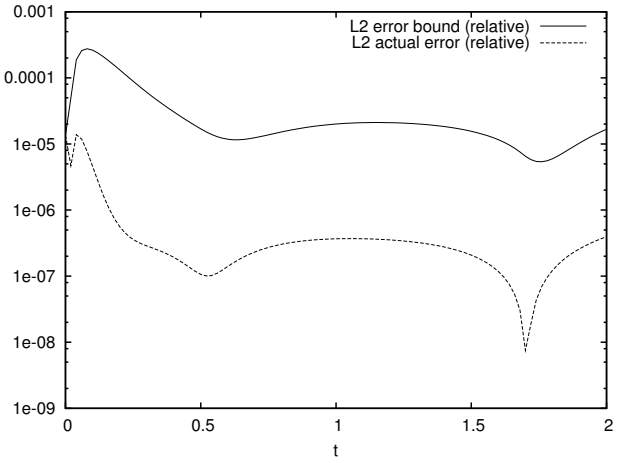

Figure 2.1: Relative errors for 7 parameters and a 7 member POD basis, as a function of time. Solid line represents the online relative bound $\epsilon_k / \left\|\widetilde{u}^k\right\|$, and dashed line $\left\|u^k - \widetilde{u}^k\right\| / \left\|\widetilde{u}^k\right\|$ represent the true error.

Comparison with the literature. Finally, Figure 2.3 shows the comparison with the existing bound (Nguyen et al., 2009). It shows the performance of our bound (calculated with the POD), which gains an order of magnitude. This can also be seen in the bound computation, as in the context of Nguyen et al. (2009), only the parameter ν is considered, which greatly simplifies the calculations. Indeed, the existing bound is:

$$\|e_k\| \leq \sqrt{\frac{\|e_{k-1}\|^2 + \frac{\Delta t}{\nu} \|r_k\|_0^2}{1 + \widetilde{C_k} \Delta t}}, \text{ with } \widetilde{C_k} = \inf_{v \in X_0} \frac{4c(\widetilde{u}^k, v, v) + \nu a(v, v)}{\|v\|^2}$$

while our bound is:

$$\|e_k\| \leq \frac{\|e_{k-1}\| + \Delta t \|r_k\|_0}{1 + C_k \Delta t}, \text{ with } C_k = \inf_{v \in X_0, \|v\|=1} \left[2c(\widetilde{u}^k, v, v) + \nu a(v, v)\right]$$

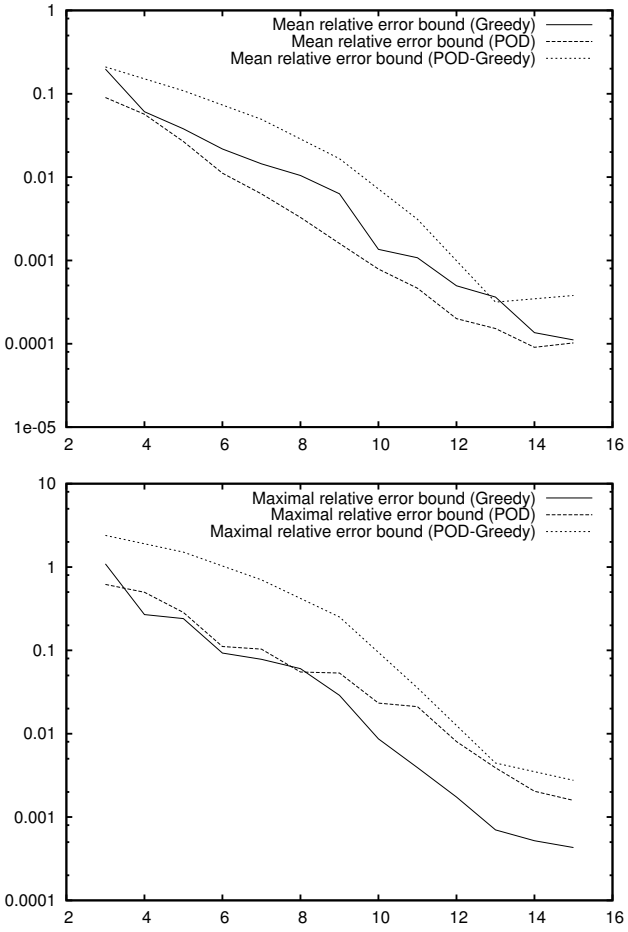

Figure 2.2: Comparison of POD, Greedy and POD-Greedy bases. We represent he mean (in time) error (top), the maximal error (bottom) as a function of the basis size. The size of the random sample of the parameter $u_{0m} \in [0, 1]$ is 100.

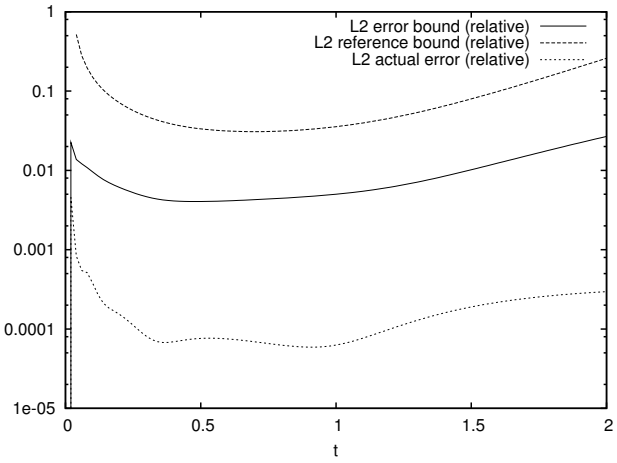

Figure 2.3: Comparison between the new bound, the bound proposed by Nguyen et al. (2009) (called reference) and the true error, as a function of time, for $\nu = 0.1$.

2.1.3 Goal-oriented error bound

This section summarizes the results contained in the submitted work [21], with C. Prieur and A. Janon, as part of his thesis.

Problem presentation

Presentation. The starting point of this work is the following: the previously proposed error bound is a bound on the solution u of the PDE. When the amount of interest (the output) is not u, but a function of u, we would like to offer a bound that is better, and adapted to the output. For example, suppose u is written in the reduced basis as $u = \sum_i u_i \phi_i$, but the output $s(u)$ only "see" some components of u, for example $s(u) = \sum_{i \text{ even}} s_i u_i \phi_i$. In this case the error bound terms associated with odd modes of u are useless. Therefore goal-oriented bound allows to either provide a more accurate result, or reduce the number of elements in the reduced basis (and thus the computation time).

Framework and notations. As before, we work in the framework of parameterised PDE, written in variational formulation and discretised by finite elements. The workspace is denoted X, its size is $\mathcal{N}$. Assume that in 2.1 a is positive definite bilinear and the second member l is linear, so that the equation leads to solve a linear system with parameters in X:

$$A(\mu)u(\mu) = l(\mu)$$

As before, we can choose a reduced basis and obtain an approximate solution by an adequate offline / online decomposition. We denote $\tilde{X}$ the reduced space (of dimension n), and Z the matrix (of size $\mathcal{N} \times n$) whose columns contain the reduced basis vectors. If we denote $\tilde{u}$ the components of the projection of u on $\tilde{X}$, we have

$$Z^T A Z \tilde{u} = Z^T l$$

It is also assumed that the output $s(\mu) = s(u(\mu))$ is a linear function of u, ie a linear form on X. For the chosen scalar product, this linear form admits a representative in X, denoted S (ie $s(u) = \langle S, u\rangle$). The reduced output is then defined

$$\tilde{s}(\mu) = \langle S, Z\tilde{u}(\mu)\rangle = \langle Z^T S, \tilde{u}(\mu)\rangle$$

and we denote also $\tilde{S} = Z^T S$.

The objective of this work is to produce an error bound on the output $\tilde{s}(\mu)$ calculated by model reduction compared to the actual output $s(\mu)$.

Past works. There are two goal-oriented bounds in the literature. The first is simply to use an existing bound for u and the linearity of the output:

$$|s(\mu) - \tilde{s}(\mu)| \leq \|S\| \, \|u(\mu) - Z\tilde{u}(\mu)\|$$

This is called the Lipschitz bound. It extends naturally to the case where the output is not linear but Lipschitz.

The second approach (Nguyen et al., 2005) is to use the solution of the adjoint problem to correct the output, and provide a (better) bound on the corrected output. The solution of the adjoint problem is written as follows (in the simplified case where A is symmetric):

$$A(\mu)u^a(\mu) = -S$$

As before we can implement a reduction method. We denote Z^a the matrix whose columns contain the reduced basis vectors, and $\tilde{u}^a$ the coordinates of the approximate solution reduced in this basis.
The corrected output is

$$s^a(\mu) = s(Z\tilde{u}(\mu)) + \langle r(\mu), Z^a\tilde{u}^a(\mu)\rangle$$

where $r(\mu) = A(\mu)Z\tilde{u}(\mu) - l(\mu)$ is the residual. And the associated error bound is

$$|s(\mu) - \tilde{s}(\mu)| \leq \frac{\rho(\mu)\rho^a(\mu)}{\alpha(\mu)}$$

where $\rho(\mu)$ is the dual norm of the residual $r(\mu)$, $\rho^a(\mu)$ the dual norm of the adjoint residual $r^a(\mu) = AZ^a\tilde{u}^a - S$ and $\alpha(\mu)$ is the coercivity constant of a.

Probabilistic error bound

The purpose of the work [21] is to propose a probabilistic error bound, depending on the level of risk $\beta \in]0, 1[$ as follows:

$$\mathbb{P}\Big(|s(\mu) - \tilde{s}(\mu)| \geq \varepsilon(\mu, \beta)\Big) \leq \beta$$

In other words, there is a risk β that the error is not smaller than the proposed bound.

We summarise the beginning of the proof below. We start with

$$A^{-1}r = Z\tilde{u} - A^{-1}l = Z\tilde{u} - u$$

Therefore

$$\tilde{s}(\mu) - s(\mu) = \langle S, Z\tilde{u} - u\rangle = \langle S, A^{-1}r\rangle = \langle A^{-T}S, r\rangle$$

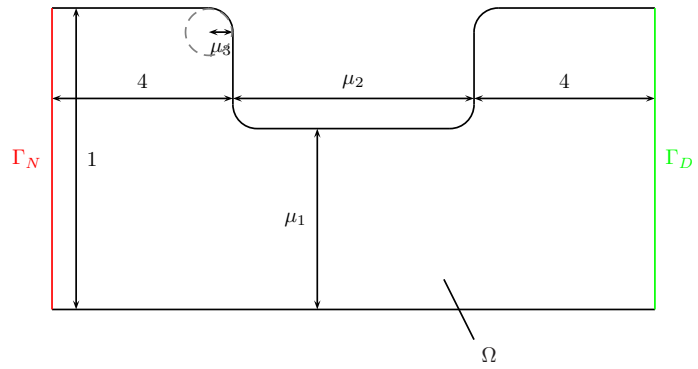

Figure 2.4: Domain $\Omega(\mu)$ for the Venturi problem.

The residual is decomposed in an orthonormal basis $\phi_1, ..., \phi_{\mathcal{N}}$ of X:

$$r(\mu) = \sum_{i=1}^{\mathcal{N}} r_i(\mu)\phi_i$$

so that we can write

$$\tilde{s}(\mu) - s(\mu) = \sum_{i=1}^{\mathcal{N}} r_i(\mu)\langle A^{-T}S, \phi_i\rangle$$

The idea of the probabilistic error bound is then to split the sum in two parts, and to bound them using a suitable choice of the basis $(\phi_i)_{1\leq i\leq \mathcal{N}}$.

This work extends naturally to the dual error bound method of the literature, so as to get a probabilistic error bound on the corrected output.

Numerical results

We validate our method on a standard benchmark for reduced bases, the Venturi model (Rozza and A.T., 2008). The considered PDE is as follows:

$$\begin{cases} \Delta u_e = 0 \text{ in } \Omega(\mu) \\ u_e = 0 \text{ on } \Gamma_D \\ \frac{\partial u_e}{\partial n} = -1 \text{ on } \Gamma_N \\ \frac{\partial u_e}{\partial n} = 0 \text{ on } \partial\Omega \setminus (\Gamma_N \cup \Gamma_D) \end{cases}$$

The three parameters:

$$\mu = (\mu_1, \mu_2, \mu_3) \in \mathcal{P} = [0.25, 0.5] \times [2, 4] \times [0.1, 0.2],$$

define the geometry of the domain $\Omega(\mu)$, see Figure 2.4. For this model we implement an offline / online strategy and calculate the four bounds seen previously:

1. Lipschitz bound,
2. dual bound (with the adjoint, on the corrected output),
3. probabilistic bound,

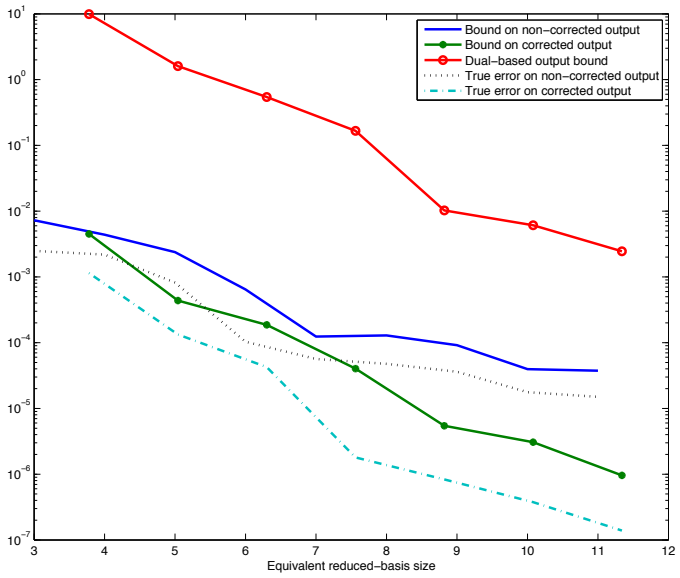

Figure 2.5: Comparison of the error bounds as a function of the reduced basis size. The probability error bound (with risk $\beta = 0.0001$) on the uncorrected output is blue, the true error is the black dashed line. For the corrected output, the true error is light blue, the dual bound red and the probability bound (with risk $\beta = 0.0001$) green. The Lipschitz bound is too large and not represented.

4. probabilistic bound on the corrected output.

Figure 2.5 compares these bounds with the actual error, as a function of the size of the reduced basis. In order to do a fair comparison, a change of scale on the basis size has been done for the bounds involving adjoint (because it requires offline and online calculations time twice as long) (see [21] for details). The Lipschitz bound is significantly worse than all others and does not even appear in the figure. We can see that our error bound for a risk $\beta = 0.0001$ is pretty close to the true error (less than one order of magnitude), and better than the existing dual bound.

The paper also presents the implementation of this method for a transport equation with the same kind of conclusions, see [21].

2.2 Global sensitivity analysis

In this section, we present the global sensitivity analysis problems that were considered (in parallel with our studies on model reduction) with C. Prieur, A. Janon, and Toulouse statisticians F. Gamboa, T. Klein and A. Lagnoux. To begin with, we present the Sobol sensitivity indices. Then we summarize the papers [9] *and* [11].

2.2.1 Presentation

As we saw in the first part, most geophysical models have a number of poorly known parameters we often try to estimate by inverse methods. The first step, of course, before even considering an inverse method, is to identify the most sensitive model parameters, those whose uncertainty will impact most strongly the forecast errors.

Framework and notations

We assume in this section that the input parameters are p real variables $X_1, ..., X_p$, and the model output Y is a real variable given by

$$Y = f(X_1, ..., X_p)$$

where f is a function $\mathbb{R}^p \to \mathbb{R}$. For example, in the Venturi model discussed above, X_i are the geometric parameters of the model and Y is the fluid flow through a boundary. Or, in a model of glaciological paleoclimatology, the X_i are the parameters related to the temperature and Y is the volume of ice at a given time.

It is natural to assume that the unknown parameters X_i are random variables. Their laws are generally unknown, but modeled according to the expertise of modellers and specialists. For the moment, many geophysical models are deterministic, but if X_i are random variables, then Y is a random variable.

There are different ways to quantify the sensitivity of a model to its input parameters. We can already distinguish global vs local sensitivity analysis. The latter is simply the mathematical translation of the question: if the input varies *around a reference value*, how will the ouput vary? The derivation of the model with respect to the parameters at the desired point $\partial_{X_i} f(x_1, ..., x_p)$ provides an answer to this question.

For an overall measure of sensitivity to a given parameter, we can still use the derivative, for example as follows:

$$\int_{\mathbb{R}^p} (\partial_{X_i} f(X_1, ..., X_p))^2 \, dX_1 ... dX_p$$

where the integral should be understood as the mathematical expectation of the random variable $(\partial_{X_i} f(X_1, ..., X_p))^2$.

But often we prefer to take advantage of the stochastic framework and propose a measure of sensitivity based on the variance, as we will see below.

Sobol global sensitivity indices

A popular way to measure the global sensitivity are Sobol variance-based indices (Sobol, 1993). The sensitivity index of the model with respect to the parameter X_i is defined as:

$$S_i = \frac{\mathrm{Var}\left(\mathbb{E}(Y|X_i)\right)}{\mathrm{Var}\left(Y\right)}$$

where $\mathbb{E}(Y|X_i)$ is the conditional expectation of Y given X_i. This is a random variable that depends only on X_i. Moreover, if the random variables are square-integrable, then we can see $\mathbb{E}(Y|X_i)$ as the orthogonal projection of Y on the set of the random variables in L^2 depending only on X_i. So, among the functions of X_i, $\mathbb{E}(Y|X_i)$ is the closest to Y in the least squares sense. The variance of $\mathbb{E}(Y|X_i)$ quantifies the dispersion of Y when only X_i varies. Therefore, the quotient S_i is the variation of Y that can be explained solely by changes in X_i. An index close to 0 indicates that Y is weakly influenced by X_i. In contrast, an index close to 1 shows that X_i has a large impact on Y.

Monte Carlo estimation of Sobol indices

Except in very simple cases (usually academic examples), we can not explicitely calculate Sobol indices, not even as functions of the input parameters, and we must resort to numerical approximations. The Monte Carlo method is a popular approach. The idea is to simulate the randomness of the input variables by choosing a large suitable sample of these parameters, and then calculate Y for each of these parameters. Thus, a sample of inputs and outputs are available to estimate the indices.

The original estimator (Sobol, 2001) is recalled. For this we define two samples (random and identically distributed) of size N of p parameters:

$$(X_1^k, ..., X_p^k)_{k=1..N} \quad (X_1'^k, ..., X_p'^k)_{k=1..N}$$

Then we define

$$y_k = f(X_1^k, ..., X_p^k), \quad y'_k = f(X_1'^k, ...X_{i-1}'^k, X_i^k, X_{i+1}'^k, ..., X_p'^k), \quad \forall k = 1, ..., N$$

The estimator is then given by

$$\widehat{S}_i = \frac{\overline{yy'} - \overline{y}.\overline{y'}}{\overline{y^2} - \overline{y}^2} \tag{2.6}$$

where we define the empirical mean $\overline{\phi}$ of a vector $\phi = (\phi_1, ...\phi_N)$ by

$$\overline{\phi} = \frac{1}{N}\sum_{k=1}^{N} \phi_k$$

There are also other estimators, we will see some later. There are also other index estimation methods. Without going into details, the FAST method (see Tissot (2012) for a recent approach and historical references) and polynomial chaos (Ghanem and Spanos, 2003) can be mentioned. We refer to the thesis Janon (2012) for more details on these topics.

2.2.2 Using metamodels to estimate Sobol indices: quantifying information loss

This section summarizes the results contained in the article [9], with C. Prieur and A. Janon, as part of his thesis.

Problem presentation

In this work we estimate the Sobol index S_i with the estimator (2.6) proposed by Sobol (2001). From a practical point of view, it is often difficult to do a large number of model runs to compute y_k, because the model is generally quite expensive. In these cases, the model f is replaced by an approximation $\tilde{f}$, called metamodel, faster to compute. For example, we saw in the previous section a method based on reduced basis to build such a metamodel, but there are other approximation methods, in particular stochastic (kriging, regression, etc.). The estimator of interest is written as:

$$\widehat{S}_i = \frac{\overline{\tilde{y}\tilde{y}'} - \bar{\tilde{y}}.\bar{\tilde{y}'}}{\overline{\tilde{y}^2} - \bar{\tilde{y}}^2}$$

where the vectors $\tilde{y}$ and $\tilde{y}'$ are defined with the metamodel instead of the full model:

$$\tilde{y}_k = \tilde{f}(X_1^k, ..., X_p^k), \quad \tilde{y}'_k = \tilde{f}(X_1'^k, ...X_{i-1}'^k, X_i^k, X_{i+1}'^k, ..., X_p'^k), \quad \forall k = 1, ..., N$$

The paper [9] aims to answer the following question: can we quantify the error between the estimator $\widehat{S}_i$ and the true value of the index? There are two sources of error: the first arises because we use the metamodel instead of the full model (error metamodel), the second comes from the approximation by Monte Carlo with a sample of size N (sampling error).

Past works. There are few studies that quantify the estimation error, especially the error due to metamodel, although most calculations of sensitivity index estimates are conducted with metamodels. We can cite Marrel et al. (2009) who provide an error estimate in the case of a kriging metamodel.

Storlie et al. (2009) also offer an error estimate, using an approach based on the bootstrap approach (Efron, 1979). The method given in Janon (2012) is described below. We are given a training sample

$$\mathcal{D} = \{(\boldsymbol{X}^1, f(\boldsymbol{X}^1)), \ ..., \ (\boldsymbol{X}^n, f(\boldsymbol{X}^n))\}$$

used to build a metamodel $\tilde{f}_{\mathcal{D}}$. We then repeat for $r = 1, ..., R$ the following steps:

1. draw with equal probability in $(\boldsymbol{X}^1, ..., \boldsymbol{X}^n)$ (with replacement) a sample of size n $(\boldsymbol{X}^{*1}, ..., \boldsymbol{X}^{*n})$;

2. draw with equal probability and with replacement in the residuals set

$$\{\tilde{f}(\boldsymbol{X}^k) - f(\boldsymbol{X}^k), k = 1, ..., n\}$$

a residual sample of size n $(e^{*1}, ..., e^{*n})$;

3. calculate a noisy version of the learning sample:

$$\mathcal{D}^* = \{(\boldsymbol{X}^{*1}, \tilde{f}(\boldsymbol{X}^{*1}) + e^{*1}),\ ...,\ (\boldsymbol{X}^{*n}, \tilde{f}(\boldsymbol{X}^{*n}) + e^{*n})\};$$

4. with this sample make a new metamodel $\tilde{f}_{\mathcal{D}^*}$, and calculate with this metamodel a replication $\widehat{S_i^r}$ of the estimator.

Then we use the set

$$\mathcal{R} = \{\widehat{S_i^1}, ..., \widehat{S_i^R}\}$$

to build a confidence interval for S_i. This method is more general than the previous one, because it can be applied to different types of metamodels. However it is very expensive, especially because of step 4, which requires building a new metamodel from the new sample.

Quantification of the estimation errors

Metamodel error. The starting point of this work is to have an error bound on the metamodel. Based on our work on reduced basis, we assumed that we could have an error bound:

$$|f(\boldsymbol{X}) - \tilde{f}(\boldsymbol{X})| \leq \varepsilon(\boldsymbol{X}), \quad \forall \boldsymbol{X}$$

where we denoted $\boldsymbol{X} = (X_1, ..., X_p)$ the vector of model input parameters. For an element $\boldsymbol{X}^k$ of the sample it is written:

$$|y_k - \tilde{y}_k| \leq \varepsilon(\boldsymbol{X}^k) = \varepsilon_k$$

We start with the following remark: $\widehat{S}_i$ is the slope of the linear regression of y'_k on y_k:

$$\widehat{S}_i = \underset{a\in\mathbb{R}}{\operatorname{argmin}} \sum_{k=1}^{N} \left((y'_k - \overline{y'}) - a(y_k - \overline{y})\right)^2 = \underset{a\in\mathbb{R}}{\operatorname{argmin}}\, R(a, \boldsymbol{y}, \boldsymbol{y'}, \overline{y}, \overline{y'})$$

where we denoted $\boldsymbol{y} = (y_1, ..., y_N)$ the sample (same for $\boldsymbol{y'}$). The idea is then to write that each y_k lies in the interval $[\tilde{y}_k - \varepsilon_k; \tilde{y}_k - \varepsilon_k]$ and to generate an interval for $R(a, \boldsymbol{y}, \boldsymbol{y'}, \overline{y}, \overline{y'})$. We then deduce the inequality

$$\widehat{S}_i^m \leq \widehat{S}_i \leq \widehat{S}_i^M$$

In the case where ε is large, this method is quite pessimistic. Assuming more regularity on the function f (which is usually the case because the models are often quite regular), we also propose a smooth version of this inequality with a sharper width.

Sampling error. To estimate this error, the bootstrap method (see above) is applied directly to the estimators $\widehat{S}_i^m$ and $\widehat{S}_i^M$. Replications are used to build two confidence intervals: $[I_1^m, I_2^m]$ for $\widehat{S}_i^m$ and $[I_1^M, I_2^M]$ for $\widehat{S}_i^M$, which gives us an interval $[I_1^m, I_2^M]$ for S_i.

Application

The method for constructing confidence intervals is applied to the parameterised viscous Burgers equation we saw in subsection 2.1.2. First we consider that only two parameters are unknown, the viscosity ν and u_{0m} in the initial condition $u_0(x) = u_{0m} + 5\sin(x/2)$. We assume that ν varies between 1 and 20 and u_{0m} between 0 and 0.3, both parameters are

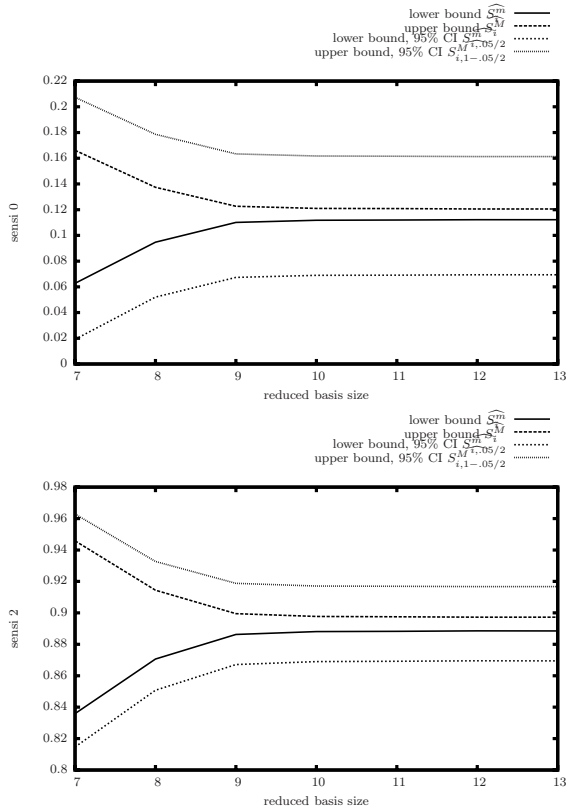

Figure 2.6: Convergence of the confidence intervals for the sensitivity indices estimation, on the left for ν, on the right for u_{0m}. The y axis represents $\widehat{S}_i^m$ and $\widehat{S}_i^M$, and the bounds of the confidence intervals at level 95%. The x axis represent the size of the reduced basisThe Monte Carlo sample size is fixed to $N = 2000$.

independent and follow uniform laws on these intervals. As this model is less expensive than a 3D geophysical model, we could calculate very accurate confidence intervals for sensitivity indices for these two parameters:

$$S_\nu \in [0.0815; 0.0832], \quad S_{u_{0m}} \in [0.9175; 0.9182]$$

which serve as a reference for the future.

Confidence intervals and coverage. With a reduced basis of $n = 9$ elements and a Monte-Carlo sample size $N = 300$ a confidence interval at level 95 % can be computed. If the confidence interval is perfect, it means that the coverage probability (ie the probability that the true value is actually in the interval) is 0.95. To validate this point, the method is repeated 100 times and we count how many times the confidence interval actually contains the true index, which gives us an empirical coverage. The table below presents the results and validates the method:

Parameter	Mean confidence interval	empirical coverage
ν	[0.0139;0.2083]	0.91
u_{0m}	[0.8421;0.9491]	0.87

Convergence. Figure 2.6 shows the evolution of the bounds $\widehat{S}_i^m$ and $\widehat{S}_i^M$ as a function of the reduced basis size for a fixed size Monte Carlo sample. This shows that the metamodel error decreases rapidly with the size of the reduced basis. The width of the confidence interval is large because sampling error is fixed. Note that the intervals $[\widehat{S}_i^m; \widehat{S}_i^M]$ do not take into account the Monte Carlo error and do not (usually) contain the true value of the index.

The end of paper [9] has other applications: the same Burgers model with more parameters, and another type of model (interpolation kernels). Both highlight the good performance of the proposed confidence interval, especially compared to existing methods in the literature.

2.2.3 Asymptotic study of Sobol indices estimation

This section summarizes the results contained in the article [11], in collaboration with F. Gamboa, A. Lagnoux and T. Klein Toulouse, with C. Prieur and A. Janon, as part of his thesis and in the framework of ANR COSTA BRAVA.

Presentation

The context of this work is the study of asymptotic properties of two Monte Carlo Sobol indices estimators. More specifically, we focus on the asymptotic behavior of two errors (metamodel and sampling) when both the learning sample for the metamodel and the Monte Carlo sample sizes tend to infinity.

The underlying concepts of interest are the asymptotic normality and efficiency. The first measures the convergence of the estimator to the true index, which helps to justify the asymptotic confidence intervals. The second allows to define the optimality of an estimator, in a certain sense, and thus to obtain the most accurate confidence intervals.

Notations. We are interested in the following type of model

$$Y = f(X, Z)$$

where $X \in \mathbb{R}^{p_1}$ and $Z \in \mathbb{R}^{p_2}$ are independent random variables called input parameters. We denote $p = p_1 + p_2$ the total number of parameters. If Y has non-zero variance and is square integrable, we are interested in the sensitivity index with respect to X:

$$S^X = \frac{\mathrm{Var}\left(\mathbb{E}(Y|X)\right)}{\mathrm{Var}\left(Y\right)} \in [0, 1]$$

If we denote by $Y^X = f(X, Z')$ where Z' is an independent copy of Z, we can see that

$$S^X = \frac{\mathrm{Cov}\left(Y, Y^X\right)}{\mathrm{Var}\left(Y\right)}$$

The first estimator that we consider is the following:

$$S_N^X = \frac{\frac{1}{N}\sum Y_i Y_i^X - \left(\frac{1}{N}\sum Y_i\right)\left(\frac{1}{N}\sum Y_i^X\right)}{\frac{1}{N}\sum Y_i^2 - \left(\frac{1}{N}\sum Y_i\right)^2}$$

with, for $i = 1, \dots, N$:

$$Y_i = f(X_i, Z_i), \quad Y_i^X = f(X_i, Z_i'),$$

where $\{(X_i, Z_i)\}_{i=1,\dots,N}$ and $\{(X_i, Z_i')\}_{i=1,\dots,N}$ are two independent and identically distributed samples (according to the law of (X, Z)), with $\{Z_i\}_i$ independent of $\{Z_i'\}_i$.

The second estimator is:

$$T_N^X = \frac{\frac{1}{N}\sum Y_i Y_i^X - \left(\frac{1}{N}\sum\left[\frac{Y_i+Y_i^X}{2}\right]\right)^2}{\frac{1}{N}\sum\left[\frac{Y_i^2+(Y_i^X)^2}{2}\right] - \left(\frac{1}{N}\sum\left[\frac{Y_i+Y_i^X}{2}\right]\right)^2}$$

Asymptotic normality

We give two results of asymptotic normality: the first when the estimator is calculated using the exact model, the second with a metamodel.

Exact model. We first establish a consistency result, that is to say, the almost sure convergence ($a.s.$) of the estimators to the indices:

$$S_N^X \xrightarrow[N\to\infty]{a.s.} S^X \quad \text{and} \quad T_N^X \xrightarrow[N\to\infty]{a.s.} S^X$$

Then we have the following proposition regarding asymptotic normality.

Suppose that $\mathbb{E}(Y^4) < \infty$. Then we have the convergence in law ($\mathcal{L}$)

$$\sqrt{N}\left(S_N^X - S^X\right) \xrightarrow[N\to\infty]{\mathcal{L}} \mathcal{N}_1\left(0, \sigma_S^2\right) \quad \text{and} \quad \sqrt{N}\left(T_N^X - S^X\right) \xrightarrow[N\to\infty]{\mathcal{L}} \mathcal{N}_1\left(0, \sigma_T^2\right)$$

with

$$\sigma_S^2 = \frac{\mathrm{Var}\left((Y - \mathbb{E}(Y))\left[(Y^X - \mathbb{E}(Y)) - S^X(Y - \mathbb{E}(Y))\right]\right)}{(\mathrm{Var}\,(Y))^2}$$

$$\sigma_T^2 = \frac{\mathrm{Var}\left((Y - \mathbb{E}(Y))(Y^X - \mathbb{E}(Y)) - S^X/2\left((Y - \mathbb{E}(Y))^2 + (Y^X - \mathbb{E}(Y))^2\right)\right)}{(\mathrm{Var}\,(Y))^2}.$$

with $\sigma_T \leq \sigma_S$ (and equality if and only if $S^X \in \{0, 1\}$).

Metamodel. This time we have an inexpensive and approximate metamodel to compute Y:

$$\widetilde{Y} = \widetilde{f}(X, Z) = f(X, Z) + \delta,$$

where the perturbation $\delta = \delta(X, Z, \xi)$ is a function of a random variable xi independent of X and Z. As before, we define the aproximate index:

$$\widetilde{S}^X = \frac{\mathrm{Var}\left(\mathbb{E}(\widetilde{Y}|X)\right)}{\mathrm{Var}\left(\widetilde{Y}\right)}$$

and the two associated estimators

$$\widetilde{S}_N^X = \frac{\frac{1}{N}\sum \widetilde{Y}_i \widetilde{Y}_i^X - \left(\frac{1}{N}\sum \widetilde{Y}_i\right)\left(\frac{1}{N}\sum \widetilde{Y}_i^X\right)}{\frac{1}{N}\sum \widetilde{Y}_i^2 - \left(\frac{1}{N}\sum \widetilde{Y}_i\right)^2}$$

$$\widetilde{T}_N^X = \frac{\frac{1}{N}\sum \widetilde{Y}_i\widetilde{Y}_i^X - \left(\frac{1}{N}\sum\left[\frac{\widetilde{Y}_i+\widetilde{Y}_i^X}{2}\right]\right)^2}{\frac{1}{N}\sum\left[\frac{\widetilde{Y}_i^2+(\widetilde{Y}_i^X)^2}{2}\right] - \left(\frac{1}{N}\sum\left[\frac{\widetilde{Y}_i+\widetilde{Y}_i^X}{2}\right]\right)^2}$$

We start with a remark: if δ is independent of N (for example if we keep the same metamodel while we increase the Monte-Carlo sample size), then in general the estimators $\widetilde{S}_N^X$ and $\widetilde{T}_N^X$ are not consistent for estimating S^X. Therefore we suppose now that δ depends on N, denoted δ_N, and it is also assumed that $\mathrm{Var}\,\delta_N$ tends to 0 as $N \to \infty$. The normal convergence of $\sqrt{N}(\widetilde{S}_N^X - S^X)$ as a function of the convergence rate of $\mathrm{Var}\,\delta_N$ to 0 is now studied. We have the following theorem.

Let us define

$$\begin{aligned} C_{\delta,N} &= 2\mathrm{Var}\,(Y)^{1/2}\left[\mathrm{Corr}\,(Y,\delta_N^X) - \mathrm{Corr}\,(Y,Y^X)\mathrm{Corr}\,(Y,\delta_N)\right] \\ &\quad + \mathrm{Var}\,(\delta_N)^{1/2}\left[\mathrm{Corr}\,(\delta_N,\delta_N^X) - \mathrm{Corr}\,(Y,Y^X)\right] \end{aligned}$$

where $\delta_N^X = \delta_N(X,Z')$ and $\mathrm{Corr}\,(A,B)$ is the correlation between A and B (covariance normalized by the standard deviations). Assume that $C_{\delta,N}$ does not converge to 0. Then

1. If $\mathrm{Var}\,(\delta_N) = o\left(\frac{1}{N}\right)$, then $\widetilde{S}_N^X$ and $\widetilde{T}_N^X$ are asymptotically normal to estimate S^X:

$$\sqrt{N}(\widetilde{S}_N^X - S^X) \underset{N\to+\infty}{\longrightarrow} \mathcal{N}(0,\sigma_S^2) \quad \text{and} \quad \sqrt{N}(\widetilde{T}_N^X - S^X) \underset{N\to+\infty}{\longrightarrow} \mathcal{N}(0,\sigma_T^2).$$

2. If $N\mathrm{Var}\,(\delta_N) \to \infty$, then they are not asymptotically normal.

3. If $C_{\delta,N}$ converges to a constant C and there exists $\gamma \in \mathbb{R}$ such that $\mathrm{Var}\,(\delta_N) = \frac{\gamma}{CN} + o\left(\frac{1}{N}\right)$, then:

$$\sqrt{N}(\widetilde{S}_N^X - S^X) \underset{N\to+\infty}{\longrightarrow} \mathcal{N}(\gamma,\sigma_S^2) \quad \text{and} \quad \sqrt{N}(\widetilde{T}_N^X - S^X) \underset{N\to+\infty}{\longrightarrow} \mathcal{N}(\gamma,\sigma_T^2)$$

Of course, if $C_{\delta,N}$ converges to 0, then we have the asymptotic normality for $\widetilde{S}_N^X$ and $\widetilde{T}_N^X$.

The proofs of these results are available in [11].

Asymptotic efficiency

I have not contributed to the results of asymptotic efficiency. In short, the concept of efficiency is as follows. Suppose we have an estimator S_N, which therefore forms for $N \in \mathbb{N}$ a sequence of estimators $(S_N)_{N\in\mathbb{N}}$, for a variable S. If S_N is asymptotically normal for S, then we have

$$\sqrt{N}(S_N - S) \underset{N\to\infty}{\overset{\mathcal{L}}{\to}} \mathcal{N}(O,\sigma^2)$$

This allows to construct asymptotic confidence intervals for S whose width is σ. The notion of asymptotic efficiency applies to the sequence whose asymptotic variance is the smallest possible (and therefore the narrowest confidence interval). The concept of efficiency is more complex, because the optimality is set on a subset of so-called regular sequences of estimators, we refer to Janon (2012) and to van der Vaart (1998) for more details. In the article [11], we show that under certain conditions the estimator sequences $(T_N^X)_N$ and $(\widetilde{T}_N^X)_N$ are asymptotically efficient for estimating S^X.

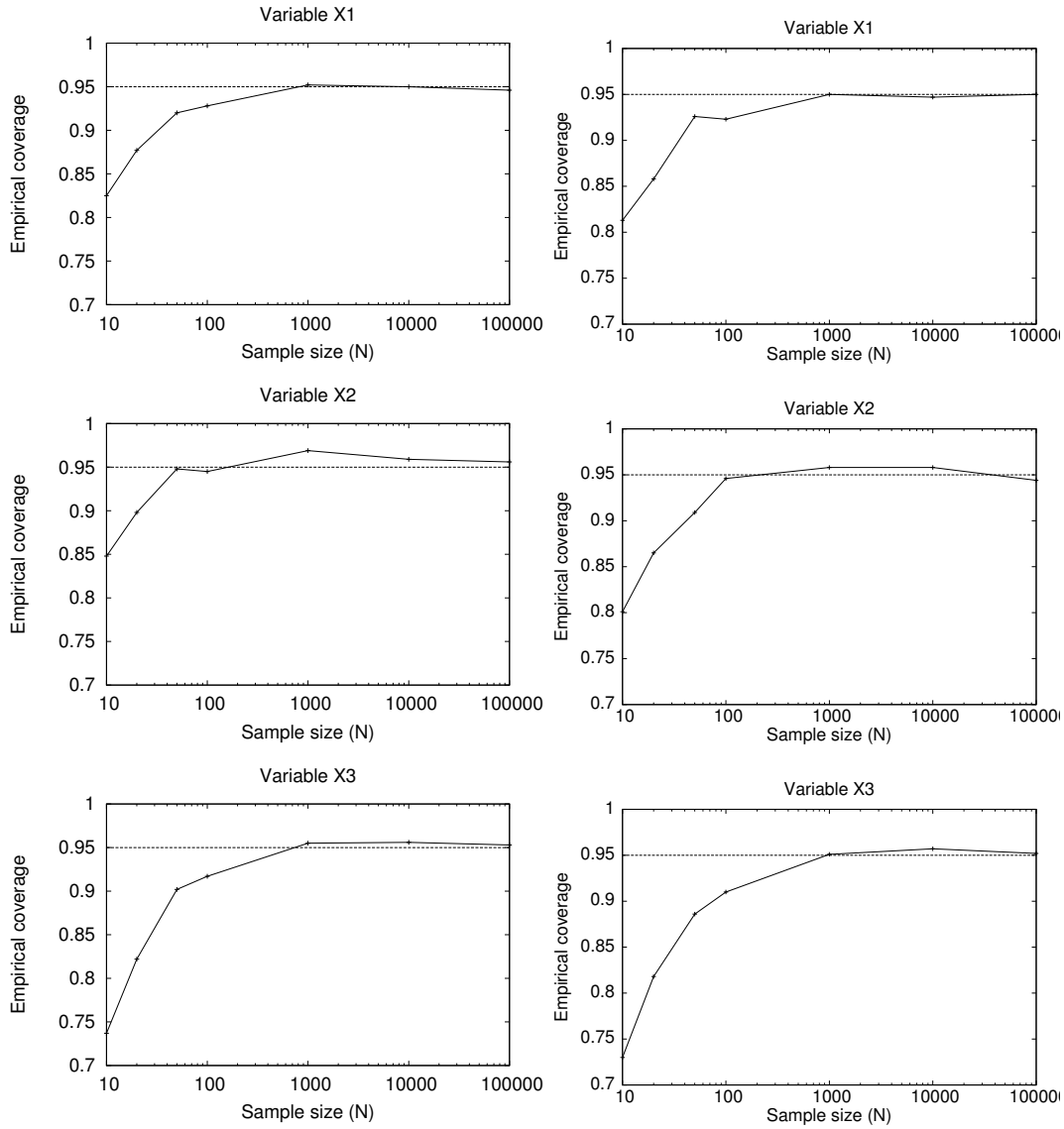

Figure 2.7: Empirical coverage for the asymptotic confidence intervals of S^1 (top), S^2 (middle) et S^3 (bottom), as a function of the Monte Carlo sample size N, for the estimators S_N (left) and T_N (right) with the exact model.

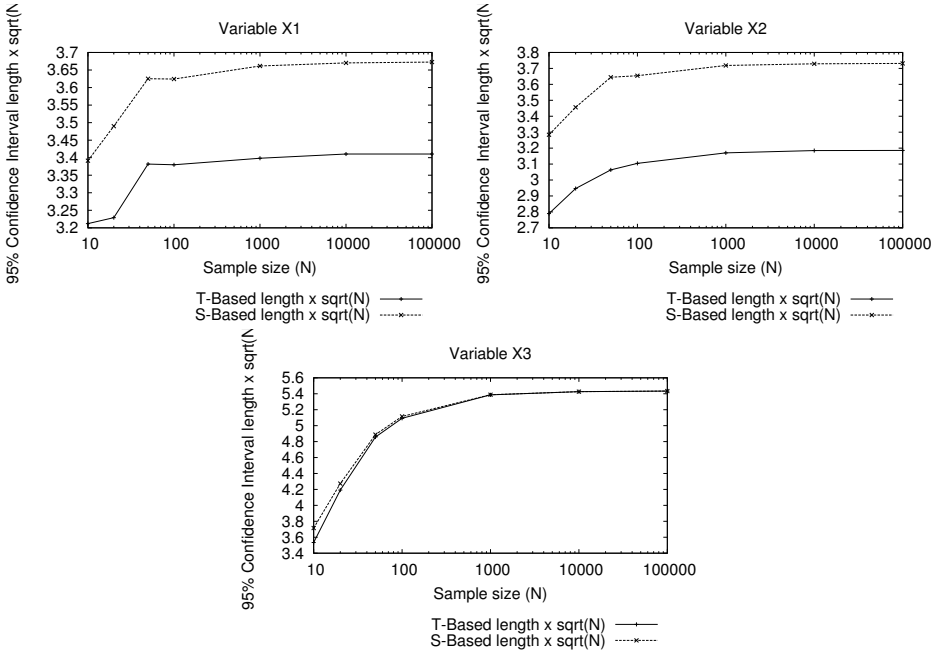

Figure 2.8: Confidence interval width (multiplied by $\sqrt{N}$) for S^1, S^2 et S^3, as a function of N, for T_N (solid line) and S_N (dashed) with the exact model.

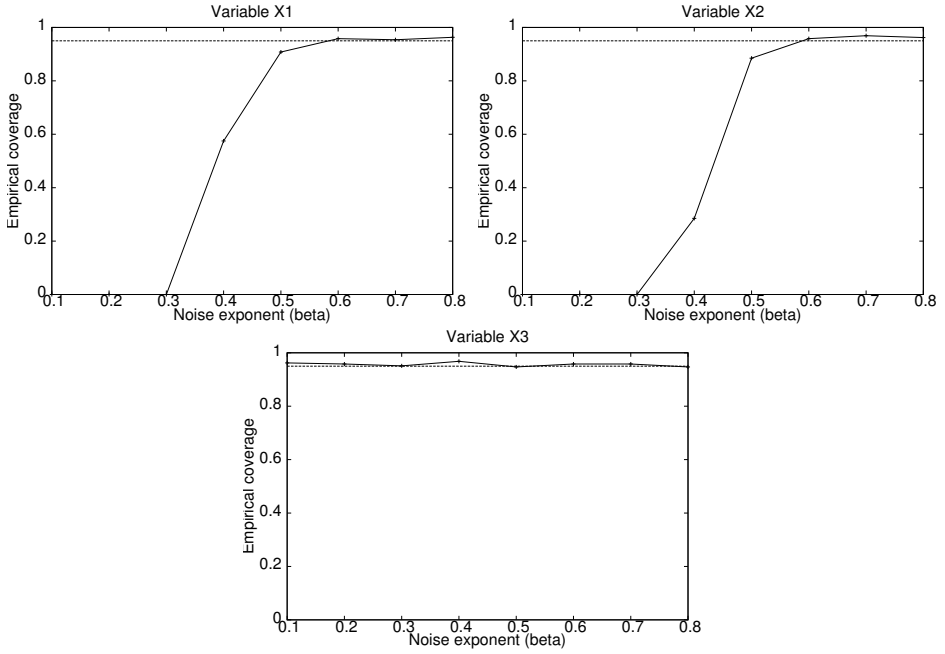

Figure 2.9: Empirical coverage for the asymptotic confidence intervals of S^1, S^2 and S^3, as a function of the noise level β, for the gaussian-perturbated model $\tilde{f}_N$.

Numerical illustrations

The previous results are illustrated with the Ishigami function (see Ishigami and Homma (1990))

$$f(X_1, X_2, X_3) = \sin X_1 + 7 \sin^2 X_2 + 0.1 X_3^4 \sin X_1$$

where $(X_j)_{j=1,2,3}$ are independent random variables following the same uniform distribution on $[-\pi; \pi]$.

We denote by S^1 the Sobol index S^{X_1} with $Z = (X_2, X_3)$, and similarly for S^2 and S^3. The exact values of these indices are known:

$$S^1 = 0.3139, \quad S^2 = 0.4424, \quad S^3 = 0.$$

To illustrate the previous results we will proceed as follows: we construct an asymptotic confidence interval at level 95%. To validate this interval the empirical coverage is computed (as above in paragraph 2.2.2) by replicating $R = 1000$ confidence intervals. The proportion of intervals containing the true value gives the empirical coverage, which should be close to 95%.

Exact model. First we consider the estimators S_N^X and T_N^X with the exact model. Figure 2.7 shows the empirical coverages obtained as a function of N. We note that these probabilities tend to 0.95 when N tends to infinity, which shows the reliability of the asymptotic confidence intervals.

Figure 2.8 compares the efficiency of S_N and T_N, showing the width of the confidence interval (multiplied by $\sqrt{N}$) as a function of N. We see that T_N is better than S_N, except for S^3 for which we have $S^3 = 0$.

Perturbed model. Then a model disturbed by Gaussian noise is considered

$$\widetilde{f}_N = f + \frac{5\xi}{N^{\beta/2}}$$

where $\beta > 0$ and ξ follows a standard normal distribution. We have $\delta_N = 5\frac{\xi}{N^{\beta/2}}$ and $\operatorname{Var} \delta_N \propto N^{-\beta}$, then

$$C_\delta = O\left(\operatorname{Var}(\delta_N)^{1/2}\right) = O\left(N^{-\beta/2}\right),$$

The proof of the theorem tells us that $\widetilde{S}_N$ is asymptotically normal for S if $\beta > 1/2$. For X_1 and X_2 we have the converse property, as $C_\delta \sim N^{-\beta/2}$. For X_3, we have $C_\delta = 0$ and $\widetilde{S}_N$ is asymptotically normal for S whatever $\beta > 0$. Figure 2.8 illustrates this. We set N large enough and the empirical coverage based is plotted as a function of β. We see that this probability is close to 0.95 when $\beta > 1/2$ for S^1 and S^2, and for all β for S^3.

Kriging metamodel. Then we consider a kriging metamodel, built from a training sample of size n. The larger n is, the more accurate the metamodel, but also the more expensive to build. Without going into details (we refer to [11]), we can prove that, under some assumptions, the noise of such a metamodel satisfies

$$\operatorname{Var} \delta \leq C e^{-k n^{1/p}}$$

where C and k are constants. Applying this to the Ishigami function and using exponential regression to estimate the coefficients, we get

$$\mathrm{Var}\,(\delta) \approx \widehat{C}e^{-\widehat{k}n^{1/3}}, \qquad \widehat{k} = 1.91$$

This leads us to propose the following relation between n and N:

$$n = (a \ln N)^3$$

and the theorem tells us that we have asymptotic normality if $a > 1/\widehat{k}$, ie $a > 0.52$. Although there is no evidence that this condition is necessary and sufficient, one can nevertheless study the empirical coverage as a function of a (knowing that the theoretical coverage is still 0.95 here):

a	N	n	Empirical coverage for S^1	for S^2	for S^3
.4	3000	33	0.1	0	0.7
.4	4000	37	0.08	0	0.78
.4	6000	43	0.26	0.3	0.88
.4	10000	51	0.28	0.18	0.78
.4	20000	77	0.28	0.1	0.59
.6	3000	111	0.79	0.37	0.9
.6	4000	124	0.8	0.7	0.94
.6	10000	169	0.92	0.82	0.94
.6	20000	210	0.93	0.85	0.95
.7	3000	177	0.93	0.88	0.93
.7	4000	196	0.9	0.91	0.94
.7	6000	226	0.94	0.93	0.97
.8	4000	293	0.95	0.95	0.95

and we see indeed a change of regime between $a = 0.4$ and $a = 0.6$.

Non-parametric regression. The article also provides another type of metamodel (nonparametric regression) which gives the same kind of result. The advantage of this metamodel is that it does not require the full model, but noisy observations suffice. The downside is that this time $n = N^a, a > 1.16$, which requires a larger learning sample for the metamodel in order to get the asymptotic normality of the estimators.

2.3 Back and Forth Nudging algorithm

In this section we summarise the works [5] and [7], in collaboration with D. Auroux and J. Blum (Nice) on a new data assimilation algorithm, the back and forth nudging (BFN).

2.3.1 Presentation

Nudging

The algorithm of the back and forth nudging (BFN) was recently introduced by Auroux and Blum (2005) as a data assimilation method which is extremely simple to implement. This method is based on the nudging, also called Newtonian relaxation, or Luenberger observer (linear case). The idea of nudging is to relax the model to the observations by adding a feedback term in the second member of the PDE. If the evolution equation of the model is written as:

$$\frac{dX}{dt} = F(X), \quad 0 < t < T, \quad X(0) = s_0$$

and observations are available $X^{\text{obs}}(t)$ via an observation operator C, then the nudging is written

$$\frac{dX}{dt} = F(X) - K(C(X) - X^{\text{obs}}), \quad 0 < t < T, \quad X(0) = x_0$$

where K is a positive coefficient (or matrix).

The theory of observers says that, under certain conditions and for an optimal choice of K, the state X tends to the observations, when t tends to infinity. For geophysical models, these assumptions are not valid, and we want results in finite time (the size of the assimilation window is a few hours for NWP and a few weeks weather in the ocean). However, the nudging has been used with some success in meteorology (Hoke and Anthes, 1976) and oceanography (Verron and Holland, 1989; Blayo et al., 1994).

BFN algorithm

The main idea of the BFN is: since it is limited to a finite time window, we would like to correct this by making several successive nudging cycles on the same time window. To do this, we need to have a corrected initial condition, thanks to backward nudging (Auroux, 2003):

$$\frac{d\tilde{X}}{dt} = F(\tilde{X}) + K'(C(\tilde{X}) - X^{\text{obs}}), \quad T > t > 0, \quad \tilde{X}(T) = X(T)$$

where this time the model is backward in time, starting from the final condition $X(T)$, and by changing the sign of the relaxation. Thus, a new initial condition $\tilde{X}(0)$ is available, which can be used to initiate a new phase of nudging.

The BFN algorithm is then written as (Auroux and Blum, 2005):

$$\text{Initialise } \tilde{X}_0(0) = x_0, \text{ then iterate until convergence, for } k \geq 1 :$$

$$\begin{cases} \partial_t X_k = F(X_k) + K(X^{\text{obs}} - H(X_k)), \\ X_k(0) = \tilde{X}_{k-1}(0), \quad 0 < t < T, \end{cases} \qquad \begin{cases} \partial_t \tilde{X}_k = F(\tilde{X}_k) - K'(X^{\text{obs}} - H(\tilde{X}_k)), \\ \tilde{X}_k(T) = X_k(T), \quad T > t > 0. \end{cases}$$

A detailed presentation of the algorithm, including its variational interpretation and its relationship with the observers is available in Auroux (2008).

2.3.2 Negative theoretical results

This section summarizes the section [5], in collaboration with D. Auroux (Nice).

Discussion

As might expect the reader who reads for the first time the BFN algorithm applied to the heat equation, the backward equation can have stability problems in the presence of viscosity. The first applications of BFN (Auroux and Blum, 2008; Auroux, 2009) however show good numerical performance for models of varying complexity (Lorenz, Burgers, quasi-geostrophic, Shallow-Water), even in the presence of viscosity. It turns out, however, that the viscosity coefficients are very low, and the backward nudging coefficient K' is large enough to compensate for the instability related to the backward Laplacian operator.

With D. Auroux we therefore studied the (non-)convergence of the algorithm in [5], at least for transport equations (linear and Burgers). We managed to prove that in the absence of viscosity convergence is assured. By cons, in the presence of viscosity we do not have convergence anymore or even solutions to the backward equation, except in the very special case where the state is observed everywhere and at all times (ie $C = 1$). We state below the theorems obtained in the linear case, we have the same kind of results in the non-linear case.

Non-viscous transport equation

Transport equation is considered

$$\left\{\begin{array}{rcl} \partial_t u_{\text{true}} + a(x)\partial_x u_{\text{true}} &=& 0, (t,x) \in [0,T]\times\Omega \\ u_{\text{true}}|_{x=0} &=& u_{\text{true}}|_{x=1}, \\ u_{\text{true}}|_{t=0} &=& u^0_{\text{true}}, \end{array}\right.$$

where Ω is the torus $\mathbb{R}/\mathbb{Z}$, $a(x) \in C^1(\Omega)$ and $u^0_{\text{true}} \in C^1(\Omega)$ are both periodic in space. Under these assumptions, we have existence and uniqueness of the solution $u_{\text{true}} \in C^1([0;T]\times\Omega)$.

Observations are available:

$$u_{\text{obs}}(t,x) = u_{\text{true}}(t,x), \text{ if } (t,x)\in\omega; \quad u_{\text{obs}}(t,x) = 0, \text{ if } (t,x)\notin\omega$$

$$\omega = \text{Support } (K) \subset [0,T]\times\Omega$$

The nudging constants K and $K' \in C^1([0;T]\times\Omega)$ are positive and may depend on t and x, and there exists a constant $\kappa \in \mathbb{R}^*_+$ such that $K'(t,x) = \kappa K(t,x)$.

The equations of one step of BFN are written

$$(F) \quad \left\{\begin{array}{rcl} \partial_t u + a(x)\partial_x u &=& -K(u-u_{\text{obs}}), \\ u|_{x=0} &=& u|_{x=1}, \\ u|_{t=0} &=& u_0, \end{array}\right.$$

$$(B) \quad \left\{\begin{array}{rcl} \partial_t \widetilde{u} + a(x)\partial_x \widetilde{u} &=& K'(\widetilde{u}-u_{\text{obs}}), \\ \widetilde{u}|_{x=0} &=& \widetilde{u}|_{x=1}, \\ \widetilde{u}|_{t=T} &=& u(T), \end{array}\right.$$

Then we denote

$$(s, \psi(s,x))$$

the characteristic curves of the forward equation with $K = 0$, with foot x at time $s = 0$, ie such that

$$(s, \psi(s, x))|_{s=0} = (0, x)$$

The characteristics are well defined and do not intersect on $[0, T]$.

We have existence and uniqueness of classical solutions u and $\widetilde{u} \in C^1([0;T] \times \Omega)$. We denote

$$\begin{aligned} w(t) &= u(t) - u_{\text{true}}(t), \\ \widetilde{w}(t) &= \widetilde{u}(t) - u_{\text{true}}(t). \end{aligned}$$

With these assumptions and notations, we can now state the following theorem:

1. If $K(t, x) = K$ constant in time and space, then for all $t \in [0, T]$ we have:

$$\widetilde{w}(t) = w(t) e^{(-K-K')(T-t)}.$$

2. If $K(t, x) = K \mathbb{1}_{[t_1,t_2]}(t)$ with $0 \leq t_1 < t_2 \leq T$, then we have:

$$\widetilde{w}(0) = w(0) e^{(-K-K')(t_2-t_1)}.$$

3. If $K(t, x) = K(x)$, then for all $t \in [0, T]$ we have:

$$\widetilde{w}(t, \psi(t, x)) = w(t, \psi(t, x)) \exp\left(- \int_t^T K(\psi(s, x)) + K'(\psi(s, x))\, ds \right).$$

In the latter case, the error decreases only when the characteristic intersect the support of $K(x)$. Anyway, the equations of BFN are well posed, and if we have enough observations in time and space, the error decreases (at least in observed areas).

Viscous transport equations

We consider this time the equation

$$\left\{ \begin{array}{rcl} \partial_t u - \nu \partial_{xx} u + a(x) \partial_x u &=& 0, \\ u|_{x=0} = u|_{x=1} &=& 0, \\ u_{t=0} &=& u^0_{\text{true}} \end{array} \right.$$

with:

- $a(x) \in W^{1,\infty}(\Omega)$;
- $\nu > 0$ constant;
- $u^0_{\text{true}} \in L^2(\Omega)$ and $u_0 \in L^2(\Omega)$.

Then we have existence and uniqueness of the solution $u_{\text{true}} \in C^0(0, T; L^2(\Omega)) \cap L^2(0, T; H^1(\Omega))$. This solution is used to generate observations u_{obs} as before.

Nudging coefficients with the same support ω as the observations are then defined: $K \in L^\infty([0;T] \times \Omega)$ and $K' \in L^\infty([0;T] \times \Omega)$ are positive and there exists $\kappa \in \mathbb{R}^*_+$ such that $K'(t, x) = \kappa K(t, x)$, and we have Support (K) = Support $(K') = \omega \subset [0, T] \times [0, 1]$.

One step of the BFN is written similarly:

$$(F)\quad \left\{\begin{array}{rcl} \partial_t u - \nu\partial_{xx}u + a(x)\partial_x u &=& -K(u-u_{\text{obs}}),\\ u|_{x=0} = u|_{x=1} &=& 0,\\ u|_{t=0} &=& u_0, \end{array}\right.$$

$$(B)\quad \left\{\begin{array}{rcl} \partial_t \widetilde{u} - \nu\partial_{xx}\widetilde{u} + a(x)\partial_x \widetilde{u} &=& K'(\widetilde{u}-u_{\text{obs}}),\\ \widetilde{u}|_{x=0} = \widetilde{u}|_{x=1} &=& 0,\\ \widetilde{u}|_{t=T} &=& u(T), \end{array}\right.$$

Assume that $u_0 \in L^2(\Omega)$ is given. We then have the following theorem:
The forward equation (F) has a unique solution $u \in C^0(0,T;L^2(\Omega)) \cap L^2(0,T;H^1(\Omega))$. In addition:

1. If $K(t,x) = K \in \mathbb{R}$, then equation (B) has a unique solution $\tilde{u} \in C^0(0,T;L^2(\Omega)) \cap L^2(0,T;H^1(\Omega))$. Moreover, if we note

$$\begin{array}{rcl} w(t) &=& u(t) - u_{\text{true}}(t),\\ \widetilde{w}(t) &=& \widetilde{u}(t) - u_{\text{true}}(t), \end{array}$$

   then for all $t \in [0,T]$ we have:

$$\widetilde{w}(t) = e^{(-K-K')(T-t)}w(t)$$

2. If $K(t,x) = K\mathbb{1}_{[t_1,t_2]}(t)$ with $K \in \mathbb{R}$ and $0 \leq t_1 < t_2 \leq T$, then equation (B) also has a unique solution $\widetilde{u} \in C^0(0,T;L^2(\Omega)) \cap L^2(0,T;H^1(\Omega))$ and we have

$$\widetilde{w}(0) = e^{(-K-K')(t_2-t_1)}w(0)$$

3. If $K(t,x) = K(x)$, with Support $(K) \subset [a,b]$ where $a < b$ and $a \neq 0$ or $b \neq 1$, then equation (B) is ill-posed: there does not exist, in general, a solution $\widetilde{u}$, even in the distributions sense.

Note that the existence of the backward solution strongly depends on the assumption that complete observations are available in space, at least for a while. In practice, this is of course not realistic, but nevertheless some observations (including satellites) have very good spatial coverage.

2.3.3 Algorithm improvement

This section summarizes the section [7], in collaboration with D. Auroux and J. Blum (Nice).

Starting point

Most geophysical models that are used in NWP and oceanography include viscous terms. The intrinsic viscosity of the fluid is generally very small, so that we can consider that the exact solution satisfies the inviscid equations. However, in practice viscous terms are added to allow the parameterization of sub-grid phenomena, ie unresolved by the model. Following the negative results [5] in the presence of viscosity, we proposed an improvement of the algorithm in the short note [7]. The idea is simply to assume that the viscosity is a numerical parameterization term, and thus change its sign in the backward equation.

Diffusive BFN

We work in the context of geophysical Newtonian fluids (atmosphere, ocean). It is assumed that the state of the system satisfies the following equation:

$$\partial_t X = F(X) + \nu \Delta X, \quad 0 < t < T, \quad X(0) = x_0$$

where the viscous terms are of the form $\nu\Delta X$, assuming that F contains only terms of transport (possibly non-linear) and also includes the boundary conditions. The observation operator is denoted H, and observations $X_{obs}(t)$ are available, to be compared to their model equivalent $H(X(t))$.

For $k \geq 1$ the diffusive BFN algorithm (D-BFN) is written

$$(F) \quad \begin{cases} \partial_t X_k = F(X_k) + \nu \Delta X_k + K(X_{obs} - H(X_k)) \\ X_k(0) = \tilde{X}_{k-1}(0), \quad 0 < t < T \end{cases}$$

$$(B) \quad \begin{cases} \partial_t \tilde{X}_k = F(\tilde{X}_k) - \nu \Delta \tilde{X}_k - K'(X_{obs} - H(\tilde{X}_k)) \\ \tilde{X}_k(T) = X_k(T), \quad T > t > 0 \end{cases}$$

The change of sign makes the backward problem generally well posed, and then we have convergence of the algorithm (see [7] for a proof in an idealized framework).

Applications

		$n_x = 4$ $n_t = 4$ Unnoisy	$n_x = 10$ $n_t = 10$ Unnoisy	$n_x = 10$ $n_t = 10$ Noisy (15%)
BFN with $\nu = 0$	No. iterations	2	2	2
	Relative RMS (%)	0.11	0.15	7.70
	K	15	43	52
	K'	30	86	104
BFN with $\nu = 0.001$	No. iterations	3	3	3
	Relative RMS (%)	0.15	0.34	8.62
	K	17	45	55
	K'	34	90	110
BFN2 with $\nu = 0.001$	No. iterations	6	4	3
	Relative RMS (%)	0.48	0.34	7.28
	K	2	10	18
	K'	4	20	36

Figure 2.10: Comparison table between BFN and D-BFN for the Burgers equation *without shock* with discrete and noisy observations, from Auroux et al. (2013) table 3.

The note [7] illustrates the algorithm in the elementary case of a transport equation with complete observations. More comprehensive tests were carried out in the article Auroux et al. (2013), where the authors propose to compare the BFN and D-BFN (called BFN2 in the article) algorithms for the assimilation of noisy observations with the Burgers equation without shock. Figure 2.10 shows the RMS errors obtained for three assimilation methods:

1. BFN with $\nu = 0$, ie the non-viscous Burgers quation,

		$n_x = 4$ $n_t = 4$ Unnoisy	$n_x = 10$ $n_t = 10$ Unnoisy	$n_x = 10$ $n_t = 10$ Noisy (15%)
BFN2 with $\nu = 0.02$	No. iterations	3	3	3
	Relative RMS (%)	1.13	1.22	6.97
	K	8	20	20
	K'	16	40	40

Figure 2.11: Comparison table between BFN and D-BFN for the Burgers equation *with shock* with discrete and noisy observations, from Auroux et al. (2013) table 6.

2. BFN with $\nu = 0.001$,
3. D-BFN with the same viscosity $\nu = 0.001$,

and for three different data sets:

1. perfect observations, available every 4 grid points and every 4 time steps,
2. perfect observations, available every 10 grid points and every 10 time steps,
3. noisy observations, available every 10 grid points and every 10 time steps.

It was found that the D-BFN algorithm gives slightly better results in the case of noisy observations, and it especially allows to use lower nudging constants.

More interestingly, the authors then consider the Burgers equation with shock. In this case, the BFN does not converge, while the D-BFN gives good results (see Figure 2.11).

2.4 Experimental study of the HUM method for waves

This paragraph presents works done in collaboration with G. Lebeau (Nice) about the control of the wave equation. The idea of this work was both to propose a numerical method and to use it to illustrate recent theoretical results. We first present the waves controlability problem and the HUM method, then we describe the numerical method and finally we show some numerical results. This section is directly pasted from the works [4] and [14].

Controllability of linear waves

For a given $f = (u_0, u_1) \in H_0^1(\Omega) \times L^2(\Omega)$, the problem is to find a source $v(t,x) \in L^2(0,T;L^2(\Omega))$ such that the solution $u = S(v)$ of the linear wave equation

$$\left\{ \begin{array}{l} \Box u = \chi v \quad \text{in }]0,+\infty[\times\Omega \\ u_{|\partial\Omega} = 0, \quad t > 0 \\ (u|_{t=0}, \partial u|_{t=0}) = (0,0) \end{array} \right. \tag{2.7}$$

reaches the state $f = (u_0, u_1) = (u(T,.), \partial_t u(T,.))$ at time T, where:

- Ω is a bounded open subset of $\mathbb{R}^d$,
- the "control domain" U is a non empty open subset of Ω,
- $\chi(t,x) = \psi(t)\chi_0(x)$ where χ_0 is a real L^∞ function on $\overline{\Omega}$, such that $\text{support}(\chi_0) = \overline{U}$ and $\chi_0(x)$ is continuous and positive for $x \in U$, $\psi \in C^\infty([0,T])$ and $\psi(t) > 0$ on $]0,T[$.

The reachable set at time T is the subspace of $H = H_0^1(\Omega) \times L^2(\Omega)$:

$$\mathcal{R}_T = \{f = (u_0,u_1) \in H, \exists v, (S(v)(T,.), \partial_t S(v)(T,.)) = (u_0,u_1)\}.$$

Then we have approximate controllability if $\mathcal{R}_T$ is dense in H and exact controllability if $\mathcal{R}_T = H$.

The HUM method

The Hilbert Uniqueness Method (HUM) of Lions (1988) consists in choosing the function v with L^2-minimal norm. Then v is necessarily of the form $\chi\partial_t w$ where w is a solution of the dual control problem:

$$\left\{ \begin{array}{l} \Box w = 0 \quad \text{in }]0,+\infty[\times\Omega \\ w_{|\partial\Omega} = 0, \quad t > 0 \\ (w|_{t=T}, \partial_t w|_{t=T}) = (w_0,w_1) = h \in H = H_0^1(\Omega) \times L^2(\Omega) \end{array} \right.$$

The HUM control operator is then defined by

$$\Lambda : \begin{array}{ccc} H & \to & H \\ f = (u_0,u_1) & \mapsto & h = (w_0,w_1) \end{array}$$

Let $A = A^*$ be the operator on $H = H_0^1(\Omega) \times L^2(\Omega)$ defined by

$$iA = \begin{pmatrix} 0 & \text{Id} \\ \Delta & 0 \end{pmatrix}$$

Let $\lambda = \sqrt{-\Delta_D}$. Then (2.7) becomes $(\partial_t - iA)u = B(t)v$ with

$$B(t) = \begin{pmatrix} 0 & 0 \\ \chi(t,.)\lambda & 0 \end{pmatrix}, \quad B^*(t) = \begin{pmatrix} 0 & \lambda^{-1}\chi(t,.) \\ 0 & 0 \end{pmatrix}$$

Then we have exact controlability iff

$$\exists C > 0, M_T = \int_0^T \mathrm{e}^{itA} B(T-t) B^*(T-t) e^{-itA^*}\, dt \geq C\,\mathrm{Id}$$

And in that case we have

$$\Lambda = M_T^{-1}$$

Geometric control condition

We recall that the source v in (2.7) is multiplied by $\chi(t,x) = \psi(t)\chi_0(x)$, where $\chi_0 \in L^\infty(\overline{\Omega})$, such that support$(\chi_0) = \overline{U}$ and $\chi_0(x)$ is continuous and positive for $x \in U$, $\psi \in C^\infty([0,T])$ and $\psi(t) > 0$ on $]0,T[$. We also assume that there is no contact of infinite order between $\partial\Omega$ and the optical rays of the wave operator in the free space. Let us recall the Geometric Control Condition (GCC) of C. Bardos, G. Lebeau and J. Rauch (Bardos et al., 1992): every geodesic ray of Ω traveling with speed 1 and starting at $t = 0$ enters the open set $U = \{x \in \Omega, \chi_0(x) \neq 0\}$ in time $t < T$.
We then have the theorem (Bardos et al., 1992): if χ and T are such that the GCC condition holds true, then M_T is an isomorphism, i.e. one has exact controlability ($\mathcal{R}_T = H$).

2.4.1 Numerical method

In previous works, Glowinski et al. (1990) first discretize the continuous wave equation, then compute the control of the discrete system. As precisely studied by Zuazua (2002, 2005), the discrete model is not uniformly exactly controllable when the mesh size goes to zero, and the interaction of waves with the numerical mesh produces spurious high frequency oscillations. In other words, the processes of numerical discretization and control do not commute for the wave equation. Thus, some multi-grid methods were developed to overcome this problem, see e.g. Glowinski et al. (2008); Asch and Lebeau (1998). Here we propose to implement the "control, then discretise" approach. A summary is presented below, and we refer to [4] for more details.

Let (ω_j^2) be the sequence of $-\Delta_D$ eigenvalues, and (e_j) the associated orthonormal basis of $L^2(\Omega)$:

$$-\Delta e_j = \omega_j^2 e_j, e_j|_{\partial\Omega} = 0$$

For a given cutoff frequency ω, we define

$$L^2_\omega = \mathrm{Span}\{e_j, \omega_j \leq \omega\}$$

and we denote by Π_ω the orthogonal projector on L^2_ω, which obviously acts also on $H = H_0^1 \times L^2$:

$$H_\omega = \Pi_\omega(H_0^1 \times L^2)$$

and we define the matrix $M_{T,\omega}$:

$$M_{T,\omega} = \Pi_\omega M_T \Pi_\omega, \qquad M_{T,\omega,n,m} = (M_T \phi_n | \phi_m)_H$$

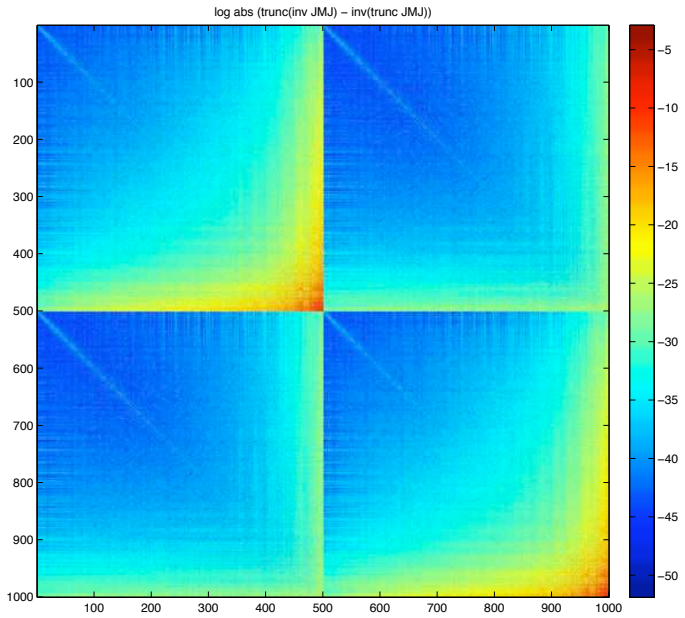

Figure 2.12: View of the logarithm of the coefficients of the matrix $J\left[((M_T)^{-1})_\omega - ((M_T)_\omega)^{-1}\right]J^{-1} = J\left[\Lambda_\omega - ((M_T)_\omega)^{-1}\right]J^{-1}$ with smooth control. The M_T matrix is computed with 2000 eigenvalues, the cutoff frequency ω is equal to the 500th eigenvalue.

where (ϕ_n) is an orthonormal basis of H_ω.
Let us recall that $\Lambda = M_T^{-1}$ and $M_{T,\omega} = \Pi_\omega M_T \Pi_\omega$.
Then we can show that $M_{T,\omega}$ is invertible on H_ω and $\|M_{T,\omega}^{-1}\|$ is bounded uniformly in ω (because of exact controlability). Under GCC we have the following result:
There exists $c > 0$ such that for all $f \in H$:

$$\|\Lambda(f) - M_{T,\omega}^{-1}(f_\omega)\|_H \leq c\|f - f_\omega\|_H + \|\Lambda(f_\omega) - M_{T,\omega}^{-1}(f_\omega)\|_H$$

with $f_\omega = \Pi_\omega f$ and $\lim_{\omega\to\infty} \|\Lambda(f_\omega) - M_{T,\omega}^{-1}(f_\omega)\|_H = 0$.

In other words, the processes of Galerkin approximation and inversion "almost" commute for M_T. This can be seen in Figure 2.12, which represents the operator $((M_T)^{-1})_\omega - ((M_T)_\omega)^{-1}$. See **?** for details.

2.4.2 Experimental study of HUM operator properties

We implemented in fortran 90 (and Matlab) the method presented above.

We implemented the algorithm for various 2D domains. We present here only the square geometry (see [4] for other examples). For each geometry, we choose a standard control domain U satisfying the geometric control condition. Figure 2.13 presents the geometry and control domain. As it has been proven by Dehman and Lebeau (2009) that the operator Λ has good properties when the control function $\chi(t,x)$ is smooth, we considered two cases: non-smooth control $\chi(t,x) = 1_{[0,T]}1_U$; smooth control $\chi(t,x) = \psi(t)\chi_0(x)$ with $\psi(t) = \frac{4t(T-t)}{T^2}1_{[0,T]}$ and similar smoothin for $\chi_0(x)$. Figure 2.13 presents the smoothed control domains as well.

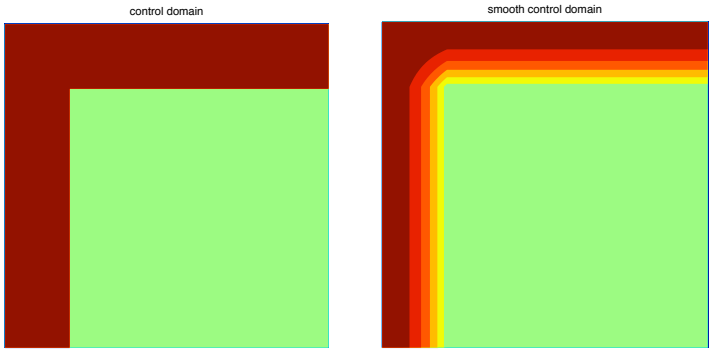

Figure 2.13: Geometries (green) and control domains (brown), without (left) or with (right) smoothing.

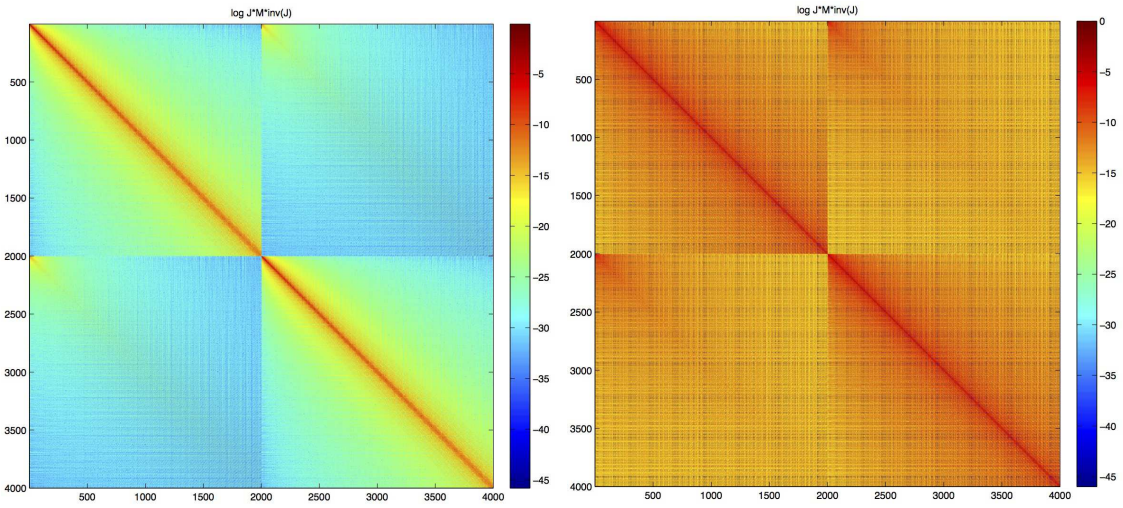

Figure 2.14: Impact of smoothing on $M_{T,\omega}$: view of the logarithm of the coefficients of $M_{T,\omega}$, for the square when GCC is valid, with smooth control on the left, non-smooth control on the right (same color scaling).

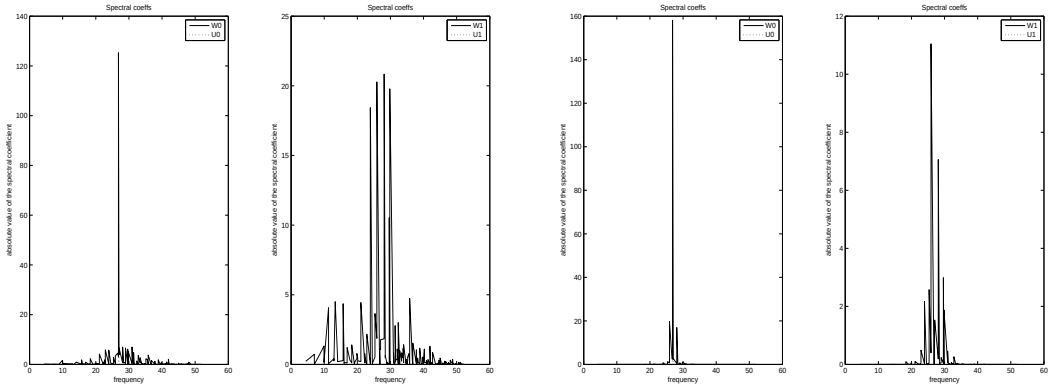

Figure 2.15: Frequency localization experiment in the square: localization of the Fourier frequences of (w_0, w_1) (left, right) for a given time T and a given domain U without smoothing (left) and with time- and space-smoothing (right). The x-coordinate represents the eigenvalues. The target data u_0 is equal to the 50-th eigenvector (eigenvalue of about 26.8), and $u_1 = 0$.

Regarding smoothing, figure 2.14 presents the coefficients of the M_T matrix with and without smoothing, with the same color scale. We clearly see that the coefficients decrease outside of the diagonal is much faster with smoothing than without.

Frequency localization

As an example of the experimental studies we have done, we show here one property of the HUM operator: the frequency localization, and the impact of smoothing on this property. We refer to **?** for an extended study of the HUM control operator.
The theoretical result states as follows (we refer to Dehman and Lebeau (2009); Lebeau (1992) for the details). Let $\psi_k(D)$, $k \in \mathbb{N}$, be the spectral localization operators associated to the Littlewood-Paley decomposition:

$$\psi_k(D)(\sum_j a_j e_j) = \sum_j \psi_k(\omega_j) a_j e_j, \quad S_k(D) = \sum_{j=0}^{k} \psi_j(D), k \geq 0$$

Assume that the geometric control condition holds true, and that the control function $\chi(t,x)$ is smooth. There exists $C > 0$ such that for every $k \in \mathbb{N}$, the following inequality holds true

$$\|\psi_k(D)\Lambda - \Lambda\psi_k(D)\|_H \leq C2^{-k}$$
$$\|S_k(D)\Lambda - \Lambda S_k(D)\|_H \leq C2^{-k}$$

Figure 2.15 shows the consequence of this result on the one-mode experiment, ie when the target data $f = (u_0, u_1)$ (to be reached) is equal to an eigenvector. We can see that the control (w_0, w_1) is almost equal to the same eigenvector, illustrating the above property.

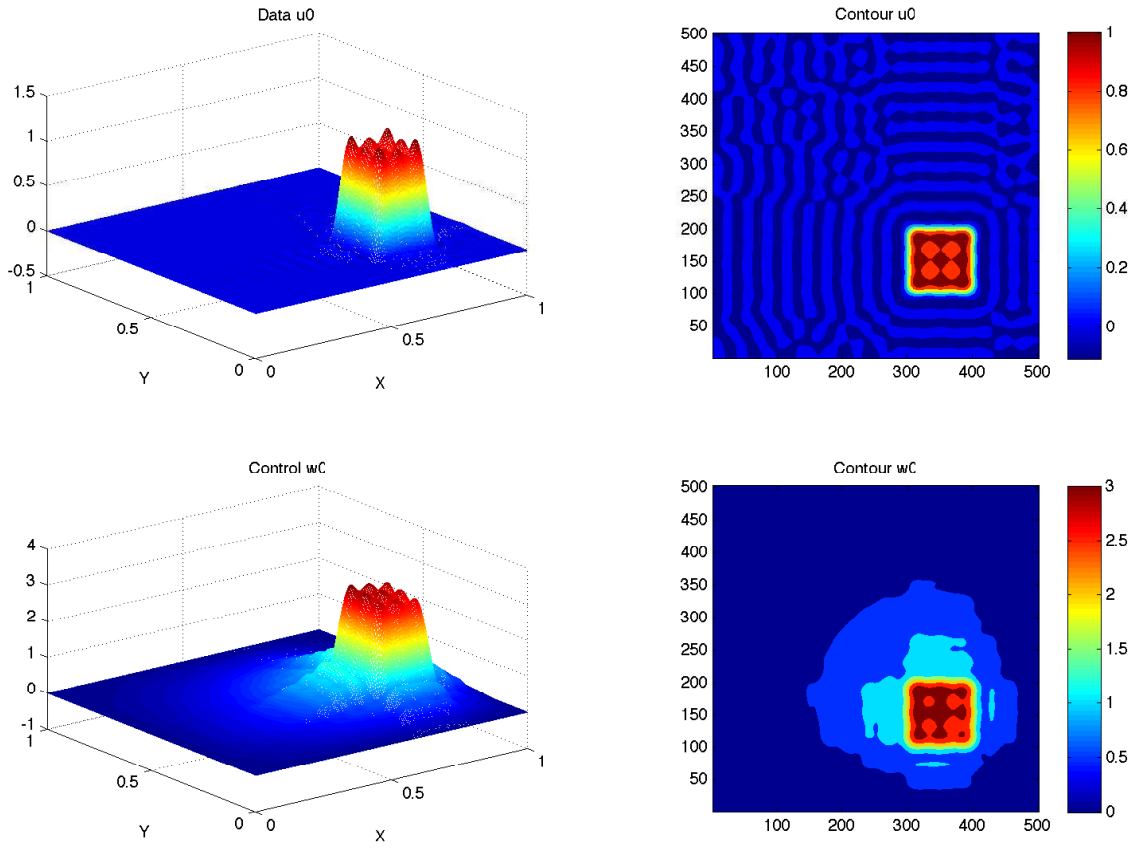

Figure 2.16: Space localization of the control function w_0 (bottom panels) with respect to the data u_0 (top panels), in the square, with smoothing. Left panels represent 3D view, and right panels show contour plots.

Space localisation

Regarding space localisation, we do not have theoretical results. However, the figure 2.16 is an example in which the support of the control $\boldsymbol{w}_0$ is identical to the target u_0. We have plenty of other examples, with/without smoothing, in other geometries and with other targets (see [4]) that could let us think that M_T could be a microlocal operator. That would mean it would actually preserve space as well as frequency localisation.

2.5 Bibliography 2

M. Asch and G. Lebeau. Geometrical aspects of exact boundary controllability of the wave equation. a numerical study. *ESAIM:COCV*, 3:163–212, 1998.

D. Auroux. *Étude de différentes méthodes d'assimilation de données pour l'environnement*. PhD thesis, Université de Nice, 2003.

D. Auroux and J. Blum. Back and forth nudging algorithm for data assimilation problems. *C. R. Acad. Sci. Paris Sér. I*, 340:873–878, 2005.

D. Auroux and J. Blum. A nudging-based data assimilation method for oceanographic problems: the back and forth nudging (bfn) algorithm. *Nonlin. Proc. Geophys.*, 15: 305–319, 2008.

Didier Auroux. Algorithmes rapides pour le traitement d'images et l'assimilation de données. *Mémoire de l'Habilitation à Diriger la Recherche, Université de Toulouse*, 3, 2008.

Didier Auroux. The back and forth nudging algorithm applied to a shallow water model, comparison and hybridization with the 4D-VAR. *International Journal for Numerical Methods in Fluids*, 61(8):911–929, November 2009.

Didier Auroux, Patrick Bansart, and Jacques Blum. An evolution of the back and forth nudging for geophysical data assimilation: application to Burgers equation and comparisons. *Inverse Problems in Science and Engineering*, 21(3):399–419, April 2013.

C. Bardos, G. Lebeau, and J. Rauch. Sharp sufficient conditions for the observation, control and stabilisation of waves from the boundary. *SIAM J.Control Optim.*, 305: 1024–1065, 1992.

E. Blayo, J. Verron, and J. M. Molines. Assimilation of TOPEX/POSEIDON altimeter data into a circulation model of the North Atlantic. *Journal of Geophysical Research*, 99:24691–24706, December 1994. doi: 10.1029/94JC01644.

A. Buffa, Y. Maday, A.T. Patera, C. Prud'homme, and G. Turinici. A priori convergence of the greedy algorithm for the parametrized reduced basis. *Mathematical Modelling and Numerical Analysis*, 2009.

T. Bui-Thanh, K. Willcox, O. Ghattas, and B. van Bloemen Waanders. Goal-oriented, model-constrained optimization for reduction of large-scale systems. *Journal of Computational Physics*, 224(2):880–896, 2007.

Y. Chen, J.S. Hesthaven, Y. Maday, and J. Rodríguez. Improved successive constraint method based a posteriori error estimate for reduced basis approximation of 2d maxwell's problem. *ESAIM: Mathematical Modelling and Numerical Analysis*, 43 (06):1099–1116, 2009.

Nguyen Ngoc Cuong, Karen Veroy, and Anthony T Patera. Certified real-time solution of parametrized partial differential equations. In *Handbook of Materials Modeling*, pages 1529–1564. Springer, 2005.

B. Dehman and G. Lebeau. Analysis of the HUM Control Operator and Exact Controllability for Semilinear Waves in Uniform Time. *SIAM J.Control Optim.*, 2009. in press.

Bradley Efron. Bootstrap methods: another look at the jackknife. *The annals of Statistics*, pages 1–26, 1979.

R.G. Ghanem and P.D. Spanos. *Stochastic finite elements: a spectral approach*. Dover Pubns, 2003.

R. Glowinski, C.H. Li, and J.L. Lions. A numerical approach to the exact boundary controllability of the wave equation (I). dirichlet controls : description of the numerical methods. *Japan J. Appl. Math.*, 7:1–76, 1990.

Roland Glowinski, Jacques-Louis Lions, and Jiwen He. *Exact and approximate controllability for distributed parameter systems*, volume 117 of *Encyclopedia of Mathematics and its Applications*. Cambridge University Press, Cambridge, 2008. ISBN 978-0-521-88572-0. A numerical approach.

M.A. Grepl and A.T. Patera. A posteriori error bounds for reduced-basis approximations of parametrized parabolic partial differential equations. *Mathematical Modelling and Numerical Analysis*, 39(1):157–181, 2005.

Martin A Grepl, Yvon Maday, Ngoc C Nguyen, and Anthony T Patera. Efficient reduced-basis treatment of nonaffine and nonlinear partial differential equations. *ESAIM: Mathematical Modelling and Numerical Analysis*, 41(03):575–605, 2007.

B. Haasdonk and M. Ohlberger. Reduced basis method for finite volume approximations of parametrized linear evolution equations. *ESAIM: Mathematical Modelling and Numerical Analysis*, 42(2):277–302, 2008. ISSN 0764-583X.

J. Hoke and R. A. Anthes. The initialization of numerical models by a dynamic initialization technique. *Month. Weather Rev.*, 104:1551–1556, 1976.

E. Hopf. The partial differential equation $u_t + uu_x = \mu_{xx}$. *Communications on Pure and Applied Mathematics*, 3(3):201–230, 1950.

D.B.P. Huynh, G. Rozza, S. Sen, and A.T. Patera. A successive constraint linear optimization method for lower bounds of parametric coercivity and inf-sup stability constants. *Comptes Rendus Mathematique*, 345(8):473–478, 2007a.

D.B.P. Huynh, G. Rozza, S. Sen, and A.T. Patera. A successive constraint linear optimization method for lower bounds of parametric coercivity and inf-sup stability constants. *Comptes Rendus Mathematique*, 345(8):473–478, 2007b.

T. Ishigami and T. Homma. An importance quantification technique in uncertainty analysis for computer models. In *First International Symposium on Uncertainty Modeling and Analysis Proceedings, 1990.*, pages 398–403. IEEE, 1990.

Alexandre Janon. *Analyse de sensibilité et réduction de dimension. Application à l'océanographie.* PhD thesis, Université de Grenoble, 2012.

D.J. Knezevic, N.C. Nguyen, and A.T. Patera. Reduced basis approximation and a posteriori error estimation for the parametrized unsteady boussinesq equations. *Mathematical Models and Methods in Applied Sciences*, 2010.

G. Lebeau. Contrôle analytique I : Estimations a priori. *Duke Math. J.*, 68(1):1–30, 1992.

J.-L. Lions. *Contrôlabilité exacte, perturbations et stabilisation de systèmes distribués. Tome 2*, volume 9 of *Recherches en Mathématiques Appliquées [Research in Applied Mathematics]*. Masson, Paris, 1988. ISBN 2-225-81474-0.

A. Marrel, B. Iooss, B. Laurent, and O. Roustant. Calculations of sobol indices for the gaussian process metamodel. *Reliability Engineering & System Safety*, 94(3):742–751, 2009.

N.C. Nguyen, K. Veroy, and A.T. Patera. Certified real-time solution of parametrized partial differential equations. *Handbook of Materials Modeling*, pages 1523–1558, 2005.

N.C. Nguyen, G. Rozza, and A.T. Patera. Reduced basis approximation and a posteriori error estimation for the time-dependent viscous Burgers equation. *Calcolo*, 46(3):157–185, 2009.

C Prud'homme and Anthony T Patera. Reduced-basis output bounds for approximately parametrized elliptic coercive partial differential equations. *Computing and Visualization in Science*, 6(2-3):147–162, 2004.

Christophe Prud'homme, Dimitrios V Rovas, Karen Veroy, and Anthony T Patera. A Mathematical and Computational Framework for Reliable Real-Time Solution of Parametrized Partial Differential Equations. *ESAIM: Mathematical Modelling and Numerical Analysis*, 36(05):747–771, October 2002.

G. Rozza and Patera A.T. Venturi: Potential flow. *http://augustine.mit.edu/workedproblems/rbMIT/venturi/*, 2008.

I. M. Sobol. Sensitivity estimates for nonlinear mathematical models. *Math. Modeling Comput. Experiment*, 1(4):407–414 (1995), 1993. ISSN 1061-7590.

I.M. Sobol. Global sensitivity indices for nonlinear mathematical models and their Monte Carlo estimates. *Mathematics and Computers in Simulation*, 55(1-3):271–280, 2001.

C.B. Storlie, L.P. Swiler, J.C. Helton, and C.J. Sallaberry. Implementation and evaluation of nonparametric regression procedures for sensitivity analysis of computationally demanding models. *Reliability Engineering & System Safety*, 94(11):1735–1763, 2009.

J.Y. Tissot. *Sur la décomposition ANOVA et l'estimation des indices de Sobol'. Application à un modèle d'écosystème marin.* PhD thesis, Université de Grenoble, 2012.

K. Urban and A.T. Patera. A new error bound for reduced basis approximation of parabolic partial differential equations. *Comptes Rendus Mathematique*, 2012.

A. W. van der Vaart. *Asymptotic statistics*, volume 3 of *Cambridge Series in Statistical and Probabilistic Mathematics*. Cambridge University Press, Cambridge, 1998. ISBN 0-521-49603-9; 0-521-78450-6.

K. Veroy and A.T. Patera. Certified real-time solution of the parametrized steady incompressible Navier-Stokes equations: Rigorous reduced-basis a posteriori error bounds. *International Journal for Numerical Methods in Fluids*, 47(8-9):773–788, 2005.

Karen Veroy, Christophe Prud'homme, D V Rovas, and Anthony T Patera. A posteriori error bounds for reduced-basis approximation of parametrized noncoercive and nonlinear elliptic partial differential equations. In *Proceedings of the 16th AIAA computational fluid dynamics conference*, 2003.

J. Verron and W. R. Holland. Impacts de données d'altimétrie satellitaire sur les simulations numériques des circulations générales océanique aux latitudes moyennes. *Annales Geophysicae*, 7(1):31–46, 1989.

E. Zuazua. Controllability of partial differential equations and its semi-discrete approximations. *Discrete and Continuous Dynamical Systems*, 8(2):469–513, 2002.

E. Zuazua. Propagation, observation, and control of waves approximated by finite difference methods. *SIAM Rev*, 47(2):197–243, 2005.

Future directions

Short-term directions

Each of my current research directions offers naturally short-term future questions, consisting in pursuing, deepening or improving current work. I list them quickly below:

- Small scale glaciology (Elmer/Ice):
  - improve the approximate gradient,
  - improve the algorithms,
  - include bedrock topography control,
  - implement the BFN.
- Large scale glaciology (Winnie, GRISLI):
  - add more physics in Winnie for both Kalman and 4D-Var,
  - get the full adjoint,
  - move to GRISLI,
  - implement the BFN.
- Lagrangian data: propose an applicatio to real data (e.g., Black Sea).
- Image sequences: carry on the study of observation error covariance matrices.
- Sensitivity analysis and model reduction: study a more realistic geophysical problem, e.g. Shallow-Water equations.
- BFN:
  - algorithm improvements,
  - implementation in glaciology.
- HUM: application to a real problem of non destructive control or medical imaging (defect or source localisation).

Mid-term directions

Regarding middle-term future work, a few directions seem particularly interesting to me.

Image sequences assimilation. First about image assimilation, we would like to study another type of distance to measure the observation-model misfit, more adapted to structure tracking. In particular the optimal transportation theory seems promising. The Wasserstein distance between two images measures the transportation cost from one image to the other. This notion was introduced by G. Monge, who had to optimise displacements between excavated materials and backfill zones, ie find the optimal way minimising transportation cost. The cost thus depends on the mass to be moved and the distance to cover. The Wasserstein distance between two images ρ_0 and ρ_1 (seen as densities) is given by:

$$W_2^2(\rho_0, \rho_1) = \inf_{M \text{ satisfies } (E)} \int |M(x) - x|^2 \rho_0(x)\, dx$$

where (E) is the following non linear constraint

$$(E): \quad \det(\nabla M(x)) \rho_1(M(x)) = \rho_0(x)$$

This distance notion seems more appropriate for image data assimilation. Indeed, contrary to the L^2 distance, where images are compared pixel by pixel, this distance takes into account the distance between structures supports. As it does not derive from a scalar product, the classical optimal control theory cannot apply. However, we still would like to do data assimilation, by computing the derivative of the distance with respect to the images, in order to implement a gradient descent method. This work, both theoretical and numerical, will be the subject of a PhD starting in November.

Glaciology. Second, in glaciology it is well known that (at least in some cases) the joint assimilation of bedrock and basal friction is imossible. Indeed, in an idealised configuration, a deep bedrock with few sliding leads to the same surface velocities as a higher bedrock with more sliding. In this framework, the problem is not controlable. I would like to study this problem in the general case, at least numerically if theory is too complex.

Then we would like to try and overcome this non-controlability issue. A way to do so would be to add a coupling with bedrock temperature and geothermal flux. This would give a temperature information at the base, which should help discriminating sliding/grounded zones.

Another solution, more complex theoretically, would be to study the full thermomechanically coupled model, in which the temperature field into the ice is coupled to the dynamics. Similarly, this would lead to additional information regarding the nature of the basal conditions, maybe leading to the loss of non-controlability.

Applications to biology and ecology

Finally, I am also interested in other environmental topics, in particular related to biology and ecology.

Fluid-biology coupling. On this subject A. Rousseau (MOISE) and I started to study a lake depolluting problem. The problem states as follows: water is taken out of the lake to a bioreactor, where bacteria eat the polluting material. They are then decanted, and "clean" water is taken back to the lake, according to the following scheme[1]:

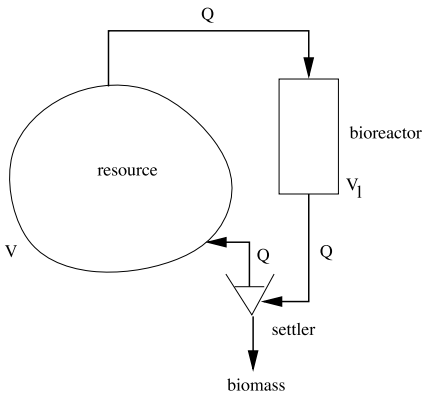

Fig. 1. Interconnection of the bioreactor with the resource.

The question is then to identify the optimal pump flow taking water from the lake. This problem has been studied before[1] in a somewhat simplified framework where the transport of the pollutant in the lake is assumed to follow an ordinary differential equation. With A. Rousseau we would like to study the problem in a more realistic framework, where fluid flow is taken into account with Navier-Stokes PDE. The model we consider represents the coupling between:

- fluid flow in the lake (with pump input/output flow),
- diffusion-transport of the pollutant by the fluid in the lake,
- pollutant consumption by bacteria in the bioreactor,
- bacteria population evolution in the bioreactor.

In this model we have one unknown parameter: the pump flow between the lake and the bioreactor. We would like to study and implement a variational assimilation method to identify the optimal value, maximising the depollution at final time.

We could also apply A. Janon thesis results to study a littoral ocean - marine biology coupled problem. Such models have many unknowns and could benefit from recent calibration tools. Sensitivity analysis could help to identify the most sensitive parameters, before calibration thanks to data assimilation could be implemented.

[1] P. Gajardo, J. Harmand, H. Ramírez C., A. Rapaport, *Minimal time bioremediation of natural water resources*, Automatica, 2011

Ecology. I am also interested in other subjects, in particular related to ecological agriculture:

- agroecology: soil microbiology modelling, in relation to hydrologie and plants;
- agroforestry: coupling between trees–agriculture–hydrology–soil

in order to better protect crops, to improve pest control, better understand interactions between various components (plants, minerals, soil biomass, hydrology, and so on). In these domains we can find modelling questions, as well as model calibration and optimisation / data assimilation, and I will soon develop collaborations on some of these subjects.